Cortical Tension of Cells:

From Apical Membrane Patches to Patterned Cells

Dissertation

for the award of the degree
"Doctor rerum naturalium" (Ph.D.)
Division of Mathematics and Natural Sciences
of the Georg-August-Universität Göttingen

submitted by

Stefan Nehls

from Göttingen

Göttingen 2017

Thesis Committee

Prof. Dr. Andreas Janshoff
Institute of Physical Chemistry
Georg-August-University Göttingen

Prof. Dr. Michael Meinecke
Department of Cellular Biochemistry
University Medical Center Göttingen

Prof. Dr. Stefan Jakobs
Department of NanoBiophotonics
Max Planck Institute for Biophysical Chemistry

Members of the Examination Board

1st Referee: Prof. Dr. Andreas Janshoff
Institute of Physical Chemistry
Georg-August-University Göttingen

2nd Referee: Prof. Dr. Michael Meinecke
Department of Cellular Biochemistry
University Medical Center Göttingen

Further Members of the Examination Board

Prof. Dr. Stefan Jakobs
Department of NanoBiophotonics
Max Planck Institute for Biophysical Chemistry

Prof. Dr. Silvio Rizzoli
Department of Neuro- and Sensory Physiology
University Medical Center Göttingen

Prof. Dr. Sarah Köster
Institute for X-Ray Physics
Georg-August-University Göttingen

Dr. Florian Rehfeldt
3rd Institute of Physics
Georg-August-University Göttingen

Date of the oral examination: 13.02.2018

I, Stefan Nehls, hereby certify that my doctoral thesis entitled “Impacts of the connection between cytoskeleton and plasma membrane on the mechanics of adherent cells” has been written independently and with no other sources and aids than quoted.

"To err is human, but to really foul things up you need a computer."

Paul R. Ehrlich

Abstract

During their lifetime, cells and tissues have to deal with a variety of mechanical challenges. Shear forces exist inside of vessels, bones have to carry the weight of organisms and connective tissues are generally deformed on a regular basis. The elasticity moduli of human tissues differ by orders of magnitude depending on the tissue type, and the successful homeostasis of elasticity is required for proper function. Cellular mechanics can be described in different ways. Here, indentation studies on apical membranes on living MDCK II cells as well as on isolated apical membrane sheets, originating also from Madin-Darbey Canine Kidney (MDCK II) cells, are presented. Preparation of apical cortices is performed using porous substrates with holes of 1.2 µm diameter that are open on both sides. These studies will provide evidence that an intact mechanical cortex can be obtained and behave mechanically similar to living cells, as addition of crosslinking agents like glutaraldehyde will stiffen the patches while treatment with Pronase E will soften them. These results suggest that only a thin layer of cells determines their mechanical response to indentation. Further indentation experiments on an epithelial cell layers show a Correlations of surface mechanical properties of cells with their projected area. To investigate this correlation, micropatterned substrates were created, providing small but precisely shaped islands of extracellular matrix proteins with a non-adhesive surrounding on standard culture dishes' glass surfaces. Cells in different shapes and areas are used in nanoindentation experiments, creating reliable maps of surface mechanical parameters. The indentation data was analysed by both, a continuum model resulting in Young's moduli and a tension model yielding a prestress and a compressibility modulus. Characteristic differences were found depending on the geometrical condition of the cells and are discussed here, resembling a possible mechanism for cells to recognize their shape.

Table of Contents

1 Introduction

After the discovery of deoxyribonucleic acid (DNA) in 1953[1], scientists believed that the DNA comprises all the basic information that pose the foundation of living systems. The sequence of the human DNA moved into the research focus and lead to the human genome project, a multinational project shared among 20 working groups. When finishing in 2000, the project had about 94% of the human basepairs recognized.[2] Besides the actual data, the project lead to the development of high throughput gene sequencing applications and essentially lead to a large toolbox of genetic experiments to expand our knowledge of how cellular life actually works. However, although our understanding of the origin and principles of life has increased dramatically ever since, there are new questions rising just as rapidly and we are still far off of a complete understanding of life or the creation of life from scratch.
Besides the vast complexity of biochemical interactions orchestrating cellular processes, cellular mechanics and mechanotransduction have gained increasing attention during the past years. Propagation of compressive mechanical waves poses a very rapid way of signaling compared to diffusion-driven chemical signals.[3] Furthermore, biophysics are assumes to be important in almost all aspects of cellular life, including function, reproduction, survivability, interaction, communication and memory. Examples for these are, among others, muscle contraction, cytokinesis, osmotic swelling, matrix stiffness and mechanotransduction. Mechanical sensing of cells is supposed to be important for correct development of tissues as, for example, shear forces are important for vessel development.[4, 5]. Abnormal behavior of the mechanical machinery of cells is probably connected to diseases like scleroderma[6], and mechanical properties can be handed down to future generations of cells as the cytoskeleton is split between daughter cells.[7]
Nowadays there exists a variety of different experimental approaches to determine mechanical behavior of cells, ranging from high troughput methods like geometrical analysis of layer images[8] or deformation based analysis of suspended cells similar to fluorescence activated cell sorting[9, 10] to subcellular resolved determination via ob-

servation of traction force microscopy (TFM)[11, 12] or response to nanoindentation. In this thesis atomic force microscopy (AFM) is used to record the repulsive force exerted by cells upon deformation due to indentation. The use of small tips on cantilevers results in small deformation and allows the recording of local indentation in well resolved grids, creating a map of mechanical properties. This approach naturally is limited to the apical side of cells and requires adherent cells, therefore MDCK II were used which are already established as a representative model for epithelial cells.

As cells are highly anisotropic materials and heterogenous in nature, they are commonly approximated to different degrees for the analysis of force-distance data. Here, a tension-based model is used that treats cells similar to liquid droplets, where deformation is countered by the energy loss due to surface area expansion and minimal contributions originate from compression of the interior. In terms of cell biology, the expanding surface is characterized by the plasma membrane and the underlying actomyosin cortex while the cytoplasm is not considered to significantly contribute to the stiffness.[13] This treatment is very different from continuum mechanics that are commonly applied in similar studies, where indentation is usually evaluated as the deformation of an isotropic semi-infinite body.[14, 15] While this is well fit for small deformations of large polymer bodies, there is a high degree of organization within cells that probably carries more information than just a bulk parameter.

MDCK II cells are an established cell line that has been applied in a number of studies as a representation of epithelial cell characteristics. It is very well suited for biomechnical investigation since the strong adhesion to substrates and the formation of a monolayer grants good access to the apical cellular cortex for a mechanical probe of choice. The strong adhesion is useful for TFM, while strong cell cell contacts and formation of intercellular junctions allow the investigation of effects due to junctional changes on mechanics. The strong adhesion also enables the isolation of native apical membrane sheets from these cells in a process called sandwich cleavage, where a second substrate is coated with a positively charged polymer, placed on top of a cell monolayer, incubated shortly to facilitate electrostatic adhesion and then ripped off.[16, 17] After this process, the strong adherent basal parts of the cells are still stuck on the culture dish while the native apical parts are transferred to the upper substrate.[18, 19] Using a porous silica substrate with pore diameters well below the size of the cells, nanoindentation into these pores were performed to observe the repulsive force occurring without any influence or organelles, cytoplasm, nuclei or other central or bottom cellular parts.

Layer analysis of the MDCK II cells have shown that the geometrical variety within a monlayers of cells is fairly pronounced, and larger scale AFM studies, as shown here, revealed a correlation between cellular size and Young's modulus. Besides cellular size it seemed reasonable that a correlation between shape and mechanics does exist as well. However, finding cells of desired shape and size in a wild growing monolayer is extremely demanding given the broad diversity of shapes. Instead, micropatterned culture surfaces were used where cells adhere on precisely controlled adhesive islands coated with extracellular matrix protein, while the majority of the surface is coated with a non-adhesive polymer. While cells on such surfaces will voluntarily adapt the

pattern geometry, this technique does however require to work with single spread cells. The matrix patterning has however already been successfully applied in studies about proliferation and epithelial-mesenchymal transition.[20, 21] Given full control over cell shape, indentation experiments were performed on these patterned cells and analyzed according to tension-based and continuum mechanics. The results were averaged using multiple datasets and pattern symmetry to obtain reliable parameter maps representing the mechanical surface properties of cells in a variety of shapes and sizes. Until now, there are only few systematic studies of the influence of cell geometry onto their mechanical properties[22], so this correlation will be specifically addressed herein.

2 Principles

2.1 Epithelial Cells

The Epithelium is one of the types of tissue that form higher organisms. In particular, epithelial cells like MDCK (Madin-Darbey Canine Kidney[23]) cells usually form a two-dimensional layer to separate different spaces from one another. In the case of kidney cells, the epithelium acts as a barrier to limit trafficking of molecules between lumen and tissue. This process includes the formation of a polarity, where the area

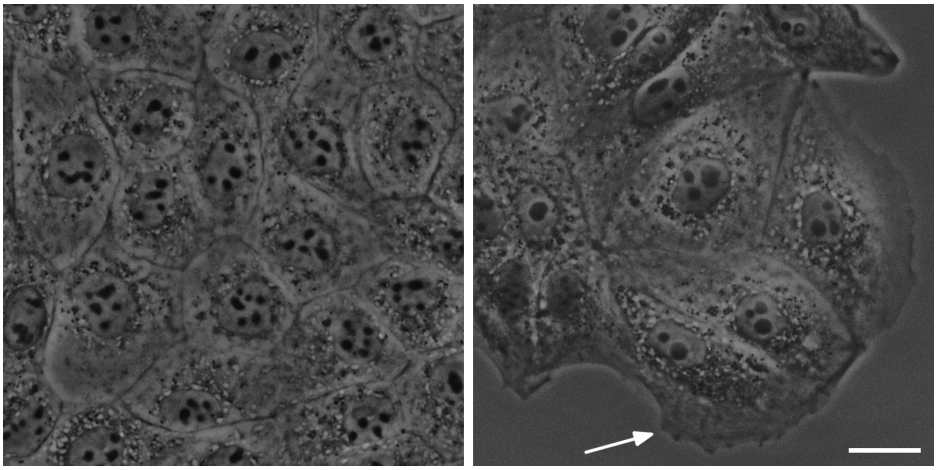

Figure 2.1 – Confluent and subconfluent cells in phase contrast images. With enough time to grow, cells form a dense two dimensional layer (left) with tightly packed cells. Earlier during development, subconfluent cells (right) tend to form clusters and show migrating ends on individual cells (arrow) that are used during proliferation to sense further suitable areas to cover. The projected cell area of spreading cells, as seen in the images, is larger than that of confluent cells. Scalebar: 20µm.

of cell-cell-contacts is called the lateral membrane, while apical membranes are facing inside a lumen and basal membranes face away from the lumen, which in the case of cultured cells refers to the culture dish surface.
In order to have control over the nutrient flow across the cell layer, the transepithelial diffusion in-between cells has to be shut down. Therefore, cells grow and cover a given surface until a confluent state is reached, at which gaps between cells are closed by tight junctions (see figure 2.1). Tight junctions are one class of cell-cell junction complexes that form belt-like structures along the lateral membrane between adjacent cells.[24] The interaction is mediated by binding of claudins of each cell to one another and is calcium dependent, while proteins including ZO-1, ZO-2 and others connect the junctions to the actin cytoskeleton.[25, 26] Depletion of calcium leads to break down of tight junctions and increases transepithelial permeability, as has been shown for example in experiments investigating the transepithelial resistance (TER).[27, 28] The very close cell membranes in the area of tight junctions is also supposed to act as a fence for large integral proteins that are unable to cross from the apical to the basolateral membrane and vice versa.[29] Notably, lipid compositions of apical and basal membranes are different from each other as well, as has been shown for phosphatidylinositol 4,5-bisphosphate (PIP_2)[30, 31] and phosphatidylinositol 3,4,5-triphosphate (PIP_3).[32] While this fence mechanism supports the maintenance of polarity in epithelial cells, it is not a necessity to form polarity in the first place. Formation of epithelial polarity has even been shown for single adherent cells ([33, 34]). Protein and lipid sorting between apical and basal membranes is also supported by directed integration from the golgi apparatus and due to attachement to actin-cortex specific proteins.[35, 36, 37]
Besides the tight junction complexes, other classes of junctions include adherence junctions and demosomes. These are usually present at the cell-cell interfaces of epithelial layers and for most cell types located closer to the basal membrane, while tight junctions are usually located towards the apical membrane. Adherence junctions are mediated by E-cadherin interaction and connected to the actin cytoskeleton[38, 39, 40], while desmosomes connect intermediate filaments of adjacent cells via desmoplakins.[41, 42, 43] Both these junctional complexes are supposed to bear cell-cell adhesion forces. Another class of cell-cell junctions are gap junctions, based on connexin interactions. These connexins typically form channels to control cell-cell trafficking of small molecules like nutrients or messenger molecules.[44]
To facilitate the transportation function epithelial cells often have an increased surface area to provide a higher number of channel protein assembles, giving a bigger microscopic surface while keeping the macroscopic surface low. Upon reaching confluency, further proliferation is downregulated by contact inhibition.[45, 46]

2.2 Cellular Adhesion

The adhesion of epithelial cells is a complex process. Since epithelial cells are meant to form a monolayer, the correct identification of suitable substrates is important to form an axial polarization and successful subsequent 2D culture.[47, 48] Adhesion is executed by the formation of focal adhesion clusters which include a number of different proteins, and enable cells to recognize the chemical composition of underlying matrices, exert forces on those matrices and thereby to probe the mechanical stiffness of the matrix.[49] All these processes are important, and it has been shown that proliferation on extra cellular matrix proteins like Collagen I and Fibronectin is enhanced compared to untreated glass surfaces in cell culture.[50, 51] Substrate stiffness is also important since cell behavior can change dramatically, as stemcells on hard substrates tend to differentiate into bone cells and muscle or neuron cells on increasingly softer substrates.[52, 53, 54] Tuning of substrate properties even leads to the formation of beta cells from human embryonic stem cells that react to glucose triggers by secretion of insulin.[55] In a different study adipose-derived stromal cells were triggered to undergo chondrogenesis depending on matrix composition and stiffness in 3D culture.[56, 57] Force exertion of cells onto substrates has been extensively studied by traction force microscopy and resulted in a deeper understanding of cell migration.[58]
In figure 2.2 the protein composition of focal adhesion clusters is illustrated. It is widely accepted that one of the main structures responsible for recognition of extracellular matrix proteins and mechanotransduction is the transmembrane integrin complex.[60, 61, 62] While the actin cytoskeleton has no direct connection to the integrin complexes, a series of different proteins serve as a joint by the formation of

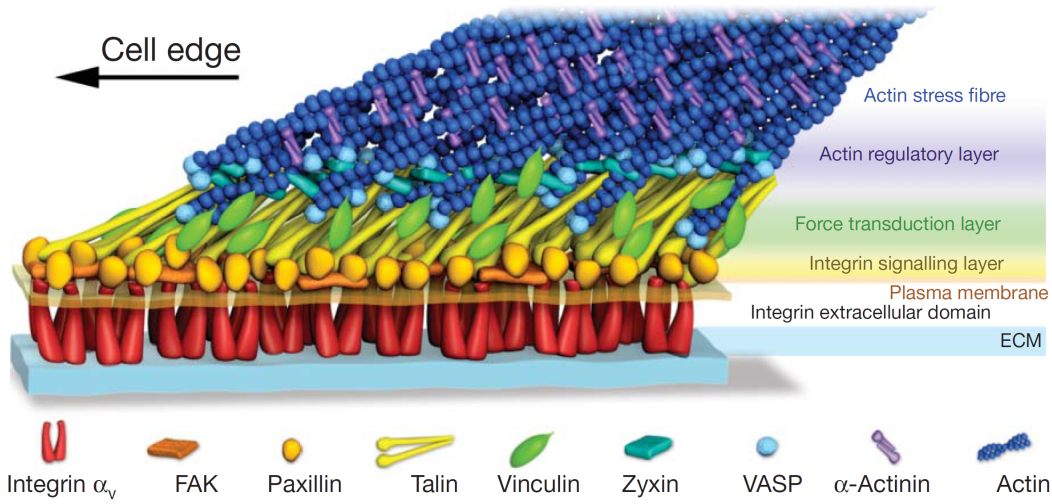

Figure 2.2 – Schematic representation of focal adhesions. Integrins bind to extra cellular matrix. Pixilin and focal adhesion kinase are located very close to the intracellular integrin domains. Talin connects integrin and actin. Adapted by permission from Macmillan Publishers Ltd: Nature [59], copyright 2010.

a matured focal adhesion complex. Talin is one of the these proteins with binding domains for both actin and integrin and is therefore able to connect both with each other.[63, 64] Paxillin is another example for a protein located in the focal adhesions by binding to the β-subunit of integrin.[65] Paxillin is involved in the dynamic regulation of focal adhesion assembly and maturation, working in conjunction with the focal adhesion kinase[66, 67] and many others.[68] Paxillin is one of the most used staining targets for focal adhesion localization in fluorescence microscopy besides the actual integrin.[69, 70] Dynamic regulation of these focal adhesion complexes does not only include the complex composition itself, the machinery also leads to increased actin polymerisation close to the site, leading to strong actin bundles that are used to exert force onto the substrate that the cells adhere on. Maturation of focal complexes is strongly promoted by tension on the stress fibers, underlining the role of the focal adhesions in mechanotransduction.[71, 72]
This formation of anchoring points is not just the basis for cell spreading and migration[73] but also has been in the focus of mechanotransduction studies, revealing that the translation from mechanical to chemical signals is not limited to mechanosensitive channel proteins but also pathways are being discovered that directly link mechanical stress to changes in nuclear structures and rapid changes of gene expression.[3] The advantage of mechanical signals is that stress waves propagate at much higher velocity compared to chemical diffusion.[74]
Focal adhesions are not only important for correct cell spreading and proliferation but also during migration. The process of cell relocation involves the formation of lamellipodia that consist of highly branched actin filaments that support a flat ($<$300 nm) but broad membrane protrusion.[75, 76, 77] Filopodia on the other hand are finger-like membrane protrusions containing mostly parallel bundles of actin filaments. The membrane of these filopodia usually contains integrins and due to the constant movements of the contractile actin network constantly probe the cells' surrounding.[78, 79] Upon binding to a suitable ligand, focal adhesion complex maturation is started and expansion of the lamellipodium occurs, expanding the cell towards the direction of the suitable surfaces. Contraction of the cells' rear will finish this directed motion.

2.3 Apical Membrane Organization

While adhesion takes place at the basal membrane of polarized epithelial layers, the apical side of cells is facing into a lumen. The tight barrier of transporting epithelia, as described in section 2.1, makes the cell layer a strong barrier to prevent any substances from crossing between apical and basal side in an uncontrolled manner. The active transport of molecules however needs special channel proteins that are able to actively work against an unfavorable concentration gradient. Epithelial cells have a heavily ruffled surface with a large number of protrusions. One advantage of this is that every cell can integrate a large number of transport proteins into their membrane and therefore increase the performance in their transport capabilities.
Another advantage of a ruffled surface is that when cells are in need of extra membrane area, these ruffles can be flattened to provide additional area. Processes that involve the need of such excess area are deformations or a net increase of volume. In hypoosmotic conditions for examples cells will accumulate addition water, thereby increase their volume and consequently their circumference. Addition of hypoosmotic solutions on top of confluent epithelial cell layers has indeed shown to flatten the apical surface.[80, 81, 82] Another impressive example is the phagocytosis of particles by macrophages, who can drastically increase their surface area and can cover large objects by sacrificing small microstructures on their surface.[83]
One of the best known microstructures on cellular surfaces are microvilli.[84] They form turbular protrusions with a small diameter of about 50 nm and can grow to lengths in the range of 1-2 µm[85, 86]. To grant these tall structures stability, actin filaments are present within the microvillus (see figure 2.3). The outer plasma membrane is connected to the filaments by protein like ezrin, radixin and moesin. The tight connection can withstand the osmotic pressure from inside of the cell and thereby allows the formation of structures that increase the surface area.
While the microvilli are stabilized and tightly bound, they are also very dynamic.[87] This might seem like a contradiction on the first view, but active processes are performed all the time by remodeling of the cytoskeleton and actively phosphocycling ezrin. Phosphocycling refers to a process of constant phosphorylation and dephosphorylation mediated by both kinases and phosphatases, essentially enhancing the turnover of phosphate residues on proteins under consumption of adenosine triphosphate (ATP).[88] While the enzymes, that are responsible for phosphocycling, are still under debate and probably depend strongly on the cell type, lifetimes of active ezrin is similar to that of microvilli.[89] The length and position of actin filaments is also in an actively accelerated balance.[90, 91] PIP_2 levels, for example, influence the amount of bound ezrin and the amount of f-actin by regulation of relevant polymerization proteins and therefore universally influence this dynamic equilibrium.[92, 93] The maintenance cost for these acceleration are high, and implies that microvilli serve more purposes than just static surface increase. One of the proposed uses is the compensation of area expansion during mechanical challenging processes like osmotic cell swelling. In these cases, a rapid regulation of microvilli appearance is of major importance to feed their surface area into the area dilation process but also to recover microvilli as fast as possibile to reestablish membrane

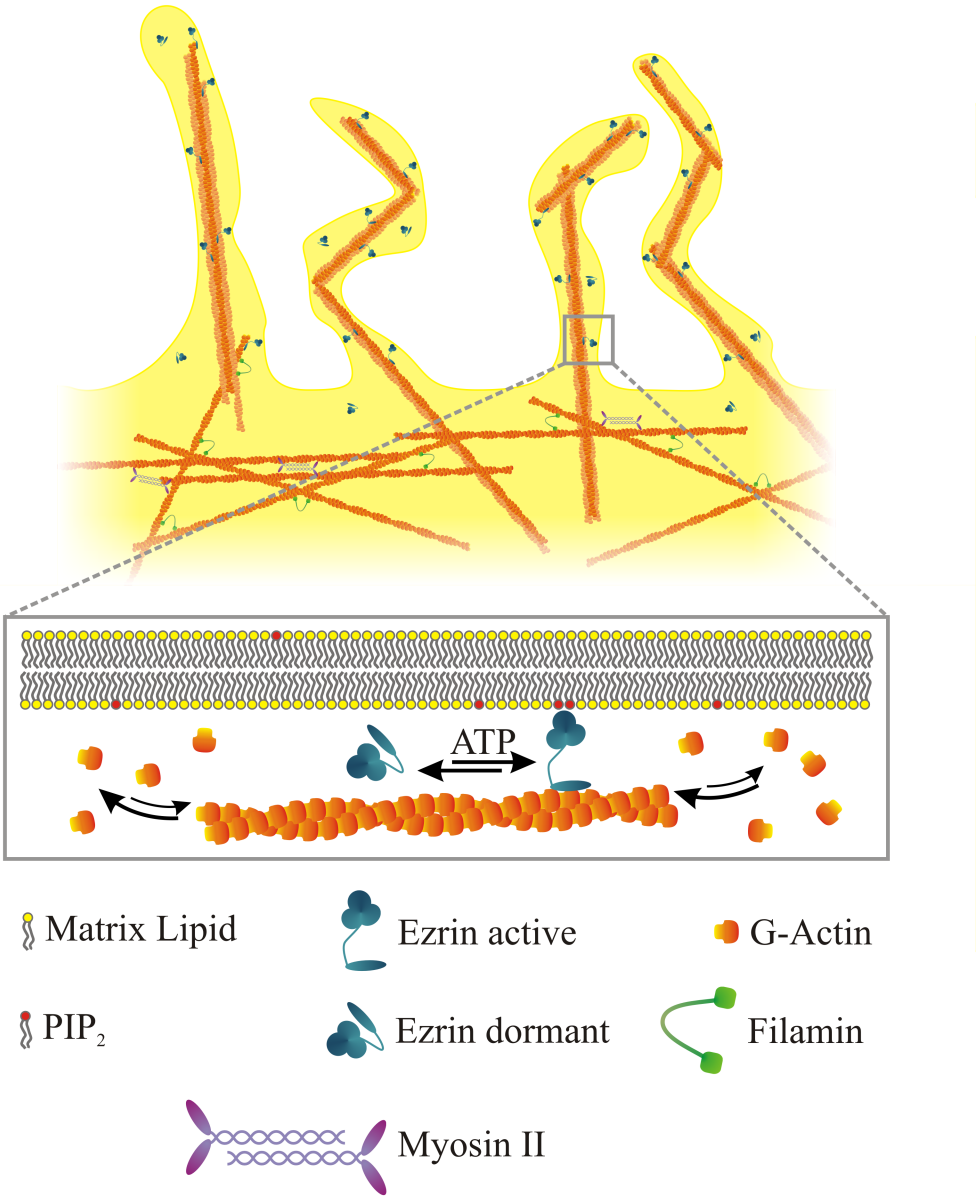

Figure 2.3 – Schematic drawing of the organization of the apical cell cortex. Finger-like protrusions called microvilli (4 instances shown here) are located on the apical surface of epithelial cells facing towards a lumen. They are stabilized by actin filaments that are located within the microvilli and linked to the membrane via ezrin, which binds to f-actin and PIP_2. This system is in a dynamic balance where ezrin is rapidly actived and inactivated by phosphocycling and actin fibers are treadmilling by polymerization and depolimerization at both ends simultaneously but with different rates. The cortex underneath the zone of microvilli is further supported by f-actin, which forms a dense network including crosslinkers like filamin and active motors like myosin II.

homestasis and functionality.

2.4 Cell Mechanics

Biophysics have raised increasing attention in recent years, where the influence of mechanical properties on molecular, cellular and tissue level upon the healthy development and operation of organisms as well as disease mechanisms has been widely accepted.
The atomic force microscopy in particular was applied since the 1990s to receive highly resolved images and also probe the mechanical response of living cell samples.[94, 95, 96, 97] Constant technological advances have helped the AFM to become a versatile tool in biophysical chemistry and allow rapid high quality spatio-temporal determination of cell mechanics. In the course of such investigation a small probe usually of the shape of a cone or sphere is pushed on or into a cell's surface with a contact area ranging from nm^2 to μm^2. During such an indentation the repulsive force acting on the probe is recorded depending on the probe movement, yielding a force distance curve (FDC).
The most applied model to evaluate such FDCs is the so called Hertzian model in the case of spherical indenter or Sneddon model for conical indenters respectively.[14, 15] Both these models treat a sample as an infinite semi space of an elastic polymer without consideration of adhesion and friction. Adhesion is included in the Johnson-Kendall-Roberts model[98], but since uncoated probes show weak adhesion forces compared to the compressive forces, Hertz and Sneddon are sufficient to describe the data. According to Sneddon and coworkers the force(f)-distance(δ) relation in the case of conical indenters with half-opening angle θ indenting a sample of Young's modulus E and Poisson's ratio ν is

$$f = \frac{2E\,\tan(\theta)}{\pi(1-\nu^2)}\delta^2. \tag{2.1}$$

Since this approach includes the approximation of an infinitely thick sample, the quality of the received moduli is getting worse as the relative indentation depth increases. For large indentations of thin samples with height h the mechanics of the underlying substrate starts to influence the force response. To include this substrate effect Gavara and Chadwick[99] corrected the equation based on the solution for the Green's function in case of $\delta/h < 1$ by Dimitriadis *et al.*[100] assuming $\nu = 0.5$ to

$$f = \frac{8E\,\tan(\theta)\delta^2}{3\pi}\left[1 + 1.7795\frac{2\tan(\theta)}{\pi^2}\frac{\delta}{h} + 16\tan(\theta)^2 1.7795^2\frac{\delta^2}{h^2} + \mathrm{O}\left(\frac{\delta^3}{h^3}\right)\right]. \tag{2.2}$$

The substrate corrected equation has been applied in studies of for example actin dependency of single cell stiffness[101], the characterization of melanoma cells via elasticity[102] or the drug-dependent mechanical changes in fibroblasts on matrix patterns[103].
A distinct alternative approach to the continuum mechanics is a tension-based explanation of the mechanical response during the poking of cells. Instead of an elastic continuum the tension model treats cells like liquid filled droplets with an

outer shell, the plasma membrane and the cortex, that create an inward facing force due to in-plane tension that counteracts the outward facing osmotic pressure of the cytoplasm. This picture takes the inhomogenity of cells into consideration and is therefore better suited for such shell-like cell bodies with cortical thickness of $< 200\,\mathrm{nm}$ like reported for human foreskin fibroblasts[104] or HeLa cells[105].
The fundamental equation of the tension model reads

$$T = \frac{K_A}{A_{\mathrm{ex}} + A_0}\Delta A + T_0, \tag{2.3}$$

which determines the tension T as a sum of the prestress T_0 and the area dilation ΔA multiplied by the compressibility modulus K_A and divided by the sum of area before indentation A_0 and excess membrane area A_{ex}. Excess membrane area describes microscopic membrane reservoirs like microvilli and caveolae that are readily available if surface expansion required additional surface area[106, 107], since bilayers are known to rupture at dilations of 2-3%.[108] The force f is then calculated as the integral of tension along the line of the force-balance with length s_{max} in a given setup to be:

$$f = \int_0^{s_{\mathrm{max}}} T \mathrm{d}s \tag{2.4}$$

This model has been applied in previous studies[109, 13, 82, 110] and it's main challenge poses the determination of the exact place of force balance and the calculation of area dilation, both of which are usually explained in detail by geometrical treatment of each individual setup, as done very elaborately for example by Sen and Disher.[111] Note that also, depending on the study, apparent compressibility moduli are often given as $\tilde{K}_A = K_A/(A_{\mathrm{ex}} + A_0)$ or $\tilde{K}_A = (K_A\, A_0)/(A_{\mathrm{ex}} + A_0)$ in units of $\mathrm{N/m^3}$ and $\mathrm{N/m}$ respectively.
The flattening of surface membranes, as for example in fibroblasts due to the required surface expansion during spreading, has been known for a long time[112, 113] and underlines the importance of tension homeostasis in plasma membranes and respective cell cortizes. While contribution of both, elastic polymer-like cytoplasm and tension-based shells, are widely accepted the dominance of either over the other in terms of cell mechanics is still being disputed. It should be noted that the tension we refer to here is different from the membrane tension that is received by tether experiments which only composes of pure membrane tension and neglects cortical tension.[114, 115] It should neither be confused with epithelial tension that refers to supra cellular tension in epithelial layers.[116]

2.5 Models for Layer Analysis

Among a number of tissue types, epithelial monolayers consist of tightly packed cells with strong cell-cell-contacts. Inside these layers a global force balance exists that originates from a number of small balances between individual cells, and the geometry of single cells is strongly influences by the forces acting on every cell's borders. Analysis of cell layers can therefore give insights about the layer's mechanical behavior. A number of different models have evolved to connect cellular behavior to mechanics on layer level, for example cells can be approximated to instances of a nematic crystal phase.[117, 118]
More detailed treatments are often based on the individual cells' borders, that are either exactly extracted from binarized image data or received via tessalation considering cell centers. Contact lines between cells usually end in three-fold vortices where two new contact lines arise. The geometry of such vortices is used in a growing number of models that conclude mechanical parameters from the pattern formation in confluent monolayers, considering the size and shape of the individual cells. While these models can be applied to optical images of cell borders and therefore give access to a large number of cells and layer wide mechanics, complementary data could be acquired in AFM based deep indentation experiments where deformations of cell layers on the upper micrometer scale could be examined while recording the force feedback.[8]
Vertex models were applied to the development of drosophila wing disc formation. These wings undergo major geometrical reorganization that are thought to occur due to mechanical changes of the individual cells. In these models, the total energy of a layer is calculated by

$$E = \sum_N \frac{K_N}{2}(A_N - A_{N,0})^2 + \sum_{i,j} \Lambda_{ij} l_{ij} + \sum_\alpha \frac{\Gamma_N}{2} L_N^2. \tag{2.5}$$

This energy including N cells describes a compression contribution of the compressibility modulus K times the area increase from the ideal projected cell area A_0 to the actual area A_N of the respective cell squared. Additional terms include the adhesion energy between two cells that is calculated for any connected pair of vortices with index i and j as the product of line tension Λ_{ij} and the length of the contact line l_{ij} as well as the contractility term Γ_N and the circumference L_N of each cell.
Considering this energy landscape and assuming that a cellular monolayer will always try to shift verteces to find at least an local minimum of the overall energy, causing a force acting on the vortex in the direction of the minumum of $F_i = -\partial E/\partial R_i$, where i is the index of the given vortex and R describes it's position. Running a simulation that induces cell division (by choosing a ramdom cell and a random cell division axis), Farhadifar *et al.* showed that within a few generations a perfectly hexagonal pattern of equally sized cells will change into a diverse mixture of individual cell shapes having broad distributions of cell areas and polygon orders.[119] While the original hexagonal pattern is the global minimum of the energy function, spontaneous reorganization of the vorteces will settle in local minima where the variance of

the geometrical cell features decreases rapidly with the number of cell generations. Comparing the resulting patterns of their simulations to real data they concluded the relations of contractility, line tensions and compressibility present in drosophila wing layer formation.
It should be noted that although these models explain the formation of cellular geometries within confluent layers by the physical and mechanical properties of the cells involved, they do assume an at least mainly identical distribution of cellular properties in the cells of the confluent layer and especially within single cells of the layer. Nanoindentation experiments on the other hand are able to identify anisotropic intracellular tension.
Also while layer tension might be the main driving force of layer organization, contribution of tension along the plasma membrane has not been excluded. Although these two types of tension are based on a two dimensional picture of a cell or cell layer they do not need to be equal, as layer tension along a large number of cells can be transmitted mainly through the contractile ring and/or cytoskeletal structures deep inside of cells, while the membrane tension can be decoupled from deeper structures and only connect to a thin sheet-like cortex right underneath the membrane.

3 Materials & Methods

3.1 Cell Culture

All experiments were carried out on Madin-Darbey canine kidney cells (MDCK II, Health Protection Agency, Salisbury, United Kingdom). Cells were kept in an incubator (Heracell 150i, Thermo Fisher Scientific, Waltham, Massachusetts, USA) at 37°C under 7.5% CO_2 atmosphere in culture flasks (TPP, Trasadingen, Switzerland) under MEM (Minimal essential medium with Earl's salts, 2.2 g/L $NaHCO_3$, Biochrom, Berlin, Germany) containing 4 mM L-Glutamine (Lonza, Basel, Switzerland). Cells were subcultivated twice a week by addition of a 0.05% Trypsin and 0.02% EDTA (Biochrom, Berlin, Germany) and short incubation at 37°C under 7.5% CO_2 atmosphere. The suspension was centrifuged and the solution discarded while cells were resuspended in MEM and seeded in the mentioned culture flasks or used for further experiments.

3.2 Substrate Patterning

To create micrometer-scale patterns on culture dishes, plasma induced protein patterning was used. First patterns were drawn in AutoCAD (Autodesk, San Rafael, California, USA) and the corresponding mask was created (Compugraphics, Jena, Germany). The mask was used to create structured surfaces on silica-wafers, which were kindly prepared in part by the group of Prof. J. Rädler and in part by the coworkers of Dr. M. Tarantola.
The passivated, microstructured wafers were then used to cast polydimethylsiloxane (PDMS, SYLGARD 184, Dow Corning, Wiesbaden, Germany) molds, by mixing polymer and curing agent in a 10:1 ratio and curing it at 70°C for 4 h. The finished stamp was peeled off the wafer.

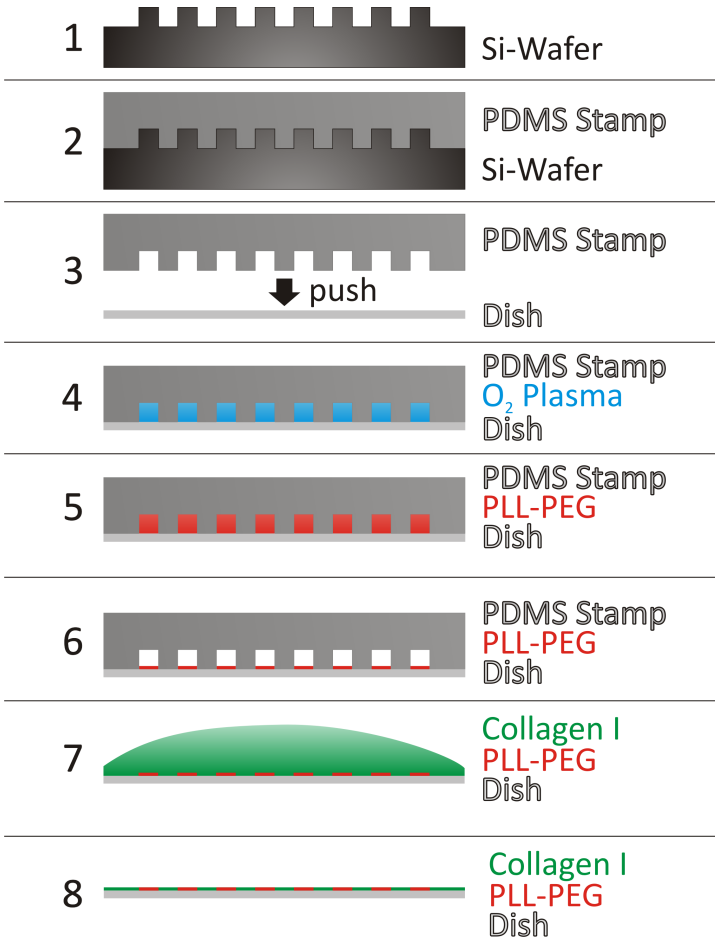

Figure 3.1 – Schematic representation of the plasma induced micropatterning technique. A small pattern in created ontop of a silicon wafer by illumination of photosensitive coating through a corresponding chromium mask (1). Addition of PDMS and curing on the silica wafer results in a stamp carrying the negative pattern (2). The PDMS stamp is placed on a culture dish (3) and exposed to oxygen plasma reaching only the cavities of the stamp (4). Addition of small volumes of polymer-containing solution fills the cavities due to capillary forces (5) and is left to dry(6). The stamp is removed liberating the parts previously covered by the stamp. Subsequent addition of Collagen I containing solution (7) will have the matrix polymer adhere to free spots on the dish resulting in the final pattern of collagen and non-adhesive polymer (8).

Glass-bottom Petri dishes (Ibidi, Martinsried, Germany) were cleaned by washing with ultrapure water and ethanol and dried in nitrogen stream. The freshly cured PDMS stamp was cut into 5 mm x 5 mm pieces and placed onto the glass surface. While in contact the dish was placed in a plasma cleaner and exposed to oxygen plasma for 90 seconds. Immediately after plasma treatment a solution of poly-L-lysine-graft-poly-ethyleneglycol (0.5 µL, PLL(20)-g[3.5]-PEG(2)/TRITC, SuSoS, Dübendorf, Switzerland) solution was added to each individual stamp, and the sample rested for 1 h at 23°C under exclusion of light. Within the given time period, the solvent evaporated. After incubation the stamps were removed and the dish was washed three times with Phosphate-buffered saline without Mg^{2+} or Ca^{2+} (PBS, Biochrom, Berlin, Germany) and a solution of bovine Collagen I (0.2 mg/mL,

Thermo Fisher Scientific, Waltham, Massachusetts, USA) in phosphate buffered saline was added and incubated for another two hours. Finally, the dish was again washed three times with PBS and twice with MEM, and 100.000 MDCK II cells suspended in 2.5 mL M10F40 (MEM containing 10% fetal calf serum (Biowest, Nuaille, France), 4 mM L-Glutamine (Lonza, Basel, Switzerland), Penicillin/Streptomycin (Konzentration), 0.25 mg/mL Amphotericin B (Biochrom, Berlin, Germany) and 40 mM 4-(2-hydroxyethyl)-1-piperazineethanesulfonic acid (HEPES, Biochrom, Berlin, Germany)) were added and incubated at 37°C. After 60 minutes the sample was rinsed with M10F40 to remove any non-adherent cells and atomic force microscopy measurements were started.

3.3 Staining Protocols

Membrane staining for live-cell imaging was prepared by rinsing a cells sample with PBS and addition of 1 mL MEM containing CellMask Orange (1:500, Thermo Fisher Scientific, Waltham, Massachusetts, USA). Samples were incubated at 37°C under exclusion of light for 10 min, rinsed three times with M10F40 and were ready for imaging.
Every other staining was preceded by fixation using 4% Paraformaldehyde (Sigma-Aldrich, Steinheim, Germany) in PBS for 20 min and blocking of unspecific binding by addition of 5% bovine serum albumin (BSA, Sigma-Aldrich, Steinheim, Germany) and 0.3% Triton-X (Sigma-Aldrich, Steinheim, Germany) and incubation for 30 min.
Staining of the nucleus involved the addition of 4',6-Diamidino-2-Phenylindole (DAPI, 50 ng/mL, Invitrogen, Life Technologies, Carlsbad, US) and incubation for 20 min.
Staining of filamenteous actin was performed by addition of AlexaFluor-488-Phalloidin (0.22 mg/mL, Thermo Fisher Scientific, Waltham, Massachusetts, USA) and incubation for 45 min.
Antibody staining required first the addition of primary antibody solution, therefore either mouse anti-Ezrin (5 µg/mL, BD Biosciences, Heidelberg, Germany), mouse anti-Podocalyxin/gp135 (3F2, 34 µg/mL, Developmental Studies Hybridoma Bank, University of Iowa, Department of Biology, Iowa, USA)[33] or mouse anti-ZO-1 **(info)** were diluted in PBS containing 1% BSA and 0.3% Triton-X and incubated for 45 min. In a second step secondary antibody solution of AlexaFluor-488 or AlexaFluor-546 goat anti-mouse (5 µg/mL, Thermo Fisher Scientific, Waltham, Massachusetts, USA) in PBS containing 1% BSA and 0.3% Triton-X was added and incubated for 60 min.
All Staining steps on fixed samples were performed under protection from light and between each staining step samples were washed three times with PBS.

3.4 Sandwich-Cleavage

Petri dishes (35 mm, TPP, Trasadingen, Switzerland) were coated with poly-D-lysine for 2 h (PDL, 50 µg/mL, mol wt. > 300,000, Sigma-Aldrich, Steinheim, Germany).

After washing with PBS three times MDCK II cells were seeded on the coated dishes and grown to confluency over the course of two days. Porous silica substrates, exhibiting pores of 1.2 µm diameter in a hexagonal pattern (FluXXion), were cleaned in argon plasma, sputtered with Chromium and coated with 20-25 nm gold in an evaporation chamber. Immediately after the metal coating process PDL the substrates were immersed into PDL-solution (0.2 mg/mL) and incubated for 2 h.
For Membrane isolation, the confluent cell culture were stained for membrane using CellMask Orange (see section section 3.3) and rinsed with ultrapure water and kept under ultrapure water for 1 min. The PDL-coated porous substrates were placed on top of the cell facing upside-down, pressed gently and incubated for 30 min. Subsequently, substrates were taken off the cells, washed with PBS twice and either kept under PBS until force measurement experiments were performed or treated further as marked in the experiments. To digest protein content on the patches Pronase E (2 mg/mL in water, Sigma Aldrich, Steinheim, Germany) was added for a period of 1 h while for crosslinking of proteins glutaraldehyde (0.5% in PBS, Sigma Aldrich, Steinheim, Germany) was added for 10 min.

3.5 Optical Microscopy

Epifluorescence images were acquired on ether an upright microscope (BX51, Olympus, Tokyo, Japan) or an inverted optical microscope (IX83, Olympus, Tokyo, Japan). Images were taken in either 10x or 40x objectives, images for cell size analysis and cell cycle determination were captured in large arrays using a motorized stage. 3D stack images were taken on a confocal microscope (LSM 710, Zeiss, Jena, Germany) using a 100x immersion objective (UPLFLN100XO2PH, NA = 1.3, Olympus, Tokyo, Japan).

3.6 Fluorescence Recovery After Photobleaching

Bleaching of samples was performed on a confocal laser scanning setup (LSM 710, Zeiss, Jena, Germany). After bleaching of the fluorophores the recovery was observed relative to a not-bleached reference sport on the same image. The cumulative intensity was obtained from integrating the pixel intensities within the defined region of interests from a time-lapse repetitive capture of the same sample. To estimate the actual diffusion coefficient, a model described by Axelrod et. al.[120] was applied.

3.7 Cell Cycle Determination

To address the question whether or not freshly seeded cells have a memory effect of their previously contact-inhibited cell-cycle, cells were either seeded and grown to confluency over the course of two days and fixed or fixed after performing experiments on patterned cells. Samples were stained for nucleus (see section section 3.3) and automated fluorescence image acquisition was performed (see section section 3.5). Single images were stitched together using a Fiji plugin[121] and nuclei were recognized using CellProfiler[33]. The Identification and integration of fluorescence intensity was done in CellProfiler, creation of histograms was done using MatLab (The MathWorks, Natick, USA).

3.8 Cell Shape Evaluation

Identification of single cell shapes was examined on confluent samples similar to those used in cell cycle determination (section section 3.7) but with staining of ZO-1 (section section 3.3). Images were taken in a raster as described in section section 3.5 and analyzed using a home-made MatLab script which will be briefly described in the following.
The process involved the recognition of cell borders by thresholding the fluorescence image of ZO-1, dilation and subsequent erosion of the binary image to close small gaps, and skeletonization of the ZO-1-containing zones. Every pixel not covered by these zones and not touching the edges of the image was identified and counted. To count the number of neighbors to each cell, cells were dilated by 1 px and the number of cells touching the original one was counted. Cell size was determined by multiplication of the number ob pixels of each individual cell with the pixelsize.
To get an idea of the shape of these cells, which in principle is likely to be unique for any given cell, the overlap with either a square, a disc, a rectangle or a hexagon of the same size was calculated. Note that the first three patterns correspond to the ones used for patterned cells in section section 3.2. To do so, cells were rotated in steps of one degree and for any rotation the maximum of the crosscorrelation to each of the four patterns was determined. The best correlation for the best rotation was used, the number of overlapping pixels was counted and divided by the area of the respective cell, resulting in values of overlap ranging from zero (no overlap at all, virtually impossible) to one (full overlap and perfect match).
To examine the size distribution of single cells, glass-bottom Petri dishes equal to the patterning protocol were cleaned in oxygen plasma and coated with Collagen I, essentially the same way as the patterned surfaces were prepared but without using a stamp or non-adhesive polymer. 10,000 cells were suspended in 2.5 mL M10F40 and seeded on those surfaces, washed after 1 h of incubation at 37°C and incubated for another hour. Due to the low cell concentration and early washing step almost only individual cells were attached onto the surface. Samples were fixed and stained for membrane and nuclei. Cell recognition was achieved by using CellProfiler with a self-written pipeline, identifying nuclei according to the staining and using the

positions of the nuclei as seeds for identification of the cell body. The threshold for body classification was set by hand for every experiment as required by the particular image quality and results were saved as outline overlays to be verified easily. All recognized cells were filtered for either multiple cells touching each other and cells touching the image frame.

3.9 Atomic Force Microscopy

Force microscopy studies on isolated membrane sheets were performed on a MFP-3D (Asylum Research, Santa Barbara, USA) with an approach speed of 5 µm/s. The force setpoint was at 0.5 nN while using a MLCT cantilever (C-lever, Bruker AFM Probes, Camarillo, USA). Measurements were performed as forcemaps using a lateral resolution of 150 nm x 150 nm.
Studies on living cells were performed on an NanoWizard IV (JPK instruments AG, Berlin, Germany) mounted on an inverted optical microscope (IX 81, Olympus, Tokyo, Japan), allowing for parallel acquisition of optical images and force data with phase-contrast or fluorescence at 10X or 40X magnification. Force Experiments were done with the softer CSG11-cantilever (NT-MDT Spectrum Instruments, Moscow, Russia) calibrated via thermal noise[122] at constant axial velocity of 5 µm/s up to a trigger force of 500 pN. Forcemaps were taken with a lateral resolution of 1.5 µm x 1.5 µm.

3.9.1 Evaluation of Membrane Patches

To determine the mechanical properties of isolated apical membrane sheets a home-written MatLab script was used. The script can load the force-distance data from the MFP-3D and plot a trigger-point height map, where the centers of pores were selected manually. The central force-distance curve (FDC) was picked together with the surrounding FDCs, giving 9 FDCs in total per pore. This was repeated for all pores and for every FDC the contact point was selected by hand and the parameters of the tension model as described in section section 4.1.2 were received by fitting the FDC to equation equation (4.10). FDCs showing either bad accordance to the fit or artifacts from the measurements (e.g. membrane rupture or distortion in the baseline) were discarded, and all accepted values of the 9 FDCs were averaged per pore.

3.9.2 Evaluation of Cellular Membranes

The determination of size dependent mechanics was performed by acquisition of force maps of a 100 µm x 100 µm with a resolution of 1 μm^2. The cell-cell-contact lines were drawn by hand according to optical images and slope maps. A self written script in MatLab was used to determine the Young's moduli. In brief the scripts accept the

cell borders, eliminate all cells touching the force map frame, indexed all full cells and attributed all FDCs to either the corresponding cell number or discarded them. The FDCs were integrated to extract the modulus as described in section 4.2.2.
In the case of patterned cells for every cell the correct pattern in the fluorescence images was checked. Force maps were taken covering the whole cells and FDCs on membranes were separated from those on pure substrate and contact points were chosen by hand. Tension parameters were gained by fitting according to the theory described in section 4.2.2. The center of cells in force maps were determined and the force maps were translated and rotate to match the best overlap with an identically sized ideal pattern. The results in a given pixel were average over all experiments for a given pattern and the symmetry of the pattern, which is 8-fold for discs and square and 2-fold for the rectangular triangle. The mean values were then used for spacially resolved analysis as well as for kernel density distributions.

4 Results and Discussion

The complex architecture of cells naturally makes them hard to describe in terms of their mechanical properties. They consist of a number of different organelles, positioned in a highly heterogenous cytoplasm. The high degree of organization regarding the distribution of proteins and lipids within these compartments additionally contributes to the complexity of this system.
Since it is almost impossible to develop a model including each and every interaction inside cells and determine their contribution to the mechanical response of cells upon deformation, currently used models have to approximate these properties to some degree. As discussed in section 2.4, the most common model is treating cells as a semi-infinite half-space and calculate Young's moduli from indentation experiments. tension-based models on the other hand assume a soft interior with a thin shell, where deformation is countered by prestress and compressibility of the shell. The goal of this thesis is to compare the two models and apply them to indentation studies performed on epithelial cells.
In the first part, it will be shown that the apical membrane and a thin layer of cortex can be transferred onto a porous silica substrate, and indentation experiments of these thin samples are compared to results from living cell studies. This basically underlines the applicability of a tension-based model to explain mechanical responses of cells due to indentation.
In the second part, studies on cells of MDCK II monolayers reveal a broad distribution of different shapes that cells adapt. Additionally it will be demonstrated that cells with larger projected area have a higher stiffness. Due to the amounts of data, analysis will be performed according to Sneddon *et al.*[15] without manual contact points.
To further investigate the correlation of shapes and sizes with cellular stiffness, studies on micropatterned substrates will be presented in the last part. By providing an exactly shaped small area of extracellular matrix, while the culture dish is mostly

coated with non-adhesive polymer, the projected area and shape of cells can be tuned as desired. These studies demonstrate that, surprisingly, tension homeostasis is very pronounced in MDCK II as compressibility and Young's modulus are only slightly altered by spreading area. The prestress on the other hand undergoes dramatic changes depending on size.
All of this underlines the complexity of cellular mechanical behavior that is depending on the cellular state and highly inhomogenous across the cell surface.

4.1 Apical Membrane Sheets

Studies performed on apical membranes are published in *Elastic Properties of Pore-Spanning Apical Cell Membranes Derived from MDCK II Cells*, Stefan Nehls, Andreas Janshoff, Biophysical Journal, Volume 113, Issue 8, pp. 1822–1830, 2017.

4.1.1 Validation of Apical Membrane Integrity

Typical results of the sandwich-cleavage method to generate apical membrane fragments were shown in figure 4.1, documenting the integrity of the membrane patches. The membrane patches were stained using CellMask Orange (red) while F-actin was visualized using phalloidin (green). The membrane staining was used in all experiments to identify the patches prior to force measurements, while F-actin staining

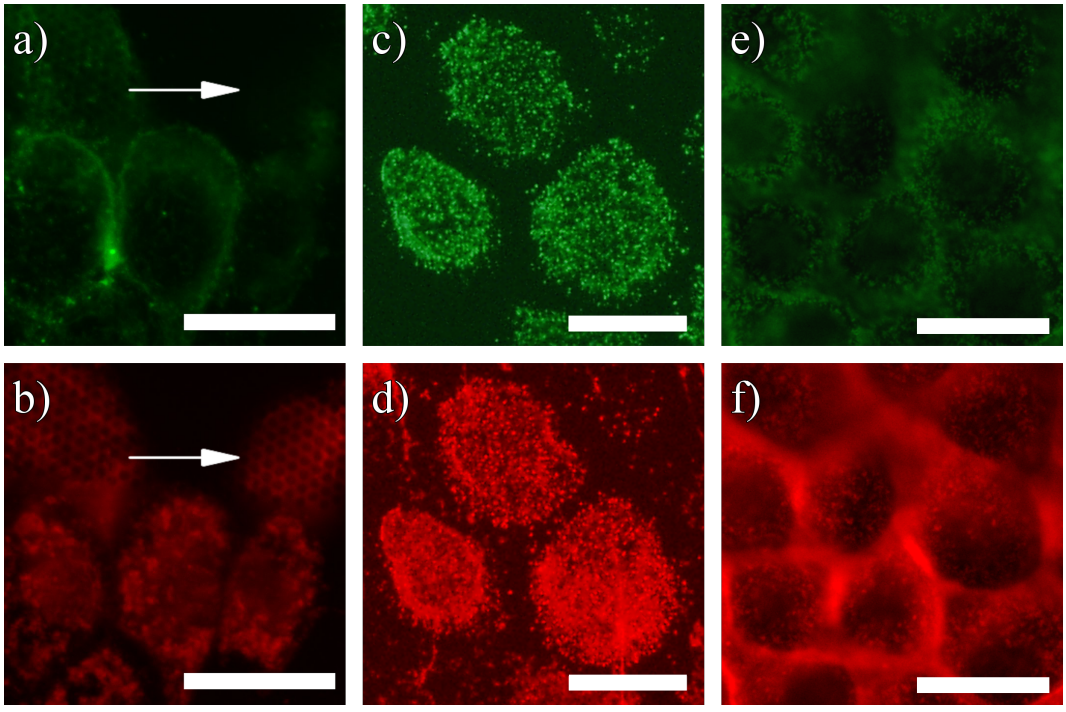

Figure 4.1 – Fluorescence images of membrane patches deposited on porous silica substrates with a pore diameter of 1.2 µm. Staining of apical membrane in red with CellMask Orange (a) and F-actin in green using phalloidin (b) shows an inhomogenous distribution of actin on top of the patches. The patch on the top right (arrow) generates almost no intensity from attached actin, while the other patches show remnants of the cortex especially associated with microvilli. Staining of F-actin (red, c) and ezrin (green, d) shows colocalization in point-like structures identified as microvilli. Similar patterns are found in cultured MDCK II cells stained for F-actin (red, e) and ezrin (green, f). Scalebar: 20 µm.

was only used occasionally after carrying out the force measurements.
The amount of F-actin inferred from the fluorescence signal on top of the patches can vary considerably (figure 4.1 a, b). Some patches show a quite dense actin network, while others display only a few filaments that are visible as point-like clusters (figure 4.1 c, d). These clusters probably originate from the microvilli that are very pronounced on the apical surface of cultured MDCK II cells (figure 4.1 e, f). Figure 4.2 shows a scanning ion conductance microscopy (SICM) image of the apical surface of MDCK II cells. SICM creates label-free non-contact topographical images of delicate surface structures attached to a soft cell[123, 124].
Microvilli are formed and supported by F-actin and linker proteins like ezrin, and both are found to colocalize on the surface of the apical membrane patch (figure 4.1). The distribution of the proteins is similar to that of living cells, which suggests that the transfer of the apical membrane is faithful and therefore a suitable model system (figure 4.1 c-f).
Membrane staining was also used in fluorescence recovery after photobleaching (FRAP) experiments to check the integrity and fluidity of the membrane (see figure 4.3). Due to the strong membrane-substrate adhesion, the diffusion of lipids was expected to be impaired, however results of FRAP experiments show a complete recovery of the bleached area with a diffusion coefficient of $0.046 \pm 0.008\,\mu m^2/s$ (Mean±STD). This value is very similar to the results of FRAP experiments on the apical membrane of living cells, indicating that the fluidity of the membrane is still retained even on the solid support[125]. Additionally, the free mobility of membrane constituents is important for membrane mechanics, as stress can be transmitted across the whole patch in a similar way as it occurs in living cells. Thus, the FRAP results further underline the similarity between membrane patches and cellular membranes. Force indentation maps were acquired on membrane patches deposited on porous substrates, and the force-distance curves (FDCs) obtained from the center of each pore were evaluated employing equation 12. Figure 4.4 shows a collection of typical FDCs. FDCs on the rim and in the center of uncovered pores show a steep increase due to the stiff silica substrate, but differ in contact height by about 500 nm. The difference in contact height indicates the maximum indentation depth of covered

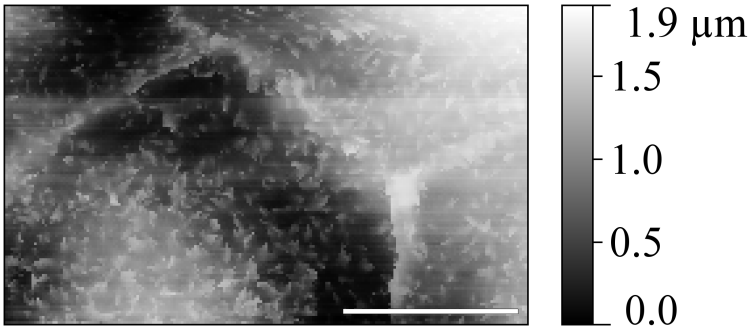

Figure 4.2 – Scanning ion conductance microscopy image of the surface of MDCK II cells after fixation with paraformaldehyde. Protrusions from the cell surface, i.e. microvilli, are visible as small bright feature. Scalebar: 5 µm.

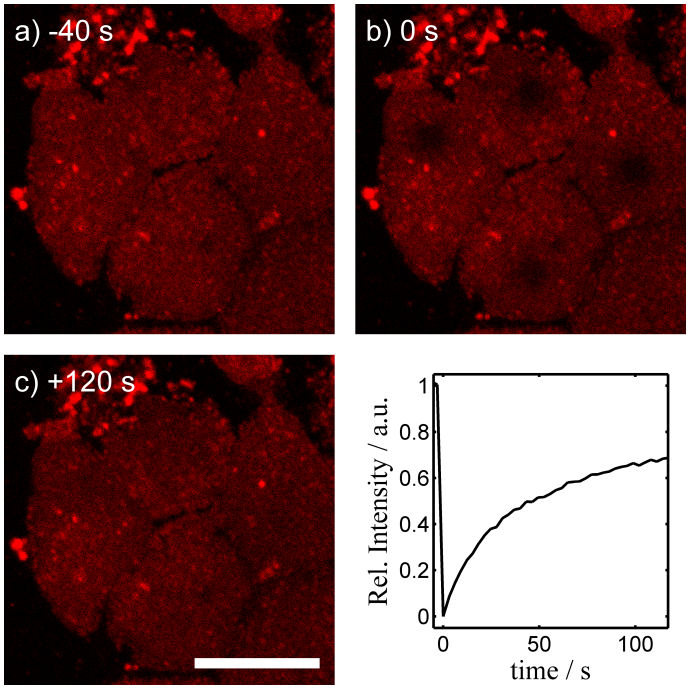

Figure 4.3 – FRAP of apical membrane patches. Shown are the fluorescence micrographs of membrane-labeled patches before (a) and immediately after bleaching (b). The fluorophores were bleached in 4 spots on 4 different patches. After 2 min a homogenous distribution of fluorophores was restored (c). Bottom right panel shows the average recovery of fluorescence intensity. Scalebar: 20 µm.

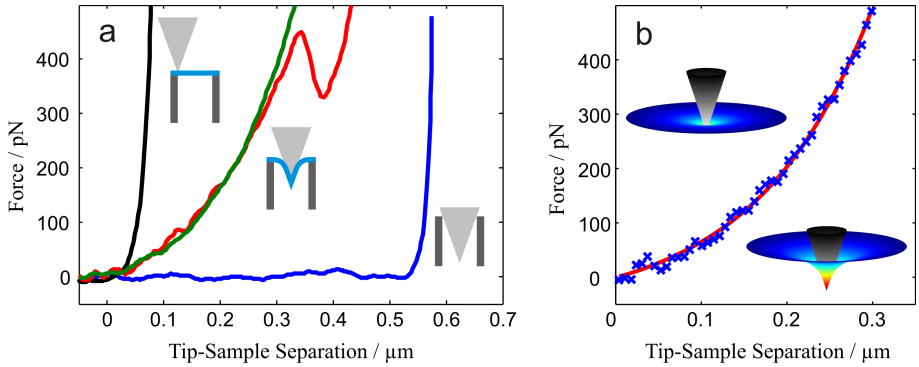

Figure 4.4 – Force-Distance curves (a) obtained from different locations on substrate-supported apical membrane patches. Indentations performed on the rim (black, left pictogram) as well as on empty pores (blue, right pictogram) show a very steep increase of force due to hard-wall repulsion. Indentations in the center of membrane-covered pores show a complex non-linear force response (red, green, mid pictogram). Membrane rupture is indicated as a sudden decrease of force (red). The fit (b, line) according to equation (4.10) nicely represents the experimental data (crosses). The results of the computation of membrane shape (small pictograms, jet colormap) during deformation by a cantilever (gray colormap) is shown for indentation depths of 100 nm (left) and 300 nm (right).

pore that can be assumed not to be influenced by probe-substrate contact, which is sufficient for all FDCs up to a force of 500 pN. FDCs on covered pores show a nonlinear force response to indentation, as expected from theory (equation (4.10)), where membrane stretching occurs and dominates. In some instances, rupture of the membrane sheet was observed as a sudden decrease in repulsive force (figure 4.4 a, red). Interestingly the corresponding holes are stabilized at a certain size and the FDC shows an increase of repulsive force again. This behavior is different from the force response of artificial bilayers, where rupture leads to the loss of the membrane spanning the pore[126]. Previous studies have shown that lipid bilayers are almost inextensible and show a linear increase in force to indentation in similar experiments[127]. The linear force response to indentation was attributed to pre–stress in the free-standing bilayer generated by a difference in free-energy between the free-standing part and the bilayer adhering to the rim, essentially reflecting the adhesion energy of the bilayer to the substrate per unit length. The stabilization of the FDCs after membrane rupture confirms the presence of a covering membrane in the first place and is also an indication of a characteristic difference in mechanical behavior of cells compared to artificial membranes, where membrane rupture results in the complete collapse of repulsive force and retraction of the membrane from the holes to the rim. It is conceivable that the presence of a cortex attached to the bilayer prevents large-scale rupture of the pore-spanning membrane, limiting hole growth by elastically decoupling of limited membrane areas covered by the actin mesh.

4.1.2 Tension Model for Membrane Covered Pores

After testing of the integrity of our prepared native membrane sheets we performed indentation experiments where we used an AFM tip to push the membrane into the substrates' pores. To determine the mechanical parameters as accurate as possible we developed a theoretical model that takes the detailed geometry of the experimental conditions using a conical indenter into account.
Since only a small layer of membrane and actin cortex remains after the preparation our system is prone to be evaluated according to the tension model. In this model, as briefly described in section 2.4, the repulsive force that rises due to area expansion of the layer in response to indentation equals

$$f = \int_0^{2\pi R} \left(T_0 + K_A \frac{\Delta A}{A_0} \right) \sin(\theta) \mathrm{d}s. \tag{4.1}$$

To evaluate this expansion a membrane profile has to be defined. A schematic drawing of the height profile with the given geometrical parameters is shown in section 4.1.2. The direction of forces has to be taken into account and is covered by

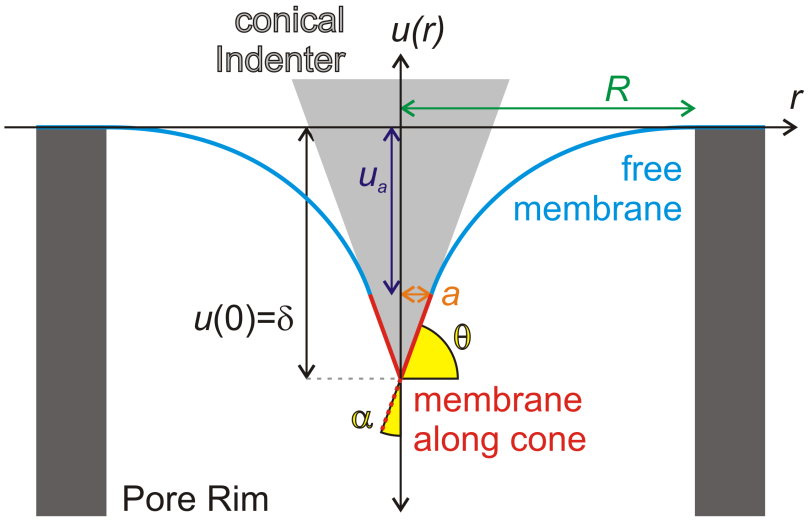

Figure 4.5 – Schematic picture of the important parameters for evaluation of membrane patches according to the tension model. Shown are the indenter (grey) that applies force on the membrane that originally horizontally spans the empty pore of radius R (green) from the rime edges (dark grey). Under load by indentation upto a depth of δ the membrane is separated into two parts, the central part of the pore attaches closely to the indenter (red) while the peripheral part minimizes the surface area (blue). The two parts of the membrane meet each other at $r = a$ and $u(r) = u_a$. The half-opening angle of the indenter equals $\alpha = 90° - \theta$.

$\sin(\theta)$ which represents the projection of the in-plane tension along the membrane onto the axial force exerted by the indenter. This angle is received via the membrane profile $u(r)$[128]:

$$\sin(\alpha) = \frac{\Delta u}{\sqrt{\Delta r^2 + \Delta u^2}} = \frac{\Delta u}{\Delta r\sqrt{1 + \frac{\Delta u^2}{\Delta r^2}}} = \frac{u'(r)}{\sqrt{1 + u'(r)^2}}. \tag{4.2}$$

To solve the membrane height equation we use the small gradient approximation $\sqrt{1 + (\nabla^2 u(r))^2} \approx \frac{1}{2}(\nabla u(r))^2$ for the energy functional $E = \int_{\Sigma_{\text{free}}} \mathrm{d}A_{\parallel} \left(\frac{T}{2}(\nabla u)^2\right)$ leading to the transverse load $q(r)$:

$$q(r) = T\nabla^2 u = T\left(\frac{\partial^2 u}{\partial r^2} + \frac{1}{r}\frac{\partial u}{\partial r}\right) \tag{4.3}$$

Given that the free part of the membrane is not under any load ($q(r > a) = 0$) any solution to this so-called Euler-Lagrange equation describes the real membrane height function with the solutions being:

$$u(r) = A_1 \ln(\frac{r}{R}) + A_2 \tag{4.4}$$

Solving the two constants with the postulated boundary conditions $u(R) = 0$ (the membrane height at the rim is exactly the surface) and $u(a) = u_a$ (to mark the radius at which the membrane separates from the indenter) we get:

$$u(r) = u_a \frac{\ln(\frac{r}{R})}{\ln(\frac{a}{R})} \tag{4.5}$$

Giving the additional boundary condition that the slope of the membrane functions free from the indenter and along the indenter must be the same at their contact point we see that:

$$u'(a) = \frac{u_a}{a \ln\left(\frac{a}{R}\right)} = -\tan(\theta) \tag{4.6}$$

Substituting this into equation equation (4.5) we eliminate u_a:

$$u(r) = -a \ln\left(\frac{r}{R}\right) \tan(\theta) \tag{4.7}$$

For any given indentation depth δ we can solve for a given the membrane height at $r = a$ to be:

$$u(a) = -a \ln\left(\frac{a}{R}\right) \tan(\theta) = \delta - a\tan(\theta) \tag{4.8}$$

This enables us to determine the membrane height profile for any given indentation depth δ and any given opening angle of the conical indenter. Consequently we can deduce the area change ΔA for any indentation by subtracting the original area $A_0 = \pi R^2$ from the sum of the cone area where the membrane is attached $A_{\text{cone}} = \pi as$ and the integral of the rotational symmetric body formed by the height profile to get

$$\Delta A = \frac{\pi a^2}{\cos(\theta)} + 2\pi \int_a^R r \sqrt{1 + \left(\frac{u_a}{r \ln\left(\frac{a}{R}\right)} \right)^2} \, \mathrm{d}r - \pi R^2 \tag{4.9}$$

since $s = a \cos(\theta)^{-1}$. Putting equation (4.2) into equation (4.1) we see that one can use

$$f = 2\pi \left(T_0 + K_A \left(\frac{\Delta A}{A_0} \right) \right) R \frac{u(R)'}{\sqrt{1 + u(R)'^2}} \tag{4.10}$$

to extract the apparent compressibility modulus K_A and the prestress T_0 based solely on the force-distance data and knowledge of the opening angle of the indenter $(90° - \theta)$ and the pores' diameter R.

4.1.3 Mechanics of Apical Membrane Sheets

Further investigation of membrane mechanics was performed by acquisition of FDCs in force maps with a lateral resolution of about 170 nm. For each measured pore the nine most central FDCs were selected and analyzed individually according to equation (4.10), providing T_0 and K_A for each force curve. The results were averaged to provide one parameter set per pore. The distribution of all parameters is shown in figure 4.6 as a histogram superimposed with a kernel density plot (solid dark line). Evaluation of the FDCs according to the tension model (see equation 12) allows to access the pre–stress T_0 and apparent area compressibility modulus K_A. The pre–stress of the isolated apical membrane sheets ($T_0 \approx 0.3\,\mathrm{mN\,m^{-1}}$) is similar to that of living MDCK II cells ($T_0 \approx 0.5\,\mathrm{mN\,m^{-1}}$[129]) from which the fragments originated.

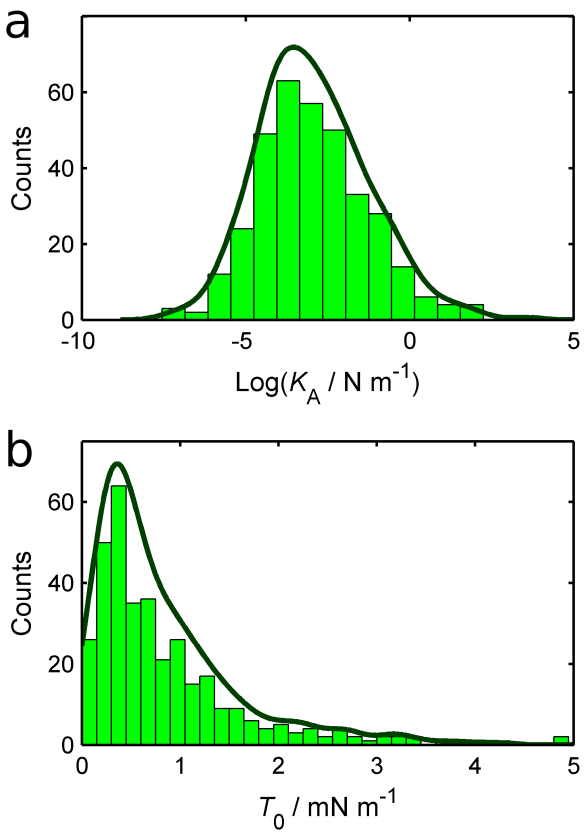

Figure 4.6 – Logarithmically scaled histogram of compressibility moduli K_A (a) and linear histogram of pre–stress T_0 (b) values obtained from isolated apical membrane sheets deposited on porous materials and subjected to central indentation. Distributions are shown as histograms (bars) with kernel density estimation (dark line). Total number of values is $n = 350$ with the highest probability at $K_\mathrm{A} = 27\,\mathrm{mN\,m^{-1}}$ and $T_0 = 0.36\,\mathrm{mN\,m^{-1}}$.

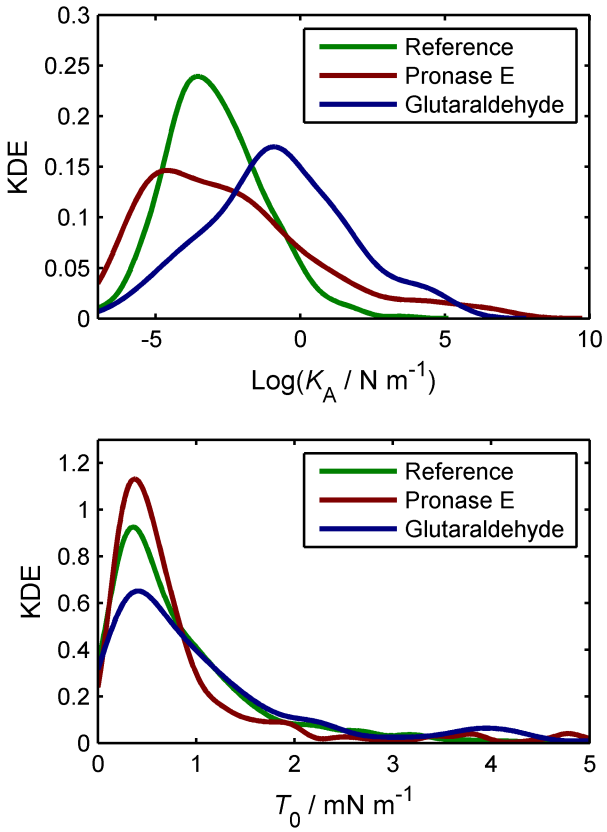

Figure 4.7 – Kernel density estimates of K_A (a) and T_0 (b) for the different treatments of apical membrane sheets. The apparent area compressibility modulus K_A is highest after treatment with glutardialdehyde (blue) and lowest after treatment with Pronase E (red), while untreated cells (green) show values in between. Pre–stress values T_0 are very similar regardless of the treatment.

However, due to the loss of cytoplasm and largely the cytoskeleton the pre–stress of the membrane sheets originates to a large extent from the membrane-substrate adhesion. The substrate is coated with a positively charged polymer, while the plasma membrane carries an overall negative charge. In contrast, pre–stress in living cells arises mainly due to the actomyosin cortex that contracts in the presence of ATP[17].

The area compressibility modulus of pore spanning membrane patches ($K_A = 27\,\mathrm{mN\,m^{-1}}$) is also similar to that of living cells, which was determined to be about $K_A = 130\,\mathrm{mN\,m^{-1}}$[129], supporting the idea of a largely intact plasma membrane. Although lipid bilayers are extensible up to a maximum of less than 5 %, structured membranes with microvilli should be able to supply their excess area to compensate indentation. The point-like structures as shown in the fluorescence micrographs (figure 4.1) indicate that the excess membrane areas are still available after the preparation process and thereby can be accessed during indentation, essentially reducing the area compressibility modulus K_A to $K_A \cdot A_0/(A_{ex} + A_0)$. Therefore,

we refer to apparent area compressibility moduli. A small value for K_A indicates larger accessible membrane reservoirs. The absence of functional myosin motors might increase the available excess area explaining why K_A values from membrane patches are smaller than those obtained from living cells[17].
In order to determine the range of mechanical responses of these membrane sheets, we applied two of the most extreme treatments, either using glutardialdehyde (GDA) to strengthen the protein network or Pronase E to digest peripheral proteins. Results of these experiments are shown in section 4.1.3. Glutardialdehyde is used to crosslink protein domains on the membrane cortex which stiffens the actin meshwork attached to the membrane to withstand expansion. This stiffening is mirrored in the area compressibility modulus as it rises from a peak at $18.8\,\mathrm{mN\,m^{-1}}$ for untreated samples to $152\,\mathrm{mN\,m^{-1}}$ after glutardialdehyde fixation. The same treatment shows almost no influence on the peak pre–stress T_0, which is $0.36\,\mathrm{mN\,m^{-1}}$ on untreated membranes and $0.37\,\mathrm{mN\,m^{-1}}$ after GDA treatment confirming the assumption that pre–stress is governed by substrate adhesion and not cortex composition.
Pronase E is used to cleave peptide bonds and thereby destroy protein structures accessable to the soluble enzyme. Incubation with pronase E should therefore weaken the cortical contractility and facilitate expansion during indentation. This weakening was indeed observed as the peak apparent area compressibility modulus K_A drops from $27\,\mathrm{mN\,m^{-1}}$ to $12.9\,\mathrm{mN\,m^{-1}}$. However, the distribution in this case is rather broad and seems to have a shoulder on values even higher than untreated samples. It is possible that cortical integrity is actually important for force transmission along the plasma membrane, and destruction of this cortex leads to an increased inhomogenity of surface properties from a mechanical perspective of view. Besides, removal of actin mightalso interfere with accessibility of membrane reservoirs and thereby increase the stiffness at large strain. Regardless of this, the peak pre–stress T_0 stays quite constant at a value of $0.41\,\mathrm{mN\,m^{-1}}$ which again indicates that pre–stress after the given preparation process is largely independent of cortical composition and reflects mainly the adhesion to the pore rims.
These findings suggest that isolated membrane sheets exhibit a mechanical behavior similar to that of plasma membranes of living cells. This supports the concept of a tension-based mechanical model that is able to describe the mechanics of apical membranes of both, in living cells and isolated fragments, and confirms and quantifies expected changes of mechanics due to cortex modifications. The change of the compressibility modulus independently of pre–stress underlines that two independent parameters are required to characterize the mechanical response of membranes to surface expansion during indentation instead of using an uniform parameter like the Young's modulus.

4.2 Studies on Confluent MDCK II cells

4.2.1 Shape Inhomogeneties within Confluent Layers

After validation of the tension model the goal was to further apply tension-based analysis to living samples. The main question addressed in this work was whether geometrical features like the cells' size and geometry leave a footprint in the mechanical properties on the cells' surfaces. Since the MDCK II cell line was already studied successfully in force indentation experiments the same line was chosen to study the impact of size and shape on cellular elasticity as well.
Confluent MDCK II layers were subjected to geometrical analysis to get a better grip on geometrical features within the layer. Instead of identification of vortices and drawing of straight lines between those as described in section 2.5 we instead identified the actual cell contact lines (including the vortices) and used those for

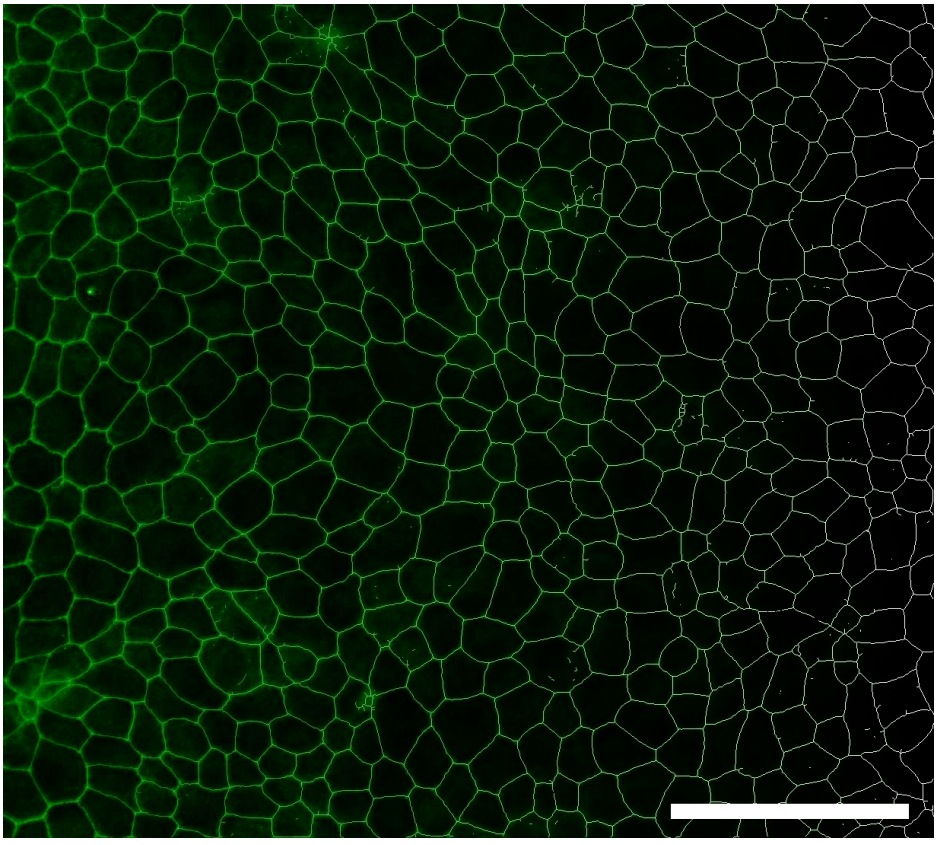

Figure 4.8 – Example of the first step of cell segmentation. Fluorescence images of ZO-1 stainings (left) are processed by thresholding and skeletonized, dead ends were removed and lead to thin lines of cell-cell contacts (right). Scalebar: 100 µm.

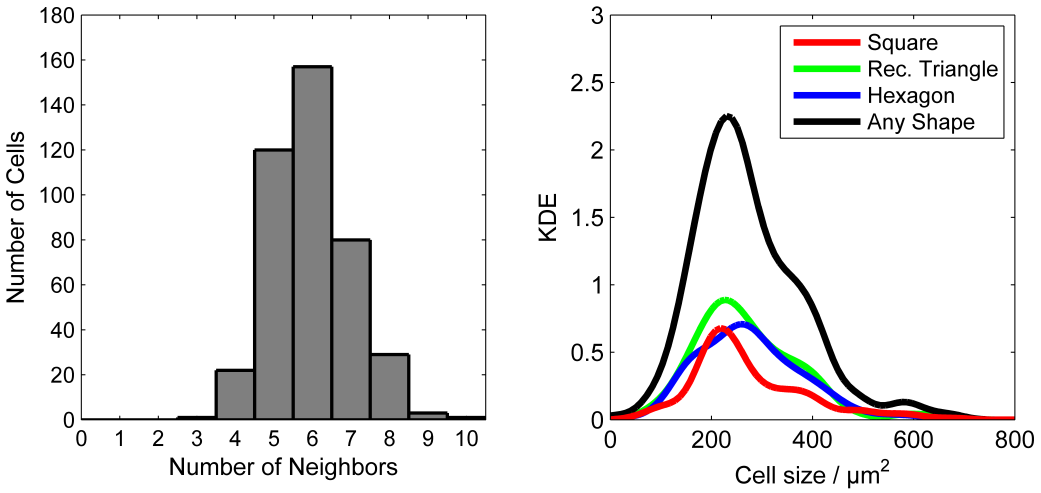

Figure 4.9 – Histogram of the number of neighbors per cell detected (left). The majority of cells show between four and 8 neighbors, with 5.96 being the average amount ($N = 413$). Kernel density estimates of projected areas, as read out from ZO-1 stainings, show an overall average cell area of 278 µm^2 in a unimodal distribution (black line, right). The categories of subpopulations, attributing each cell to the closest ideal shape, are also shown (colored lines, $N_{\text{blue}} = 127$, $N_{\text{green}} = 177$, $N_{\text{magenta}} = 204$). The kernel density distributions are scaled according to the total amount of data represented, hence the colored lines sum up to yield the black line.

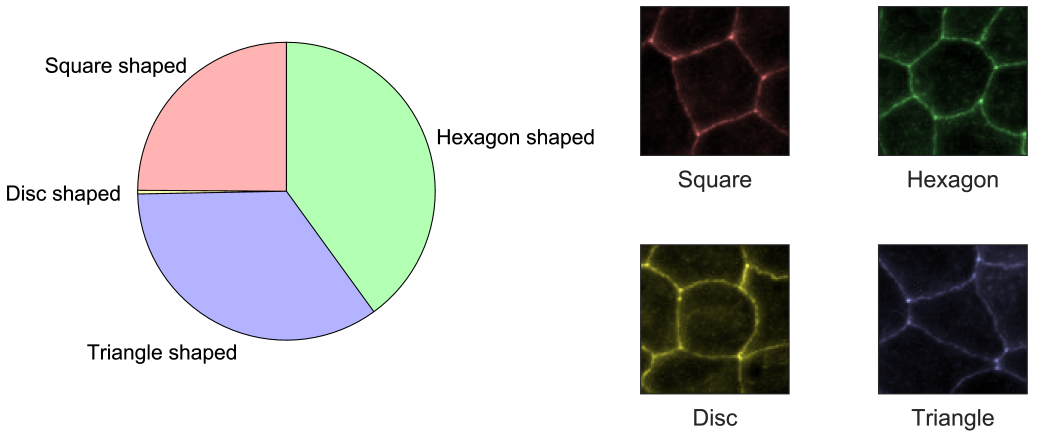

Figure 4.10 – Pie chart showing the fraction of cells that show maximum overlap with either square ($N = 127$), disc ($N = 2$), rectangular triangle ($N = 177$) or hexagon ($N = 204$). Note that only two of the analyzed cells show maximum overlap to circles, and these two even show the exact same overlap with a reference square. ZO-1 stained images of example cells for each of the reference patterns are given on the right, each showing a 32 µm x 32 µm window.

further analysis. Not only will this give more accurate results but it also allows more complex shapes to be recognized.
To do so we used images of ZO-1 stainings of fixed samples, applied an intensity threshold and skeletonized the received cell contact lines to get the most accurate central line (see figure 4.8). We further extracted cellular nuclei from images of DAPI stainings of the same area to identify and verified that within every cell border only a single cell was present. Knowing the cell's position and borders, the number of cell contact vortices was determined showing that cells touch on average six vortices, hence meeting six neighboring cells, which is in good agreement with studies on other tissues[130]. An average cell size of 278 μm^2 was found (see figure 4.9).
To test whether six neighbors also result in hexagonal cell shape, every cell was compared to a square, disc, triangle and hexagon of the same size. For each reference shape, the actual cell data were rotated and translated until the highest number of overlapping pixels was reached, this number was defined as overlap. Afterwards, cells were categorized into four populations characterized by their highest overlap, hence every cell that had the highest overlap with an ideal square was tagged as a square cell. While the hexagonal shaped cells pose the largest partition of the overall number of cells they represent less than 50 % of all cells (see figure 4.10). This emphasizes the geometrical diversity within cell layers as also reported in other studies.[118]
It is also worthwhile to check the dependency of area and number of neighbors, reflecting the order of the polygon class (figure 4.11). In general, larger cells tend to have more neighbors attached, which is reasonable since more average sized cells are needed to surround particularly large cells. In our studies on MDCK II cells the correlation between size and number of neighbors is much weaker than in a comparable study of Farhadifar *et al.*[119] on drosophila wing tissue. In their vertex model a small correlation coefficient could be caused by a higher compressibility of

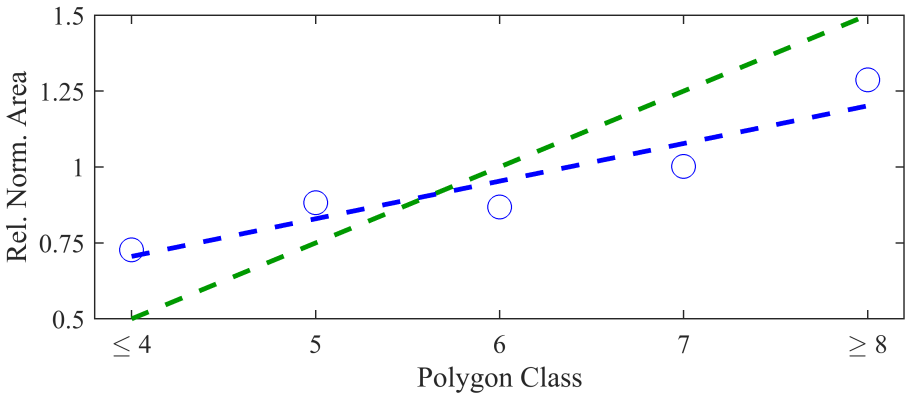

Figure 4.11 – Correlation between the average size of cells of a given polygon class $\overline{A_n}$ divided by the overall average size of cells $\overline{A_{\text{tot}}}$ and the polygon class n (blue circles). The Polygon class denotes the number of neighbors of each given cell. The blue dashed line represents a linear fit to the circled data points, while the green dashed line represents results from similar studies in drosophila wings during development.[119]

cells, hence compressibility dominates pattern formation and organization of confluent cell layers.
These results show that the shape and size heterogenity in the investigated MDCK II layers are fairly pronounced and further investigations of the connection between compressibility moduli and these heterogenities were performed.

4.2.2 Contact Point-free Young's Moduli

As discussed in section 2.4, cellular mechanics are often treated as a deformation of a semi-infinite space with a Poisson's ratio ν by a rigid indenter. Such deformations are characterized by the Young's modulus E[15], which in the case of a conical indenter with half-opening angle θ results in a repulsive force f due to indentation δ according to

$$f = \frac{2E\,\tan(\theta)}{\pi(1-\nu^2)}\,\delta^2. \tag{4.11}$$

In typical force spectroscopy experiments a force setpoint is given and indentation is continued until the force setpoint f_{SP} is reached, hence all acquired data share roughly the same maximum force but different indentation depths. The equation above is only true during contact between probe and samples and does not apply to regions of the force distance curve without contact. To evaluate FDCs without knowledge of the contact point we use the integral of the whole curve, which is invariant to the length of the non-contact region.

$$E_{\mathrm{elast}} = \int_0^{\delta_{\mathrm{SP}}} \frac{2E\,\tan(\theta)}{\pi(1-\nu^2)}\,\delta^2\,\mathrm{d}\delta \tag{4.12}$$

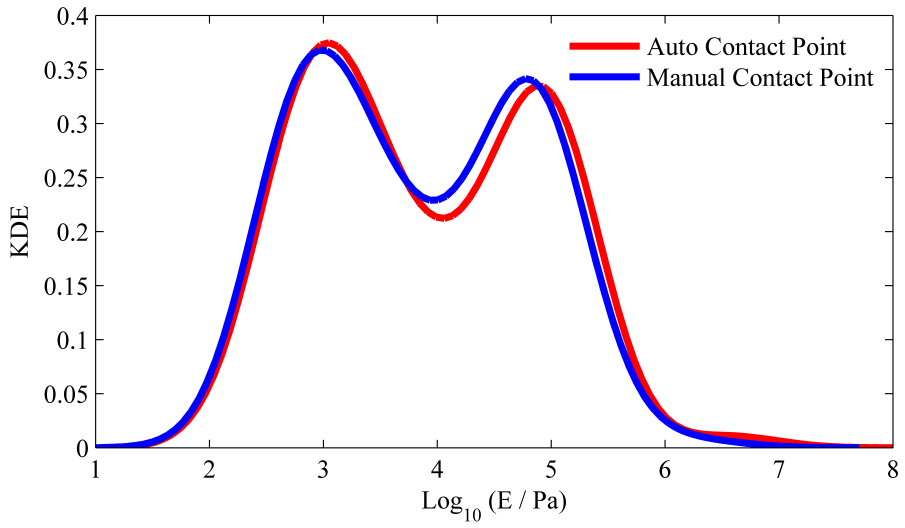

Figure 4.12 – Kernel density estimates for the same sample of force distance curves that were either evaluated by manual chosen contact points or via their elastic energy, essentially being an automated contact point recognition. Sample includes 629 datasets.

We know that indentation depth at the force setpoint equals

$$\delta_{\mathrm{SP}} = \sqrt{\frac{f_{\mathrm{SP}}\pi(1-\nu^2)}{2E\,\tan(\theta)}}. \tag{4.13}$$

Together with equation (4.12) the Young's modulus can be obtained from the elastic energy E_{elast} via

$$E = \frac{f_{\mathrm{SP}}^3}{18\,E_{\mathrm{elast}}^2\,\tan(\theta)}\pi(1-\nu^2). \tag{4.14}$$

To verify the reliability of this approach we used the contact point-independent evaluation on a sample that was also evaluated by manually chosen contact points and see very good agreement between the two methods as shown in figure 4.12.

4.2.3 Area-Stiffness Correlation

Knowing the broad distribution of cell sizes and shapes we decided to further investigate if there is any correlation between cellular geometry and the stiffness of cells. Due to the low amount cells with close to an ideal shape in a wildly grown confluent cell layer, we focused on correlations between in-plane cell size, i.e. projected area, and their surface mechanics.
Using the integral of entire force distance curves, the Young's moduli in large samples can easily be obtained, so forcemaps with a pixelsize of 1 μm^2 were acquired and

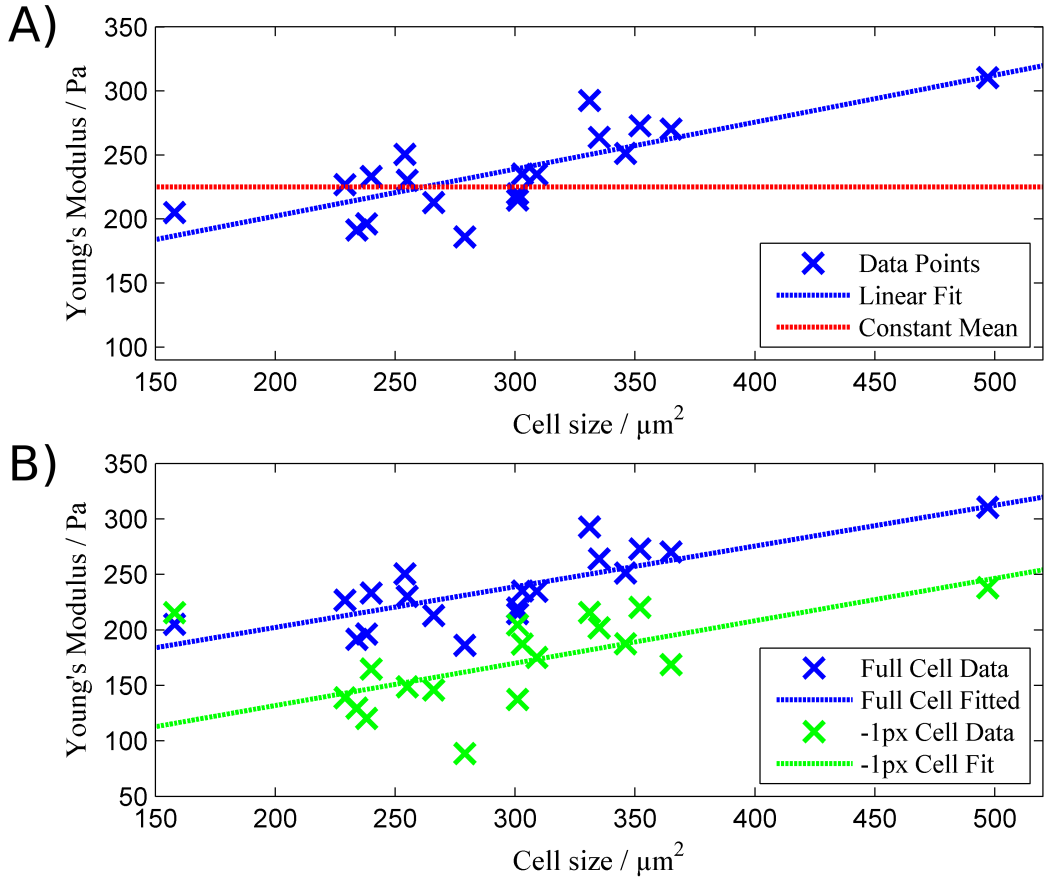

Figure 4.13 – A) Correlation between the in-plane projected cell size and the observed Young's Modulus (blue crosses). A roughly linear trend is recognizable and was determined to exhibit a slope of 443 mPa/μm^2 (blue dashed line), while independent parameters should result in no slope at all (red dashed line, marking the mean modulus). A correction of the moduli can be made by either extracting the difference of the moduli from the linear regression (blue) or their overall mean value (red). Each of the 19 data points includes one FDC per μm^2 of the respective size, resulting in a total of 5593 FDCs. B) To show that the increase in stiffness does not rely on a different ratio between area and circumference for differently sized cells, data for cells ignoring the most distant pixels, essentially ignoring the perimeter (green), still shows a strong correlation between the two.

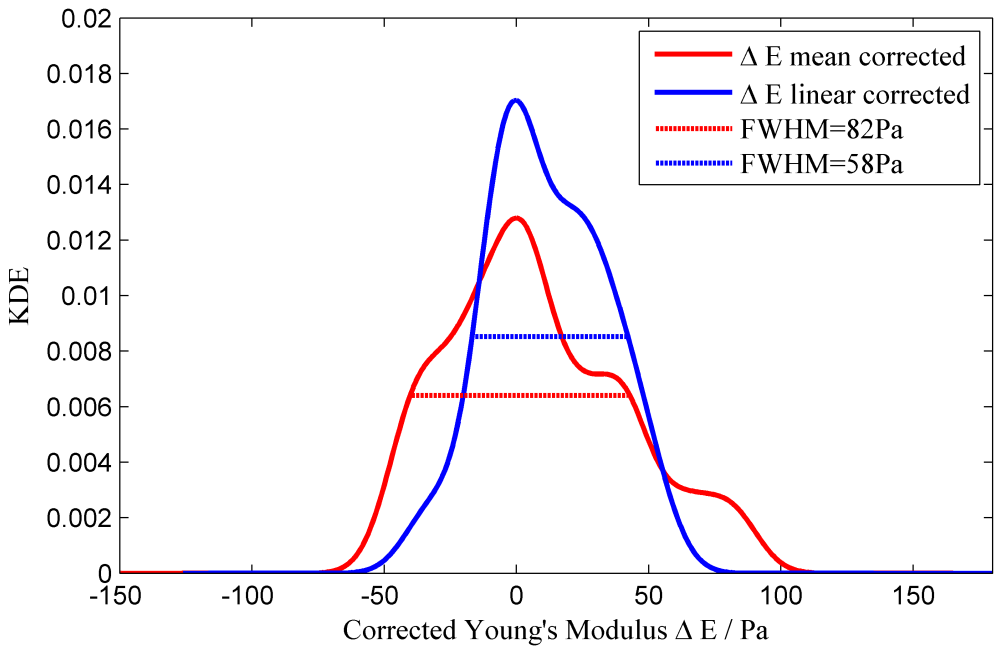

Figure 4.14 – Kernel density estimates of the difference of the Young's modulus ΔE from either their mean values (red) or their corresponding value of the linear regression (blue, see figure 4.13 top panel). As shown the full width at half maximum FWHM of the distribution decreases from 82 Pa to 55 Pa.

evaluated. Dependency of the median Young's modulus on the cellular size is shown in figure 4.13, where the modulus increases by about 50 % from a size of 200 μm^2 to 400 μm^2 with absolute values that are in good agreement with studies of Harris *et al*[131].

Previous studies have shown that in indentation studies the cell-cell contacts typically behave stiffer compared to the central part of the cell.[110] For larger cells, the ratio between circumference and area is smaller and the contribution of cell-cell contacts therefore also smaller. However,the exclusion of the perimeter data for each individual cell in the evaluation of the area-stiffness correlation still shows a very similar correlation. This shows that the observed correlation is not due to geometrical artifacts but actual difference in apical membrane mechanical properties.

Knowing this correlation, the observed stiffness can be corrected by the size-dependent part to lower the width of value distributions and consequently increase the quality of studies performed on confluent grown cell layers. This correction is shown for the given example data in figure 4.14 where a decrease of the width by about 10 % was achieved. Note that especially outliers of the distributions are reduced as those are affected by the correction the most.

Besides increasing the quality of such studies' parameter distributions this also brings up the question whether known changes of surface mechanics due to drug treatment are caused by apical reorganization, indirectly connected to a change of average cell

surface e.g. due to increased cell exclusion from the layer following the treatment, or both. Also it is interesting whether the cell size is mediated by the membrane mechanics or the size itself determines the mechanical behavior. While the latter question will remain for further studies, this work will investigate cell under tight control of their shape by nanoindentation experiments in conjunction with advanced mechanical analysis to address the former one.

4.3 Single Patterned MDCK II Cells

4.3.1 Morphology of Single Cells

Given the results that a diverse distribution of cellular sizes and shapes within confluent MDCK II layers is evident and that there is a link between size and mechanics of cells we investigated the influence of geometry on cellular mechanics reproducibly. Using a micropatterning technique enabled us to force cells into given geometries by coating a surface with Collagen I in areas where cellular adhesion was desired, while the majority of the surface was coated with a non-adhesive polymer (see section 3.2). Unfortunately, the formation of a confluent layer of MDCK II cells ignores the adhesive cues of the surface probably due to strong cell-cell-adhesion, which is why it was necessary to use single adherent cells for proper patterning results.
To properly isolate single cells on patterned culture surfaces single instances of the patterns were separated by at least 40 µm of distance. The non-adhesive compound was conjugated to a tetramethylrhodamine-isothiocyanate (TRITC)-moiety to allow validation of cellular adhesion during every experiment while not altering cell behavior. Topographical images of patterns show a height difference of +5 nm of the Collagen I coating compared to the non-adhesive area (figure 4.15). This ensures that mechanical properties of cells are not altered by any framing effects on the border between the two polymers as could be the case for patterns of cavities[132].
To get a proper idea of the size range that was to be investigated we analyzed single cells stained for membrane that grew on a completely Collagen I coated surface. Cell

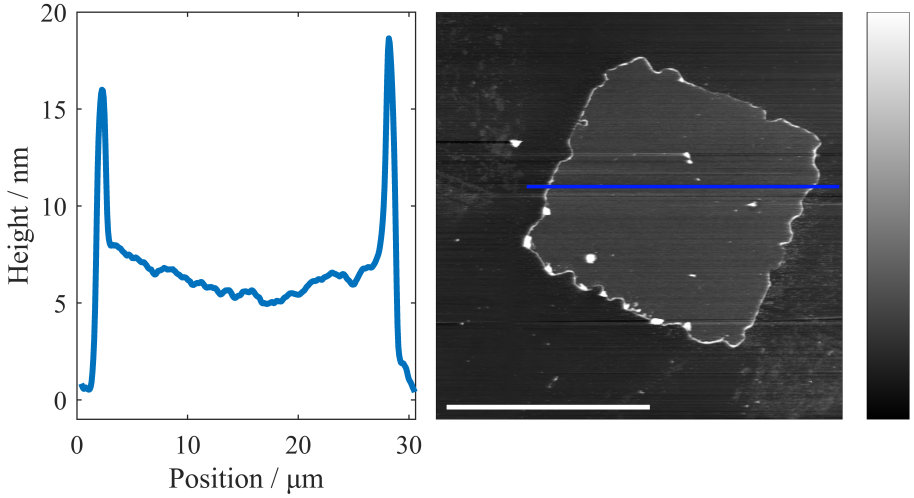

Figure 4.15 – Linescan (left) along the fast scanning direction as shown in the topographical AFM image (right). The elevated pattern consists of Collagen I bound onto a culture dish surface, while the lower surrounding is coated with non-adhesive polymer. While the perimeter is elevated by about 30 nm, the face of the pattern is less than 10 nm above the outer surface. Scalebar: 20 µm, colorscale: 69 nm.

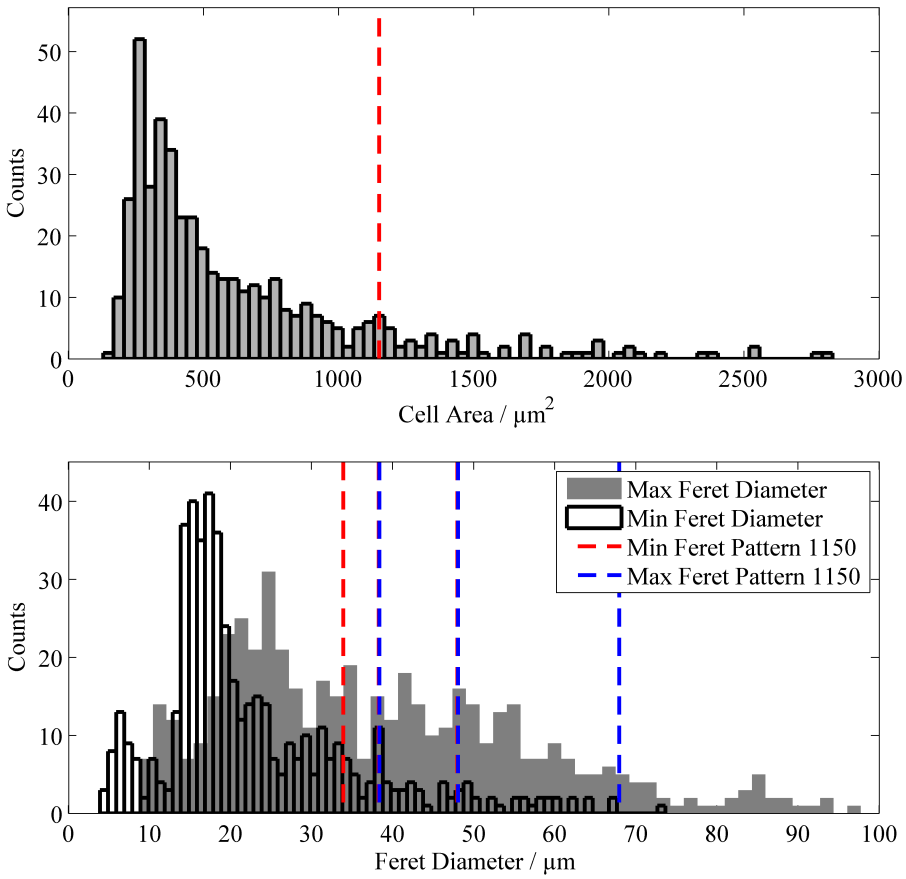

Figure 4.16 – Histograms of cell area (top) and maximal and minimal feret diameter (bottom, filled grey and empty bars with black border respectively) of single adherent MDCK II cells. Marks are given to compare the distributions to values of medium-sized cell patterns. There is only a single line in the top histogram as shapes of 1200 µm² are regarded, but there are multiple lines for the different feret diameters in the bottom plot since these depend on the shape even at equal total areas.

nuclei were stained and dual-channel images were analyzed according to section 3.8. The distribution of cell adhesion area is presented in figure 4.16, however, it is important to note that unpatterned cells tend to form very anisotropic shapes. Therefore, in addition to the determination of cell sizes we also analyzed the minimal and maximal possible distance between two tangential lines touching the circumference of the cell area (feret diameter). While the overall shape of the size distribution is similar to that of confluent cells, that of single spreading cells is shifted to larger areas. This effect is probably due to the fact that only lateral projections of the cells are represented, so while the volumes are probably similar in both conditions, spreading cells are rather flat and have therefore larger projection areas.
Interestingly, cells seeded on matrix patterns covering a total area per instance similar to the cell areas of freely spreading cells, cells did not manage to properly spread on these patterns (see figure 4.17). One possible reason for this might be that the

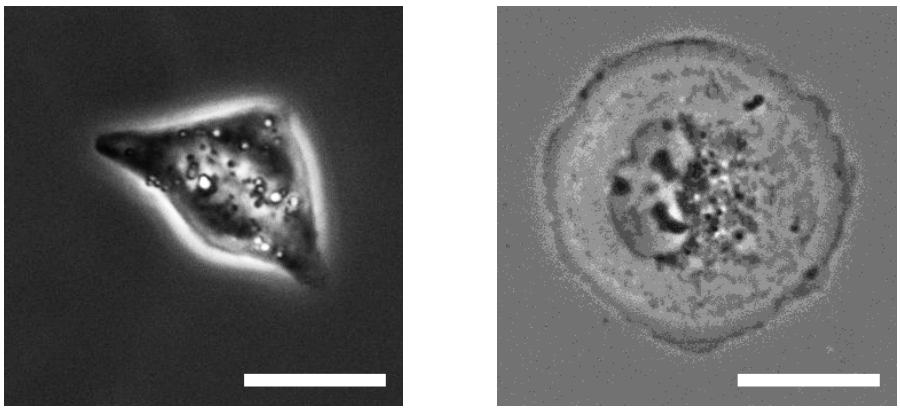

Figure 4.17 – Phase contrast images of patterned cells that are adapting the shape of a small rectangular triangle (left) and a large disc pattern (right). The bright areas around the triangular cell indicate areas of high slopes and an elevated cell body. Scale bar 20 µm.

maximal feret diameter of our desired shapes was small compared to the area due to the high symmetry of these patterns, and that small feret diameters in turn might be badly accepted by cells during the spreading process. The high symmetry was chosen to be used in the evaluation of later experiments and to allow averaging of individual cells, resulting in better statistics and more reliable results. The early spreading state however leads to cells that mostly retain their spherical shape independent of the underlying pattern. Because of that we chose to use larger patterns and focus on cells that spread properly.
Since the excess membrane area, stored in protrusions like microvilli, is believed to be of major importance for the mechanical response of cells to indentation of their apical surface the proper polarization of the freshly spread cells was verified (see figure 4.18). Staining of an apical marker that is only pronounced in cells with an axial polarization show a high recognition of proper motifs on the single cells by the antibody. Additional staining of f-actin also shows that stress fiber formation on the bottom of the cells takes place while dot-like structures on the apical surface emerged. These dot-like structures are known to often resemble microvilli, since these very small and finger-like protrusions are mechanically supported by f-actin to counter in-plane tension along the plasma membrane and facilitate the formation of increased surface area. The stress fiber formation on the basal side is mainly pronounced alongside straight sections of the matrix patterns, and only minor fibers are present at disc-shaped cells.
In addition to immunofluorescence stainings, topographical images were taken (figure 4.19). The cells adapt the shapes of the adhesive substrate by formation of thin lamellipodia at the periphery, but also maintain a considerable amount of membrane ruffles. While storages of membrane area are often sacrificed during initial spreading they are rebuild soon after.[133] Experiments were performed intentionally after these structures are regained to ensure that cells already reached a kind of dynamic equilibrium and results are not too much influenced by temporal variation. The cells' nucleus is located under the highest part of the cells, which is best visible for

rectangular triangular cells. These triangles have the shortest profile going through the patterns' center and the middle of the hypothenuse, which causes the steepest slope from the substrate to the high nucleus.
Knowing the range of adhesion areas and the shapes that were to be investigated, we decided to determine one of the biggest differences between single spreading and confluent epithelial cells, namely the cell cycle activity.[134, 135] It is a reasonable assumption that after staining the nucleus with DAPI (see section 3.3) the detected fluorescence intensity in the corresponding bandwidth is proportional to the amount of DNA in the given pixel.[136, 137] The integral over a particular nucleus in an image is therefore proportional to the total amount of DNA inside the cell. Since

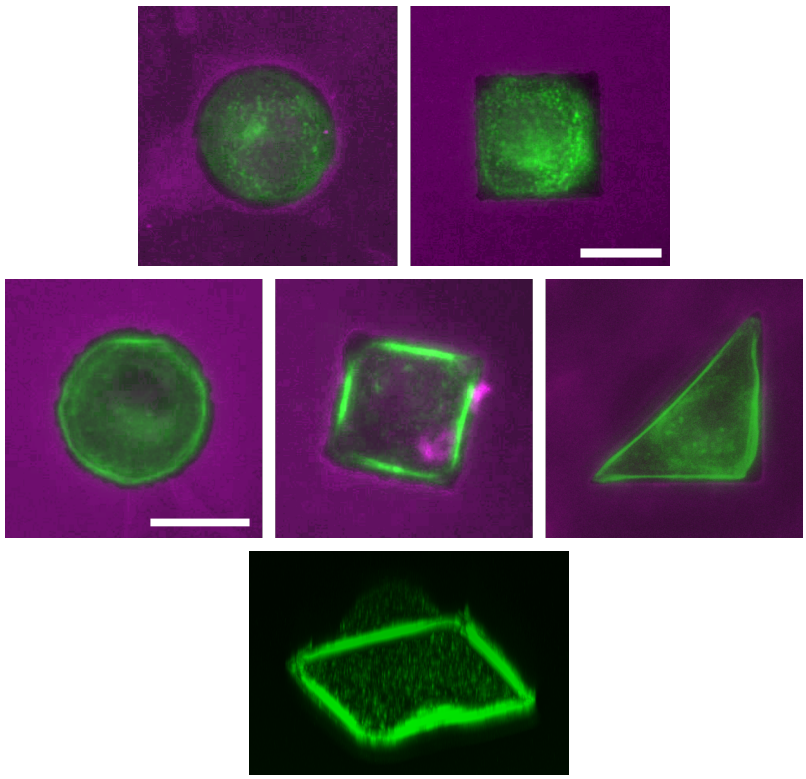

Figure 4.18 – Epifluorescence micrographs of patterned cells. The non-adhesive area (magenta) is coated with a fluorescently labeled polymer to visualize the patterns, while an apical marker is labeled via immunochemistry (top row). The apical marker is binding in good quantities and reveals small structures. The corners of the square-shaped cell are barely stained which might occur due to the fact that the corners are forming the latest since they are usually the furthest away from the initial adhesion and hard to form due to the their high curvature. The distribution of f-actin (green, mid row) shows the formation of stress fibers predominantly on the cell edge. This leads to the formation of a ring-like structure for the disc-shaped cells, in the case of square-shaped cells the straight edges are supported by strong stress fibers while the corners are not well defined and seem to feather. A 3D-representation of confocal fluorescence stack images of the f-actin distribution in square shaped cells shows the elevated central region of the cells containing dots of high intensity while stress fibers frame the cell on the bottom and perimeter of the pattern. Scalebar: 20 µm.

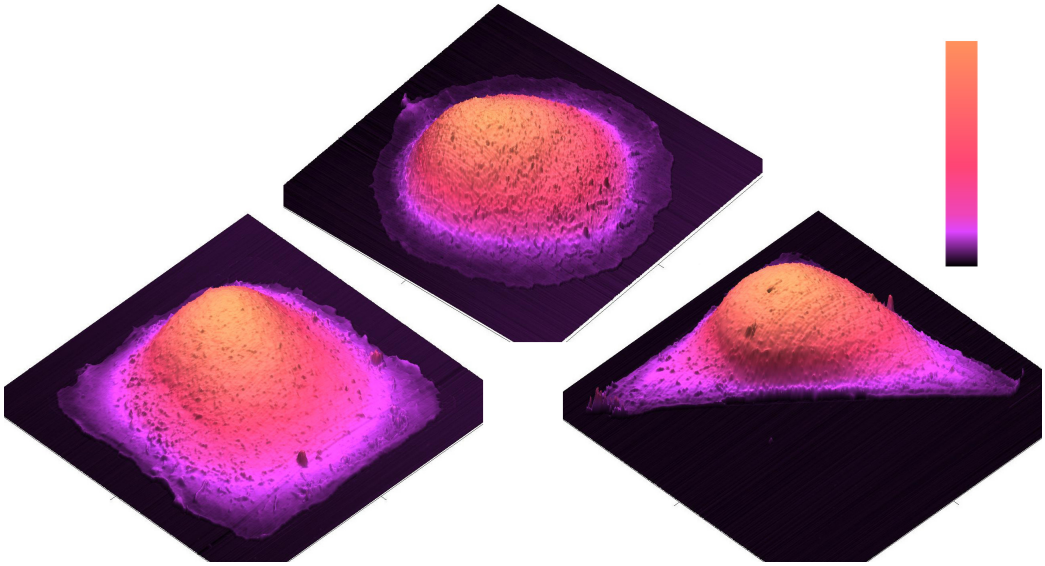

Figure 4.19 – Topographical images of patterned MDCK II cells grown in shapes of discs, squares and triangles. The image dimensions for the disc cell is 44 µm x 44 µm in lateral direction and 5.9 µm peak height, for square cell 42 µm x 42 µm in lateral direction and 6.4 µm peak height and for the rectangular triangle cell 60 µm x 60 µm in lateral direction and 5.0 µm peak height. Color tables are non-linear to emphasize the small structures on the cells' surfaces, e.g. microvilli. Images are corrected for baseline plane and artifacts.

cells undergo the cell cycle during proliferation in which their DNA is doubled in S-Phase, the amount of DNA in cells is somewhere between the single and double set of DNA, with only few cells showing intermediate DNA content. The higher the proliferation rate the more cells are tetraploid and show high DNA intensities. This principle is used to determine the cell division activity for suspended cells in flow cytometry experiments[138, 139, 140], however since we were using adherent cells we acquired representative fluorescence images and applied automated image analysis.[141] In the latter case three populations of cells exist with either a single set of chromosomes (Anaphase, Telophase, G_0 or G_1 phase), double set of chromosomes (G_2 Phase, Prophase, Metaphase) and cells in-between the two populations (S-Phase). The obtained results are presented in figure 4.20 and show that for confluent cells only a tiny fraction entered G_2 Phase which is to be expected since upon reaching confluency cells become contact inhibited and arrested in G_0 for the most part. Conversely, the patterned cells show much higher activity even a single hour after seeding, which might cause increased heterogenity in experiments of such cells.

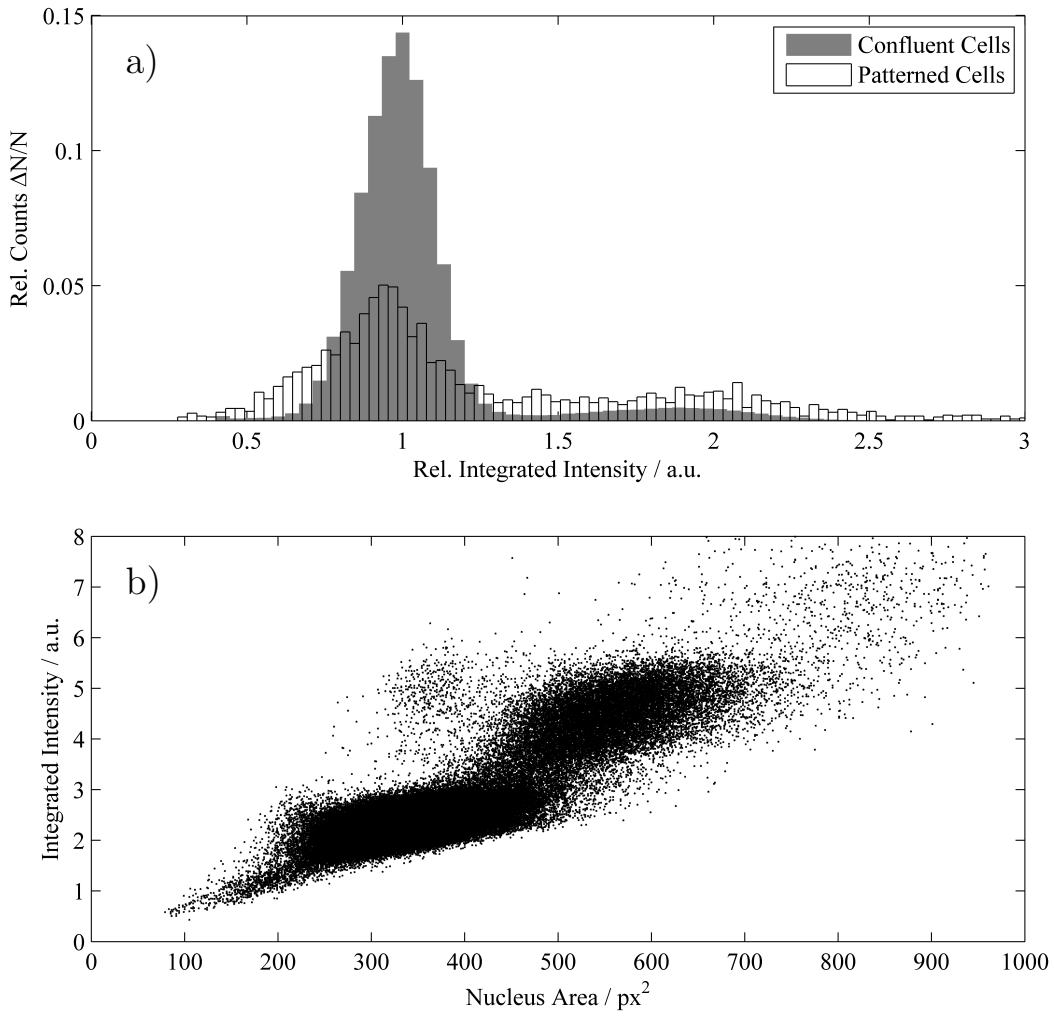

Figure 4.20 – Histograms of the nuclei intensity of confluent (grey) and patterned cells (framed). The intensities are normalized to their individual first peak of the bimodal distribution while the relative counts are normalized to the number of cells included in the particular histogram (a, $N_{\text{Confluent}} = 533705$, $N_{\text{Patterned}} = 2829$). Additionally the integrated intensities of confluent cells are plotted against the lateral projection of their nuclei areas (b) are shown to prove that the bimodal distribution of intensities corresponds to actually different DNA content and is not simply an artifact following a bimodal projection area distribution.

4.3.2 Tension Model for Patterned Cells

The same tension model as already described in section 2.4 and section 4.1.2 was also applied to access the same parameter sets for patterned cells. However, in the latter case the investigated FDCs should not be limited to only central indentation since the goal was to acquire a laterally resolved parameter map for each of the patterns. Additionally the cell surface itself is no longer even remotely rotationally symmetric. Both of these conditions demand a much more complex surface function to exactly evaluate the area dilation during indentation. In the context of this work, however, we will instead use a rough approximation since the definition of an exact and correct surface function is extremely difficult and includes a high risk of getting unpredictable artifacts due to the wrong assignment.
The geometry we consider does not take any boundary conditions into account and hereby will only give area compressibility moduli per involved surface area K_A/A_0. A schematic drawing of this model is given in figure 4.21 marking all the relevant geometrical parameters.
The force balance in this case exists just where the indenter meets the original membrane height $r = \delta \tan(\theta)^{-1}$ where the projection of in-plane tension onto axial direction of force is transferred simply by $\sin(\theta)$. Thus the basic force equation reads

$$f = \int_0^{2\pi r} T \sin(\theta) \mathrm{d}s = 2\pi T r \sin(\theta) = 2\pi\delta \cos(\theta) \left(K_A \frac{\Delta A}{A_0 + A_{\mathrm{ex}}} + T_0 \right). \qquad (4.15)$$

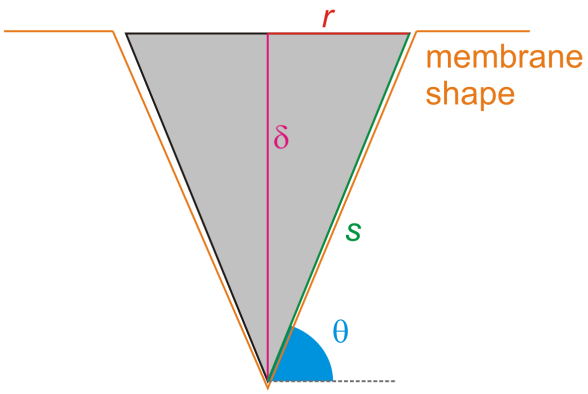

Figure 4.21 – Scheme of the indentation of a planar membrane. The membrane (orange) is touching the indenter (grey) at every point where the indenter crosses the original horizontal membrane plane. Indentation of a depth δ is therefore influencing the membrane within a radius of r depending on the half opening angle of the conical indenter $90° - \theta$ resulting in a surface increase of $\pi r s - \pi r^2$.

The area change ΔA during indentation is depending on δ according to

$$\Delta A = A_{\text{cone}} - A_{\text{disc}} = \pi r s - \pi r^2 = \frac{\pi \delta^2}{\sin(\theta)\tan(\theta)} \left(1 - \cos(\theta)\right). \tag{4.16}$$

Inserting this expression into equation (4.15) and defining $\tilde{K}_A = K_A \left(A_0 + A_{\text{ex}}\right)^{-1}$, since we do not have any information about A_0 included in this model, we end up with an expression describing the force f depending on the indentation depth δ as follows:

$$f = 2\pi T_0 \cos(\theta)\delta + \frac{2\pi^2 \tilde{K}_A}{\tan(\theta)^2}(1 - \cos(\theta))\delta^3 \tag{4.17}$$

4.3.3 Apical Cell Mechanics of Patterned Cells

After successfully establishing the patterning of MDCK II cells and evaluating the adhesion area space to be probed we chose to investigate the mechanical properties of cells in square, circular and rectangular triangular shapes of 900 μm^2. Since laterally resolved parameter maps of the mechanical responses can be obtained with statistical accuracy by averaging multiple cells of the same pattern this study should show whether or not shape features alter the surface mechanics of cells. Furthermore, we performed experiments on square and disc shaped cells of 1200 μm^2 to check if adhesion size has an overall influence on surface mechanics and if shape relations are depending on adhesion size. Lastly we performed experiments on disc shapes cells of 1500 μm^2, marking the upper end of realizable adhesion sizes to further check for size dependencies.

The size dependency that was observed in confluent cells turned out to be a rather small trend when comparing increasingly large disc-shaped cells, as shown in figures 4.22 and 4.23. In terms of the Young's modulus and compressibility modulus the center of the investigated cells was generally softer than their perimeter, while at

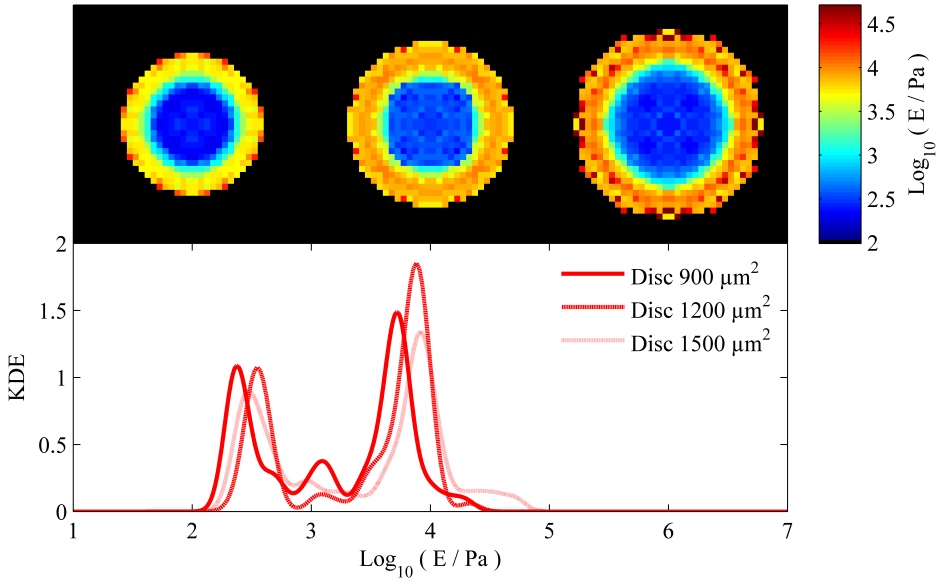

Figure 4.22 – Logarithmic representation of mean Young's moduli of disc-shaped cells in sizes of 900 μm^2, 1200 μm^2 and 1500 μm^2 (color-scaled maps, from left to right, $N = 2834, 2924, 2362$). Pixel resolution is 1.5 μm^2x1.5 μm^2. The bimodal value distribution can be addressed to geometrical features of the cells, namely the softer center and the stiffer peripheral region. Although barely visible in the kernel denstiy estimates the increasing stiffness especially of the peripheral regions is clearly visible in the laterally resolved parameter map, underlining the importance of the statistically relevant spacial resolved information that is only accessible due to the reproducible adjustment of cell patterns.

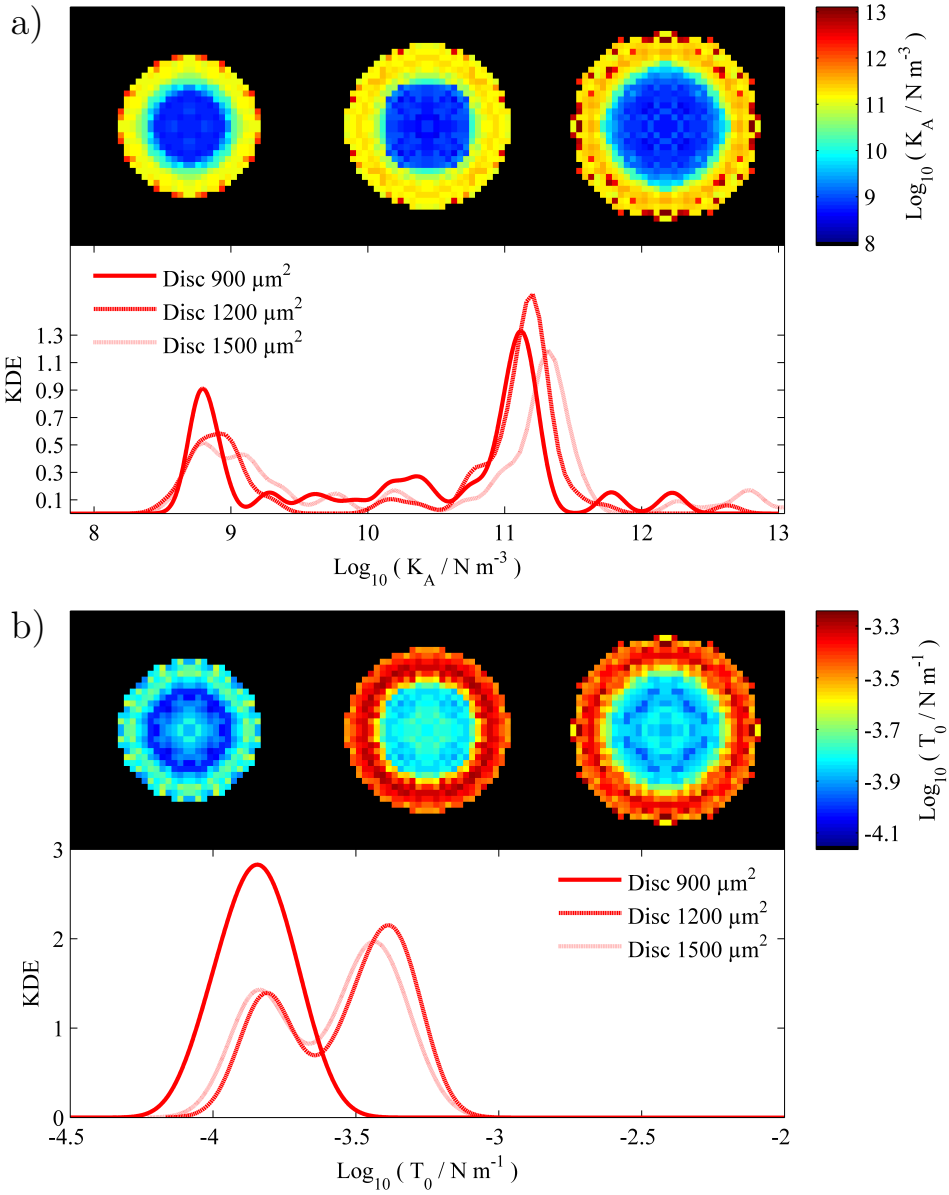

Figure 4.23 – Logarithmic representation of mean area compressibility K_A (a) and prestress T_0 (b) values of disc-shaped cells in sizes of 900 µm^2, 1200 µm^2 and 1500 µm^2 (color-scaled maps, from left to right, $N = 2834, 2924, 2362$). Pixel resolution is 1.5 µm^{2}x1.5 µm^2. The logarithmic kernel density distribution of all values (bottom) shows the bimodal distribution of values that are on average similar in all cases. Distribution of K_A shows the higher peak slightly shifting to higher values, which is also recognizable in the laterally resolved map as red pixels in the periphery of the right side example. The distribution of T_0 values show a sudden formation of two peaks from the smallest to the mediocre size. In both parameters a stiffer behavior is observed at the periphery of the cells.

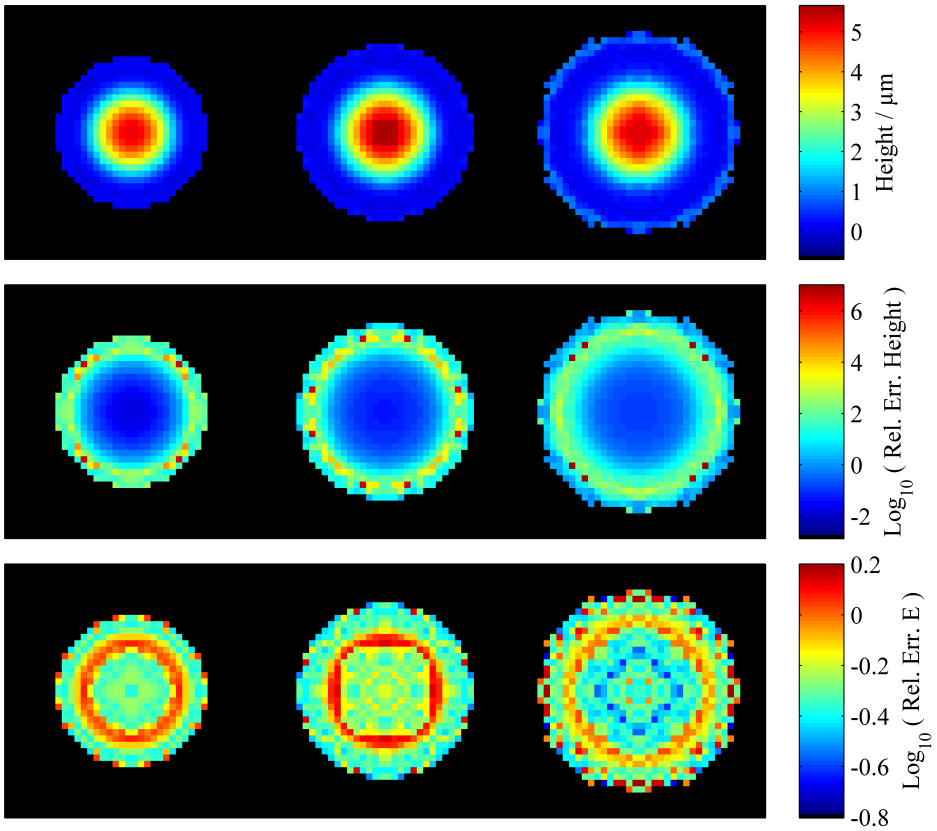

Figure 4.24 – Laterally resolved map of indentation corrected heights (top) show a radially symmetrical distribution height in all three sizes. The logarithmic mean absolute error relative to the mean value for height (middle) as well as Young's modulus (bottom) is also shown, each one with very similar images between the different sizes. Pixel resolution is 1.5 µm^{2}x1.5 µm^2. While both error distributions show a ring-like structure showing increased width of the corresponding parameter distribution in each given pixel the radius of these rings is different for heights and Young's moduli. Also the rings show strong dependence on the pattern size growing with the adhesive disc's radius.

the same time being elevated in height (see figure 4.24 top). Both of these effects probably originate from the fact that the cells' nucleus is usually located in their center. An exception to this general trend poses the prestress distribution in small disc shaped cells. These show barely higher prestress on the outer parts of the cells and average an unimodal distribution when looking at their overall behavior. This difference shows again the advantage of the tension model over continuum mechanics since the difference in prestress cannot be observed in the distribution of Young's moduli only. It should be noted that the Young's moduli in the center of the cells are in the same range as those of confluent cells as described in section 4.1.3, the peripheral regions are decisively stiffer.
To check whether or not the compressibility and Young's moduli simply correlate with the cells' height, the relative mean absolute error for both is shown in figure 4.24. A correlation of the parameters should also lead to a correlation of the errors in each

distribution. However, since the error tend to scale with the magnitude of the mean value, the mean error relative to its mean value are shown. In the images a ring of increased error values is recognizable for both parameters, the radius of these rings differs depending on size and even for a given size is different between height and Young's modulus. Since the errors of these parameters do not correlate the Young's modulus should not simply (only) correlate with cell height.
A correction of substrate influence due to low sample thickness as has been performed for example by Chadwick and coworkers[99] for Sneddon mechanics results in very bad agreement of the theoretical behavior with the actual data acquired (data not shown). The correction has however been shown to cause an overestimation of about 30 % for very thin cellular peripheries in a comparable study on breast cancer cells.[142] In any case the peripheral stiffness in the range of 10^4 Pa is still far below the stiffness of underlying glass substrates which are in the range of 10^9 Pa.
Comparing different shapes of single adherent cells similar to those found present in a wildly growing confluent monolayer of cells (see section 4.1.3) being disc-, square- or rectangular triangle-shaped cells we found a distinct footprint of the geometry in the mechanical behavior. The distribution of the Young's moduli (figure 4.25)

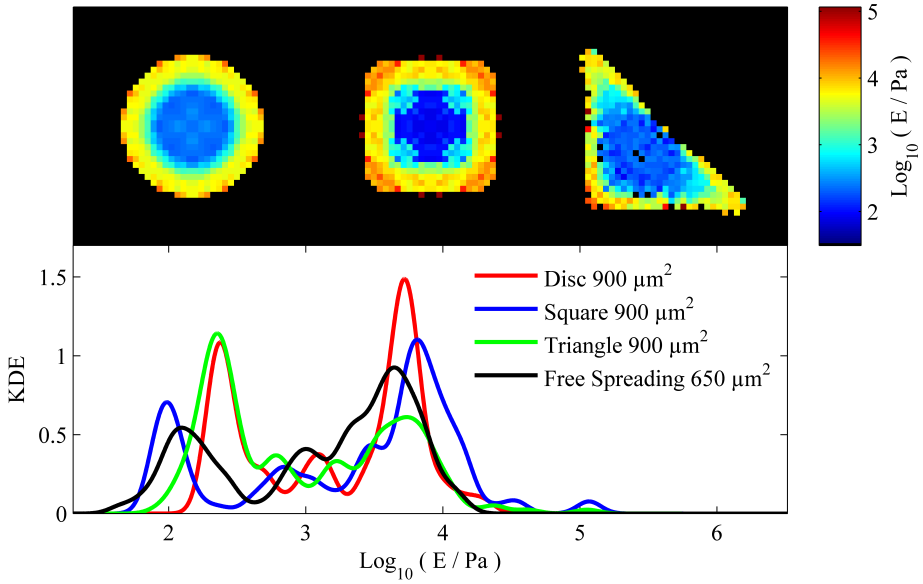

Figure 4.25 – Logarithmic representation of mean Young's moduli of disc-shaped cells in sizes of 900 µm^2, 1200 µm^2 and 1500 µm^2 (color-scaled maps, from left to right, $N = 2834, 1420, 853$). Pixel resolution is 1.5 µm^{2}x1.5 µm^2. For free spreading cells no parameter map is given since an overlay of multiple experiments with no reproducible shape is pointless. The bimodal value distribution can be addressed to geometrical features of the cells, namely the softer center and the stiffer peripheral region similar to the observation in differently sized discs. Interestingly the rectangular corners show only slightly higher moduli that are barely recognizable in the density distributions, the central values however show a strong dependency on the pattern. Note that the distribution of free spreading cells' moduli shows the widest peaks.

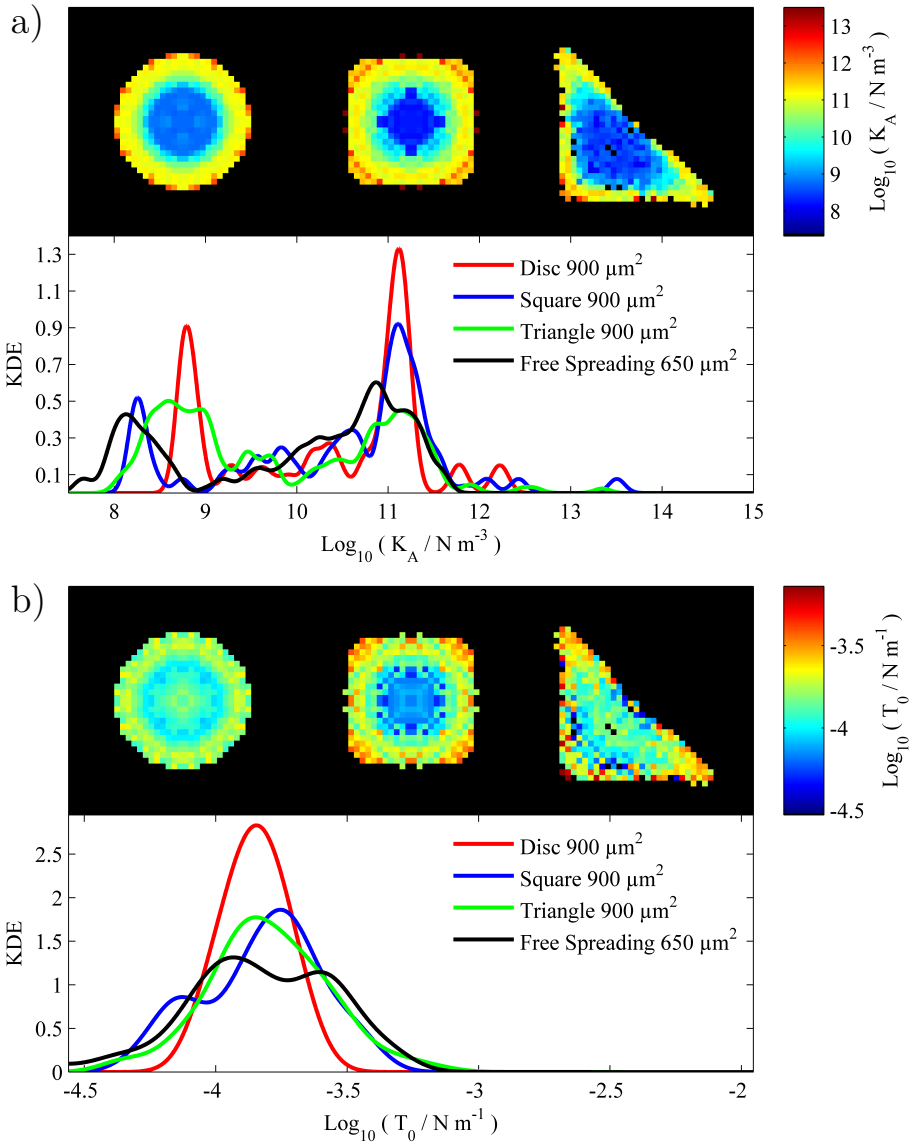

Figure 4.26 – Logarithmic representation of mean area compressibility K_A (a) and prestress T_0 (b) values of disc-, square- and rectangle triangular-shaped cells in sizes of 900 µm^2 (color-scaled maps, from left to right, $N = 2834, 1420, 853$). Pixel resolution is 1.5 µm^{2}x1.5 µm^2. The logarithmic kernel density distribution of the K_A of all pixels shows the bimodal distribution of values corresponding to the softer center and the stiffer periphery in all shapes similar to the distribution of Young's moduli E. In contrast to the E distribution here the peaks of triangular shapes are even wider, while the upper peaks show almost no change depending on the shape. The parameter maps of mean T_0 show higher values in the corners of the patterns which is however recognizable as shoulders in the density distributions. The higher values are however much less separated from the central region's contribution compared to larger shapes.

shows two parameter populations with a softer inside and a stiffer periphery. In the spacially resolved parameter maps the rectangular corners appear to be slightly stiffer even compared to remaining periphery, this however is not very pronounced as seen in the distributions. The central softer peak shows a strong difference between square and disc shape which is surprising given the fact that the central region is the furthest away from the actual geometrically different cue. This does underline the possibility of cellular mechanics as a recognition and reaction tool, since differences in the far periphery seem to be carried to the central region close to the nucleus and this transmission might just be the first step in changes of expression patterns.
We also added the parameter distributions of single free spreading cells to show the overall similar received results, while without adhesion patterns the broadest parameter distributions are obtained, proving that the patterning treatment narrows the distributions by creating reproducible shapes.
The behavior of the compressibility moduli as shown in figure 4.26 is overall fairly similar to the distribution of Young's moduli but especially the softer peak of rectangular triangle cells is much broader than those of square- or disc-shaped cells. The distribution of prestress strikingly shows a unimodal distribution for all shapes in contrast to larger sized disc-shaped cells and to the other parameters. This underlines the importance of considering the mechanical response as caused by two independent parameters. In the parameter maps of prestress, higher values for corners are recognizable similar to the maps of Young's moduli and even more

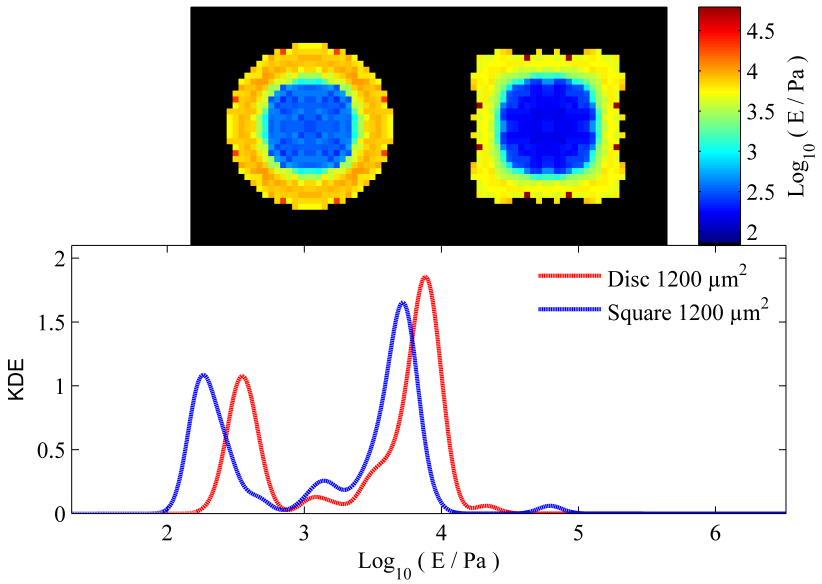

Figure 4.27 – Logarithmic representation of mean Young's moduli of disc-shaped (left) and square shaped (right) cells in sizes 1200 μm^2 (color-scaled maps, $N = 2924, 2001$). Pixel resolution is 1.5 μm^2x1.5 μm^2. The kernel density distributions show a slight difference between the upper peaks which is below the width of mentioned peaks. The lower peaks however are even stronger separated from each other and in good agreement with the comparison done for smaller patterns.

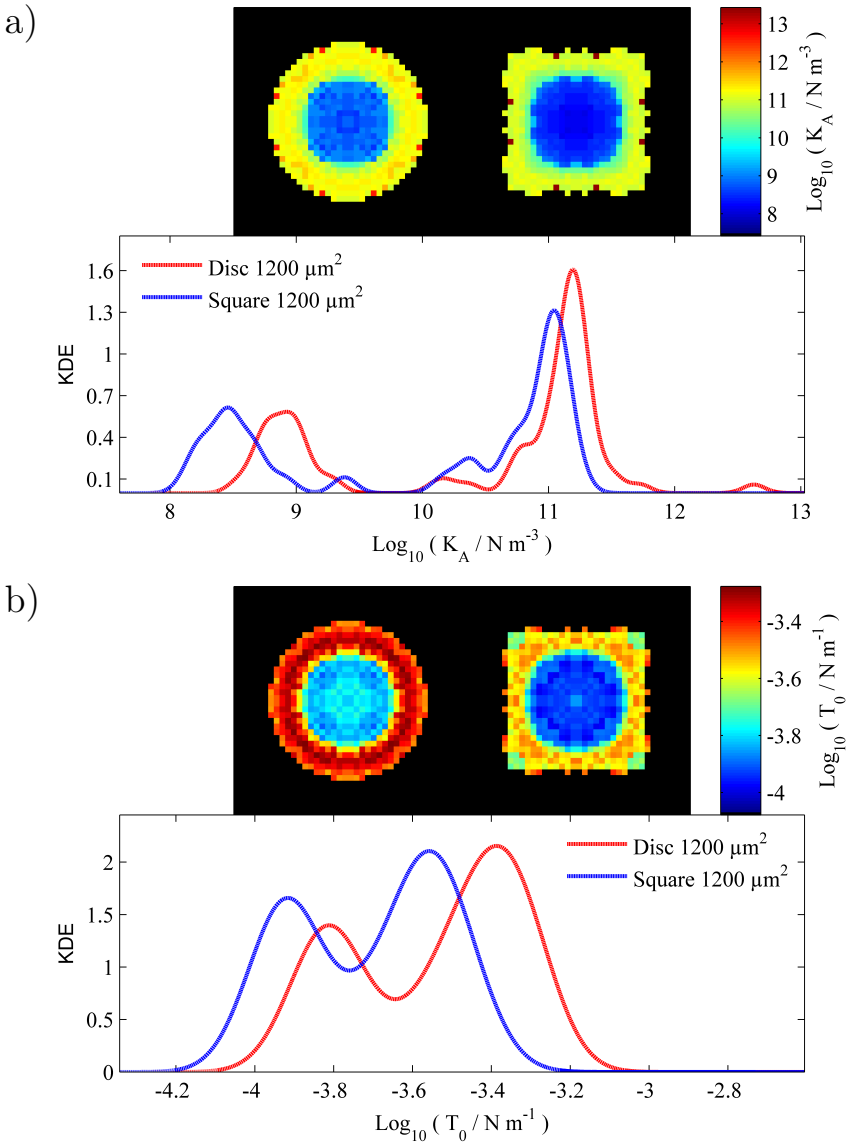

Figure 4.28 – Logarithmic representation of mean area compressibility K_A (a) and prestress T_0 (b) values of disc-shaped (left) and square-shaped (right) cells in a size of 1200 µm^2 (color-scaled maps, $N = 2924, 2001$). Pixel resolution is 1.5 µm^{2}x1.5 µm^2. The logarithmic kernel density distribution of the K_A of all pixels shows the bimodal distribution of values corresponding to the softer center and the stiffer periphery in all shapes similar to the distribution of Young's moduli E with very close upper peaks and stronger separated lower peaks in agreement with experiments on 900 µm^2 examples. The distribution of mean prestress T_0 shows a well separated bimodal distribution in both cases with a decently strong shift between the two patterns. This is a much bigger difference compared to the distribution of the same but smaller sized patterns. Also it validates the observation of the transformation from uni- to well separated bimodal prestress distributions.

pronounced than in the compressibility maps, this difference however is not strong enough to show a separated population in the prestress distributions. The strongest shift observed in the distribution of square-shaped cells and is still much weaker than the shifts in larger sized cells.
To validate the results of increasingly larger disc-shaped cells and the small cells in different shapes we additionally performed experiments on square-shaped cells of $1200\,\mu m^2$ size. Considering the distributions of Young's moduli as shown in figure 4.27 the similarities to the smaller sized patterns are striking. While the upper peaks are close to each other the lower peaks are well separated with the square-shaped cells marking the softest behavior. The spacial distribution of values is also similar to that observed in smaller cells, however the rectangular corners of the square do not show the slighter increased stiffness for the $1200\,\mu m^2$ as the $900\,\mu m^2$ did. In figure 4.28 the evaluation of mechanics according to the tension model is shown where the compressibility modulus behaves very similar to the Young's modulus with the softer peaks being sensitive to the pattern. The prestress distribution is the most interesting since the value distributions are similar in their bimodal shapes but are overall shifted between the two patterns. This validates the change of the distributions from the unimodal shapes in small sizes to bimodal shapes in larger patterns. The overall shift additionally proves that the shape of cells does alter their mechanics, for the medium sizes in compressibility and prestress as well, underlining the possibility of shape regulation via mechanotransduction.

5 Summary and Conclusions

This thesis has shown that a tension-based model considering a thin shell of membrane and actomyosin is sufficient to describe the mechanical behavior of both isolated cell fragments and living cells, underlining that this model is adequate and complete. Probing the mechanical properties of living cells in reproducible shapes and sizes during nanoindentation experiments gives new insights into the way cells determine their own geometry and orchestrate a complex and diverse balance like occurring in many epithelial layers. The intra-cellular resolution of these experiments shows that an anisotropic and identical treatment of cells in a population even if necessary in most layer models might not suffice to determine and explain all and every mechanical cue given to cells in these processes.

By application of the sandwich cleavage process we prepared membrane patches with close-to-native protein and lipid composition. Indentation of these membranes into exactly known pores gives a precise measure of the membrane extension during indentation which results in reliable mechanical parameters. The patches themselves however are not easy to control, as the amount of cortical actin differs from patch to patch even in a single preparation, often resulting in even complete cell transfer. This heterogenity results in broad distributions of the mechanical parameters in repetitive experiments. This trade-off for the complex nature of the samples is worth it, as a bottom up setup is hard to establish. The formation of a solid supported lipid bilayer containing PIP_2 and addition of an active linker protein and filamentous actin in itself poses already a big challenge. The native membrane sheets on the other hand contain probably a huge number of additional lipid and proteins, being passive crosslinkers, active motors or alternative membrane-cytoskeleton linkers.

Although the parameter distribution being rather broad it was shown that benchmarking of the system by either unspecific crosslinking of proteins and also by unspecific protein digestion the changes in mechanical behavior were clearly visible in kernel density plots of the respective data. The compressibility of the patches is very

similar to that of native samples and the changes due to chemical treatment also resemble the expectations from living systems. This observation not only underlines the functionality of these patches but also the applicability of tension-based models to explain the origin of repulsive force - at least during nanoindentation to forces of 500 pN. Proofing the reliability of native patches under artificial conditions and a mechanically equal response to mechanoprobing shows that a thin layer of plasma membrane and cortex dominate mechanical behavior even in living cells. Therefore, further studies seem reasonable including efforts in bottom up approaches which, even when tedious, are promising to reveal insights into the essential components of this important and complex ability of living cells - namely the ability to maintain tension homeostasis.

The tension model has already been applied in studies on living cell monolayers to good success and provided information about the consequences of a number of biochemical modification on cells. In the framework of this thesis the correlation between mechanical parameter and geometrical features was focused and indeed a strong correlation between cell size and stiffness was found. It was shown that geometrical diversity within the monolayer of cells is rather large and that cells adapt shapes that are far off a hexagon. Compared to other tissues however it was demonstrated that size and number of neighbors in confluent MDCK II layers show a rather weak correlation, which might indicate that compressibility dominates over cell cell adhesion. Therefore further investigations of the compressibility in the context of cell geometries were executed.

To get cells in a reproducible shape, patterns of extra cellular matrix proteins were prepared, where single cells adhere on a defined geometry. The instances of these patterns had to be well separated to prevent adherent cells from meeting each other. If they do meet other cells, the cell cell adhesion will often dominate over cell matrix adhesion and consequently the cell layer will ignore the underlying matrix pattern. Single spread cells in general show a stiff perimeter and a softer center at the location of the nucleus. While the outer stiffening might seem like a substrate influence, commonly used corrections to nanoindentation data for such influences failed. A similar behavior is also observed in confluent MDCK II layers, where the perimeter is stiffer than the central region. While the origin of this effect is probably different in confluent cells, an isotropic mechanical behavior along the cell surface is not generally abnormal. Notably the spread cells show lots of microvilli on the cells' surface similar to confluent cells and should accordingly retain a large reservoir of excess membrane area, which is relevant for the interpretation of the compressibility received from analysis according to the tension model.

Investigation of patterned cells allowed not only a good lateral resolution of mechanical properties along the cell surface, due to the reproducibility and high symmetry of the patterns a statistical relevance of parameters in each individual location was achieved. The mechanical analysis was performed according to classical continuum mechanics yielding a Young's modulus as well as according to the tension model. Surprisingly, in contrast to previous studies on other cell lines[143, 144], MDCK II cells in sizes ranging from 900 μm^2 to 1500 μm^2 show only a slight increase in their Young's moduli and compressibility moduli. It should be noted, however, that those

studies did not mention a bimodal distribution of the moduli. The prestress on the other hand reveals a distinctive difference emerging for larger cells, where an unimodal value distribution converts into a bimodal distribution. This change is not visible in the analysis of force-distance data according to continuum mechanics and underlines the superiority of the tension model, where two independent parameters characterize individual features of cellular mechanical behavior. This effect is observed in disc shaped cells and in square shaped cells as well, which means that the change in prestress is probably caused by net cellular size and could therefore possibly serve as a size recognition pathway.
The mechanical differences for different shapes of the same size turned out to be rather small as well. While the distribution of f-actin stress fibers is strongly altered between disc-, square- and triangular-shaped cells, the surface mechanics undergo only minor changes. This actually shows in conjunction with the comparatively small changes due to cell size the robustness of epithelial tension homeostasis. The small difference in compressibility, when comparing corners to sides of cells, is of special interest, since tension model analysis often assumes that the whole cell surface contributes to expansions during nanoindentations. This hypothesis hasn't been proven yet to the best of our knowledge, but if the area expansion is limited to a small circle of influence compared to the cell size the compressibility on rectangular corners should be twice as large as on straight sides. Values in 45° corners should also be twice as large as the rectangular corners and the quadruple value of a straight side (see figure 5.1). Since these changes are missing in the parameter maps resulting from the experiments shown here, this is actually a hint that indeed the whole surface area of cells contributes to the compensation of area dilation. Besides endorsing the analysis, another implication of this finding is that the mechanical force if locally applied migrates on a fast timescale along the whole plasma membrane, endorsing the hypothesis of fast signal transmission from mechanical triggers to sites of mechanotransduction.

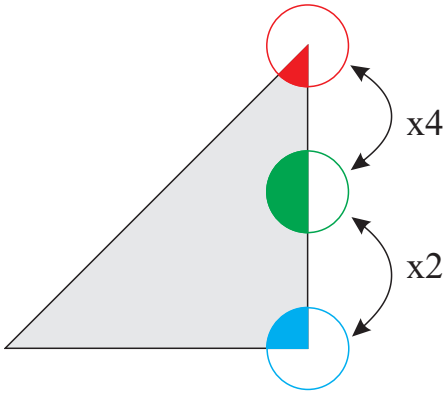

Figure 5.1 – Illustration of effects expected in the case of a small radius of influence during surface area expansion. If the radius is small compared to the size of a cell (in this example, a rectangular triangle cell, grey) expansions due to nanoindentation in the cells' periphery will be compromised by cell borders. Depending of the localization only 50 % (green), 25 % (blue) or 12.5 % (red) of possible area can actually be used.

Additionally, the changes in compressibility due to the different shapes were mainly pronounced in the center of cells instead of the periphery. This observation further supports the idea of a transmission of geometrical information about the circumference of cells their respective center and thereby towards the nucleus. One way these mechanical stimuli can be translated to chemical signals are conformational changes of E-Cadherin, that is known to be present in apical membranes of MDCK II cells[145] and is a prominent mechanotransduction protein[146, 147]. Another option is presented by the mechanical coupling of cytoskeleton to nucleoskeleton via nesprin in cooperation with emerin and SUN proteins[148, 149].
Finally, the low changes in compressibility due to the diverse patterns also underlines the strong ability of MDCK II cells to adapt to mechanically challenging situations and guarantee functionality and viability. These studies underline the difference in response in these kinds of experiments depending on the cell line and thereby provide new information about the pattern formation by cells, being another step on the way to a complete understanding of the brilliant capabilities of cells to tune their mechanical properties.

Bibliography

[1] J. D. Watson and F. H. Crick, "Molecular structure of nucleic acids," *Nature*, vol. 171, no. 4356, pp. 737–738, 1953.

[2] E. S. Lander, L. M. Linton, B. Birren, C. Nusbaum, M. C. Zody, J. Baldwin, K. Devon, K. Dewar, M. Doyle, W. FitzHugh, *et al.*, "Initial sequencing and analysis of the human genome," *Nature*, vol. 409, no. 6822, pp. 860–921, 2001.

[3] N. Wang, J. D. Tytell, and D. E. Ingber, "Mechanotransduction at a distance: mechanically coupling the extracellular matrix with the nucleus," *Nature reviews Molecular cell biology*, vol. 10, no. 1, pp. 75–82, 2009.

[4] A. W. Orr, N. E. Hastings, B. R. Blackman, and B. R. Wamhoff, "Complex regulation and function of the inflammatory smooth muscle cell phenotype in atherosclerosis," *Journal of vascular research*, vol. 47, no. 2, pp. 168–180, 2010.

[5] L. Planas-Paz, B. Strilić, A. Goedecke, G. Breier, R. Fässler, and E. Lammert, "Mechanoinduction of lymph vessel expansion," *The EMBO journal*, vol. 31, no. 4, pp. 788–804, 2012.

[6] A. Reich, M. Meurer, B. Eckes, J. Friedrichs, and D. J. Muller, "Surface morphology and mechanical properties of fibroblasts from scleroderma patients," *Journal of cellular and molecular medicine*, vol. 13, no. 8b, pp. 1644–1652, 2009.

[7] D. A. Fletcher and R. D. Mullins, "Cell mechanics and the cytoskeleton," *Nature*, vol. 463, pp. 485–492, 2010.

[8] A. R. Harris, A. Daeden, and G. T. Charras, "Formation of adherens junctions leads to the emergence of a tissue-level tension in epithelial monolayers," *J Cell Sci*, vol. 127, no. 11, pp. 2507–2517, 2014.

[9] O. Otto, P. Rosendahl, A. Mietke, S. Golfier, C. Herold, D. Klaue, S. Girardo, S. Pagliara, A. Ekpenyong, A. Jacobi, M. Wobus, N. Toepfner, U. F.

Keyser, J. Mansfeld, E. Fischer-Friedrich, and J. Guck, "Real-time deformability cytometry: on-the-fly cell mechanical phenotyping," *Nat. Methods*, vol. 12, pp. 199–202, 2015.

[10] A. Mietke, O. Otto, S. Girardo, P. Rosendahl, A. Taubenberger, S. Golfier, E. Ulbricht, S. Aland, J. Guck, and E. Fischer-Friedrich, "Extracting cell stiffness from real-time deformability cytometry: theory and experiment," *Biophysical journal*, vol. 109, no. 10, pp. 2023–2036, 2015.

[11] M. Bergert, T. Lendenmann, M. Zündel, A. E. Ehret, D. Panozzo, P. Richner, D. K. Kim, S. J. Kress, D. J. Norris, O. Sorkine-Hornung, *et al.*, "Confocal reference free traction force microscopy," *Nature communications*, vol. 7, p. 12814, 2016.

[12] H. Colin-York and M. Fritzsche, "The future of traction force microscopy," *Current Opinion in Biomedical Engineering*, 2017.

[13] A. Pietuch and A. Janshoff, "Mechanics of spreading cells probed by atomic force microscopy," *Open Biol.*, vol. 3, p. 130084, 2013.

[14] H. R. Hertz, "On contact between elastic bodies [ueber die beruehrung fester elastischer koerper]," *J. Reine Angew. Math.*, vol. 94, pp. 156–171, 1881.

[15] I. N. Sneddon, "The relation between load and penetration in the axisymmetric boussinesq problem for a punch of arbitrary profile," *Int. J. Eng. Sci.*, vol. 3, pp. 47–57, 1965.

[16] Y. Sambuy and E. Rodriguez-Boulan, "Isolation and characterization of the apical surface of polarized madin-darby canine kidney epithelial cells," *Proceedings of the National Academy of Sciences*, vol. 85, no. 5, pp. 1529–1533, 1988.

[17] A. Pietuch, B. R. Brückner, T. Fine, I. Mey, and A. Janshoff, "Elastic properties of cells in the context of confluent cell monolayers: impact of tension and surface area regulation," *Soft Matter*, vol. 9, pp. 11490–11502, 2013.

[18] J.-B. Perez, K. L. Martinez, J.-M. Segura, and H. Vogel, "Supported cell-membrane sheets for functional fluorescence imaging of membrane proteins," *Advanced Functional Materials*, vol. 16, no. 2, pp. 306–312, 2006.

[19] K. Fong-ngern, W. Chiangjong, and V. Thongboonkerd, "Peeling as a novel, simple, and effective method for isolation of apical membrane from intact polarized epithelial cells," *Analytical biochemistry*, vol. 395, no. 1, pp. 25–32, 2009.

[20] M. Théry, A. Jiménez-Dalmaroni, V. Racine, M. Bornens, and F. Jülicher, "Experimental and theoretical study of mitotic spindle orientation," *Nature*, vol. 447, no. 7143, pp. 493–496, 2007.

[21] C. M. Nelson, D. Khauv, M. J. Bissell, and D. C. Radisky, "Change in cell shape is required for matrix metalloproteinase-induced epithelial-mesenchymal transition of mammary epithelial cells," *Journal of cellular biochemistry*, vol. 105, no. 1, pp. 25–33, 2008.

[22] S. Kidoaki and T. Matsuda, "Shape-engineered fibroblasts: Cell elasticity and actin cytoskeletal features characterized by fluorescence and atomic force microscopy," *Journal of Biomedical Materials Research Part A*, vol. 81, no. 4, pp. 803–810, 2007.

[23] S. Madin and N. Darby Jr, "Established kidney cell lines of normal adult bovine and ovine origin.," *Proceedings of the Society for Experimental Biology and Medicine*, vol. 98, no. 3, pp. 574–576, 1958.

[24] M. G. Farquhar and G. E. Palade, "Junctional complexes in various epithelia," *The Journal of cell biology*, vol. 17, no. 2, pp. 375–412, 1963.

[25] C. M. Van Itallie and J. M. Anderson, "Architecture of tight junctions and principles of molecular composition," in *Seminars in cell & developmental biology*, vol. 36, pp. 157–165, Elsevier, 2014.

[26] C. Zihni, C. Mills, K. Matter, and M. S. Balda, "Tight junctions: from simple barriers to multifunctional molecular gates," *Nature reviews Molecular cell biology*, vol. 17, no. 9, pp. 564–580, 2016.

[27] A. Martinez-Palomo, I. Meza, G. Beaty, and M. Cereijido, "Experimental modulation of occluding junctions in a cultured transporting epithelium.," *The Journal of Cell Biology*, vol. 87, no. 3, pp. 736–745, 1980.

[28] D. E. Vega-Salas, P. Salas, D. Gundersen, and E. Rodriguez-Boulan, "Formation of the apical pole of epithelial (madin-darby canine kidney) cells: polarity of an apical protein is independent of tight junctions while segregation of a basolateral marker requires cell-cell interactions," *The Journal of Cell Biology*, vol. 104, no. 4, pp. 905–916, 1987.

[29] S. Tsukita, M. Furuse, and M. Itoh, "Multifunctional strands in tight junctions," *Nature reviews Molecular cell biology*, vol. 2, no. 4, pp. 285–293, 2001.

[30] F. I. Comer and C. A. Parent, "Phosphoinositides specify polarity during epithelial organ development," *Cell*, vol. 128, no. 2, pp. 239–240, 2007.

[31] F. Martin-Belmonte and K. Mostov, "Regulation of cell polarity during epithelial morphogenesis," *Current opinion in cell biology*, vol. 20, no. 2, pp. 227–234, 2008.

[32] A. Gassama-Diagne, W. Yu, M. ter Beest, F. Martin-Belmonte, A. Kierbel, J. Engel, and K. Mostov, "Phosphatidylinositol-3, 4, 5-trisphosphate regulates the formation of the basolateral plasma membrane in epithelial cells," *Nature cell biology*, vol. 8, no. 9, pp. 963–970, 2006.

[33] D. Meder, A. Shevchenko, K. Simons, and J. Füllekrug, "Gp135/podocalyxin and nherf-2 participate in the formation of a preapical domain during polarization of mdck cells," *The Journal of cell biology*, vol. 168, no. 2, pp. 303–313, 2005.

[34] K. Umeda, J. Ikenouchi, S. Katahira-Tayama, K. Furuse, H. Sasaki, M. Nakayama, T. Matsui, S. Tsukita, M. Furuse, and S. Tsukita, "Zo-1 and zo-2 independently determine where claudins are polymerized in tight-junction strand formation," *Cell*, vol. 126, no. 4, pp. 741–754, 2006.

[35] G. van Meer and K. Simons, "Lipid polarity and sorting in epithelial cells," *Journal of cellular biochemistry*, vol. 36, no. 1, pp. 51–58, 1988.

[36] A. Viola and N. Gupta, "Tether and trap: regulation of membrane-raft dynamics by actin-binding proteins," *Nature Reviews Immunology*, vol. 7, no. 11, pp. 889–896, 2007.

[37] K. Simons and J. L. Sampaio, "Membrane organization and lipid rafts," *Cold Spring Harbor perspectives in biology*, vol. 3, no. 10, p. a004697, 2011.

[38] A. S. Yap, W. M. Brieher, and B. M. Gumbiner, "Molecular and functional analysis of cadherin-based adherens junctions," *Annual review of cell and developmental biology*, vol. 13, no. 1, pp. 119–146, 1997.

[39] S. Yonemura, Y. Wada, T. Watanabe, A. Nagafuchi, and M. Shibata, "α-catenin as a tension transducer that induces adherens junction development," *Nature cell biology*, vol. 12, no. 6, pp. 533–542, 2010.

[40] T. J. Harris and U. Tepass, "Adherens junctions: from molecules to morphogenesis," *Nature reviews Molecular cell biology*, vol. 11, no. 7, pp. 502–514, 2010.

[41] K. J. Green and C. A. Gaudry, "Are desmosomes more than tethers for intermediate filaments?," *Nature reviews Molecular cell biology*, vol. 1, no. 3, pp. 208–216, 2000.

[42] D. Garrod and M. Chidgey, "Desmosome structure, composition and function," *Biochimica et Biophysica Acta (BBA)-Biomembranes*, vol. 1778, no. 3, pp. 572–587, 2008.

[43] E. Delva, D. K. Tucker, and A. P. Kowalczyk, "The desmosome," *Cold Spring Harbor perspectives in biology*, vol. 1, no. 2, p. a002543, 2009.

[44] G. Meşe, G. Richard, and T. W. White, "Gap junctions: basic structure and function," *Journal of Investigative Dermatology*, vol. 127, no. 11, pp. 2516–2524, 2007.

[45] S. Li, E. R. Gerrard Jr, and D. F. Balkovetz, "Evidence for erk1/2 phosphorylation controlling contact inhibition of proliferation in madin-darby canine kidney epithelial cells," *American Journal of Physiology-Cell Physiology*, vol. 287, no. 2, pp. C432–C439, 2004.

[46] A. Puliafito, L. Hufnagel, P. Neveu, S. Streichan, A. Sigal, D. K. Fygenson, and B. I. Shraiman, "Collective and single cell behavior in epithelial contact inhibition," *Proceedings of the National Academy of Sciences*, vol. 109, no. 3, pp. 739–744, 2012.

[47] G. Klein, M. Langegger, R. Timpl, and P. Ekblom, "Role of laminin a chain in the development of epithelial cell polarity," *Cell*, vol. 55, no. 2, pp. 331–341, 1988.

[48] D. G. Drubin and W. J. Nelson, "Origins of cell polarity," *Cell*, vol. 84, no. 3, pp. 335–344, 1996.

[49] B. Geiger, J. P. Spatz, and A. D. Bershadsky, "Environmental sensing through focal adhesions," *Nature reviews Molecular cell biology*, vol. 10, no. 1, pp. 21–33, 2009.

[50] I. A. Relou, C. A. Damen, D. W. van der Schaft, G. Groenewegen, and A. W. Griffioen, "Effect of culture conditions on endothelial cell growth and responsiveness," *Tissue and Cell*, vol. 30, no. 5, pp. 525–530, 1998.

[51] R. O. Hynes and A. T. Destree, "Relationships between fibronectin (lets protein) and actin," *Cell*, vol. 15, no. 3, pp. 875–886, 1978.

[52] S. Even-Ram, V. Artym, and K. M. Yamada, "Matrix control of stem cell fate," *Cell*, vol. 126, no. 4, pp. 645–647, 2006.

[53] H. Lv, L. Li, M. Sun, Y. Zhang, L. Chen, Y. Rong, and Y. Li, "Mechanism of regulation of stem cell differentiation by matrix stiffness," *Stem cell research & therapy*, vol. 6, no. 1, p. 103, 2015.

[54] R. Olivares-Navarrete, E. M. Lee, K. Smith, S. L. Hyzy, M. Doroudi, J. K. Williams, K. Gall, B. D. Boyan, and Z. Schwartz, "Substrate stiffness controls osteoblastic and chondrocytic differentiation of mesenchymal stem cells without exogenous stimuli," *PloS one*, vol. 12, no. 1, p. e0170312, 2017.

[55] K. Narayanan, V. Y. Lim, J. Shen, Z. W. Tan, D. Rajendran, S.-C. Luo, S. Gao, A. C. Wan, and J. Y. Ying, "Extracellular matrix-mediated differentiation of human embryonic stem cells: differentiation to insulin-secreting beta cells," *Tissue Engineering Part A*, vol. 20, no. 1-2, pp. 424–433, 2013.

[56] T. Wang, J. H. Lai, L.-H. Han, X. Tong, and F. Yang, "Chondrogenic differentiation of adipose-derived stromal cells in combinatorial hydrogels containing cartilage matrix proteins with decoupled mechanical stiffness," *Tissue Engineering Part A*, vol. 20, no. 15-16, pp. 2131–2139, 2014.

[57] R. McBeath, D. M. Pirone, C. M. Nelson, K. Bhadriraju, and C. S. Chen, "Cell shape, cytoskeletal tension, and rhoa regulate stem cell lineage commitment," *Developmental cell*, vol. 6, no. 4, pp. 483–495, 2004.

[58] S. V. Plotnikov, A. M. Pasapera, B. Sabass, and C. M. Waterman, "Force fluctuations within focal adhesions mediate ecm-rigidity sensing to guide directed cell migration," *Cell*, vol. 151, no. 7, pp. 1513–1527, 2012.

[59] P. Kanchanawong, G. Shtengel, A. M. Pasapera, E. B. Ramko, M. W. Davidson, H. F. Hess, and C. M. Waterman, "Nanoscale architecture of integrin-based cell adhesions," *Nature*, vol. 468, no. 7323, pp. 580–584, 2010.

[60] L. B. Case and C. M. Waterman, "Integration of actin dynamics and cell adhesion by a three-dimensional, mechanosensitive molecular clutch," *Nature cell biology*, vol. 17, no. 8, pp. 955–963, 2015.

[61] M. A. Schwartz and D. W. DeSimone, "Cell adhesion receptors in mechanotransduction," *Current opinion in cell biology*, vol. 20, no. 5, pp. 551–556, 2008.

[62] C. C. DuFort, M. J. Paszek, and V. M. Weaver, "Balancing forces: architectural control of mechanotransduction," *Nature reviews Molecular cell biology*, vol. 12, no. 5, pp. 308–319, 2011.

[63] D. R. Critchley, "Focal adhesions–the cytoskeletal connection," *Current opinion in cell biology*, vol. 12, no. 1, pp. 133–139, 2000.

[64] N. J. Anthis, K. L. Wegener, D. R. Critchley, and I. D. Campbell, "Structural diversity in integrin/talin interactions," *Structure*, vol. 18, no. 12, pp. 1654–1666, 2010.

[65] C. E. Turner, "Paxillin and focal adhesion signalling," *Nature cell biology*, vol. 2, no. 12, pp. E231–E236, 2000.

[66] S. K. Mitra, D. A. Hanson, and D. D. Schlaepfer, "Focal adhesion kinase: in command and control of cell motility," *Nature reviews Molecular cell biology*, vol. 6, no. 1, pp. 56–68, 2005.

[67] C. K. Choi, J. Zareno, M. A. Digman, E. Gratton, and A. R. Horwitz, "Cross-correlated fluctuation analysis reveals phosphorylation-regulated paxillin-fak complexes in nascent adhesions," *Biophysical journal*, vol. 100, no. 3, pp. 583–592, 2011.

[68] K. M. Yamada and B. Geiger, "Molecular interactions in cell adhesion complexes," *Current opinion in cell biology*, vol. 9, no. 1, pp. 76–85, 1997.

[69] C. E. Turner, J. R. Glenney, and K. Burridge, "Paxillin: a new vinculin-binding protein present in focal adhesions.," *The Journal of cell biology*, vol. 111, no. 3, pp. 1059–1068, 1990.

[70] H. Shroff, C. G. Galbraith, J. A. Galbraith, and E. Betzig, "Live-cell photoactivated localization microscopy of nanoscale adhesion dynamics," *Nature methods*, vol. 5, no. 5, pp. 417–423, 2008.

[71] C.-h. Yu, J. B. K. Law, M. Suryana, H. Y. Low, and M. P. Sheetz, "Early integrin binding to arg-gly-asp peptide activates actin polymerization and contractile movement that stimulates outward translocation," *Proceedings of the National Academy of Sciences*, vol. 108, no. 51, pp. 20585–20590, 2011.

[72] C. G. Galbraith, K. M. Yamada, and M. P. Sheetz, "The relationship between force and focal complex development," *J Cell Biol*, vol. 159, no. 4, pp. 695–705, 2002.

[73] D. A. Lauffenburger and A. F. Horwitz, "Cell migration: a physically integrated molecular process," *Cell*, vol. 84, no. 3, pp. 359–369, 1996.

[74] S. Na, O. Collin, F. Chowdhury, B. Tay, M. Ouyang, Y. Wang, and N. Wang, "Rapid signal transduction in living cells is a unique feature of mechanotransduction," *Proceedings of the National Academy of Sciences*, vol. 105, no. 18, pp. 6626–6631, 2008.

[75] M. Krause and A. Gautreau, "Steering cell migration: lamellipodium dynamics and the regulation of directional persistence," *Nature reviews Molecular cell biology*, vol. 15, no. 9, pp. 577–590, 2014.

[76] D. Raucher and M. P. Sheetz, "Cell spreading and lamellipodial extension rate is regulated by membrane tension," *J Cell Biol*, vol. 148, no. 1, pp. 127–136, 2000.

[77] C. Le Clainche and M.-F. Carlier, "Regulation of actin assembly associated with protrusion and adhesion in cell migration," *Physiological reviews*, vol. 88, no. 2, pp. 489–513, 2008.

[78] M. A. Partridge and E. E. Marcantonio, "Initiation of attachment and generation of mature focal adhesions by integrin-containing filopodia in cell spreading," *Molecular biology of the cell*, vol. 17, no. 10, pp. 4237–4248, 2006.

[79] P. K. Mattila and P. Lappalainen, "Filopodia: molecular architecture and cellular functions," *Nature reviews Molecular cell biology*, vol. 9, no. 6, pp. 446–454, 2008.

[80] M. D'Alessandro, D. Russell, S. M. Morley, A. M. Davies, and E. B. Lane, "Keratin mutations of epidermolysis bullosa simplex alter the kinetics of stress response to osmotic shock," *Journal of cell science*, vol. 115, no. 22, pp. 4341–4351, 2002.

[81] N. Groulx, F. Boudreault, S. N. Orlov, and R. Grygorczyk, "Membrane reserves and hypotonic cell swelling," *The Journal of membrane biology*, vol. 214, no. 1-2, pp. 43–56, 2006.

[82] A. Pietuch, B. R. Brückner, and A. Janshoff, "Membrane tension and homeostasis of epithelial cells through surface area regulation in response to osmotic stress," *Biochim. Biophys. Acta.*, vol. 1833, pp. 712–722, 2013.

[83] M.-I. Walters, J. M. Papadimitriou, and W. Spector, "Phagocytosis: a review," *CRC critical reviews in toxicology*, vol. 5, no. 4, pp. 377–421, 1978.

[84] C. Sauvanet, J. Wayt, T. Pelaseyed, and A. Bretscher, "Structure, regulation, and functional diversity of microvilli on the apical domain of epithelial cells," *Annual review of cell and developmental biology*, vol. 31, pp. 593–621, 2015.

[85] J. Richardson, V. Scalera, and N. Simmons, "Identification of two strains of mdck cells which resemble separate nephron tubule segments," *Biochimica et Biophysica Acta (BBA)-General Subjects*, vol. 673, pp. 26–36, 1981.

[86] J. Wayt and A. Bretscher, "Cordon bleu serves as a platform at the basal region of microvilli, where it regulates microvillar length through its wh2 domains," *Molecular biology of the cell*, vol. 25, no. 18, pp. 2817–2827, 2014.

[87] J. Seifert, J. Rheinlaender, P. Novak, Y. E. Korchev, and T. E. Schäffer, "Comparison of atomic force microscopy and scanning ion conductance microscopy for live cell imaging," *Langmuir*, vol. 31, no. 24, pp. 6807–6813, 2015.

[88] R. Viswanatha, P. Y. Ohouo, M. B. Smolka, and A. Bretscher, "Local phosphocycling mediated by lok/slk restricts ezrin function to the apical aspect of epithelial cells," *J Cell Biol*, pp. jcb–201207047, 2012.

[89] T. Pelaseyed, R. Viswanatha, C. Sauvanet, J. J. Filter, M. L. Goldberg, and A. Bretscher, "Ezrin activation by lok phosphorylation involves a pip2-dependent wedge mechanism," *eLife*, vol. 6, p. e22759, 2017.

[90] J.-M. Neuhaus, M. Wanger, T. Keiser, and A. Wegner, "Treadmilling of actin," *Journal of muscle research and cell motility*, vol. 4, no. 5, pp. 507–527, 1983.

[91] B. Bugyi and M.-F. Carlier, "Control of actin filament treadmilling in cell motility," *Annual review of biophysics*, vol. 39, pp. 449–470, 2010.

[92] H. L. Yin and P. A. Janmey, "Phosphoinositide regulation of the actin cytoskeleton," *Annual review of physiology*, vol. 65, no. 1, pp. 761–789, 2003.

[93] C. Revenu, R. Athman, S. Robine, and D. Louvard, "The co-workers of actin filaments: from cell structures to signals," *Nature reviews Molecular cell biology*, vol. 5, no. 8, pp. 635–646, 2004.

[94] N. Tao, S. Lindsay, and S. Lees, "Measuring the microelastic properties of biological material," *Biophysical journal*, vol. 63, no. 4, pp. 1165–1169, 1992.

[95] M. Radmacher, J. P. Cleveland, M. Fritz, H. G. Hansma, and P. K. Hansma, "Mapping interaction forces with the atomic force microscope," *Biophysical journal*, vol. 66, no. 6, pp. 2159–2165, 1994.

[96] C. A. Putman, K. O. Van der Werf, B. G. De Grooth, N. F. Van Hulst, and J. Greve, "Tapping mode atomic force microscopy in liquid," *Applied physics letters*, vol. 64, no. 18, pp. 2454–2456, 1994.

[97] J. H. Hoh and C. A. Schoenenberger, "Surface morphology and mechanical properties of mdck monolayers by atomic force microscopy," *J. Cell Sci.*, vol. 107, pp. 1105–1114, 1994.

[98] K. Johnson, K. Kendall, and A. Roberts, "Surface energy and the contact of elastic solids," in *Proceedings of the Royal Society of London A: Mathematical, Physical and Engineering Sciences*, vol. 324, pp. 301–313, The Royal Society, 1971.

[99] N. Gavara and R. S. Chadwick, "Determination of the elastic moduli of thin samples and adherent cells using conical atomic force microscope tips," *Nat. Nanotechnol.*, vol. 7, pp. 733–736, 2012.

[100] E. K. Dimitriadis, F. Horkay, J. Maresca, B. Kachar, and R. S. Chadwick, "Determination of elastic moduli of thin layers of soft material using the atomic force microscope," *Biophys. J.*, vol. 82, pp. 2798–2810, 2002.

[101] N. Gavara and R. S. Chadwick, "Relationship between cell stiffness and stress fiber amount, assessed by simultaneous atomic force microscopy and live-cell fluorescence imaging," *Biomechanics and modeling in mechanobiology*, vol. 15, no. 3, pp. 511–523, 2016.

[102] M. Sarna, A. Zadlo, P. Hermanowicz, Z. Madeja, K. Burda, and T. Sarna, "Cell elasticity is an important indicator of the metastatic phenotype of melanoma cells," *Experimental dermatology*, vol. 23, no. 11, pp. 813–818, 2014.

[103] A. Rigato, F. Rico, F. Eghiaian, M. Piel, and S. Scheuring, "Atomic force microscopy mechanical mapping of micropatterned cells shows adhesion geometry-dependent mechanical response on local and global scales," *ACS nano*, vol. 9, no. 6, p. 5846, 2015.

[104] A. X. Cartagena-Rivera, J. S. Logue, C. M. Waterman, and R. S. Chadwick, "Actomyosin cortical mechanical properties in nonadherent cells determined by atomic force microscopy," *Biophysical journal*, vol. 110, no. 11, pp. 2528–2539, 2016.

[105] A. G. Clark, K. Dierkes, and E. K. Paluch, "Monitoring actin cortex thickness in live cells," *Biophysical journal*, vol. 105, no. 3, pp. 570–580, 2013.

[106] A. Diz-Muñoz, D. A. Fletcher, and O. D. Weiner, "Use the force: membrane tension as an organizer of cell shape and motility," *Trends in cell biology*, vol. 23, no. 2, pp. 47–53, 2013.

[107] J. A. Braunger, B. R. Brückner, S. Nehls, A. Pietuch, V. Gerke, I. Mey, A. Janshoff, and C. Steinem, "Phosphatidylinositol 4, 5-bisphosphate alters the number of attachment sites between ezrin and actin filaments a colloidal probe study," *Journal of Biological Chemistry*, vol. 289, no. 14, pp. 9833–9843, 2014.

[108] C. Morris and U. Homann, "Cell surface area regulation and membrane tension," *Journal of Membrane Biology*, vol. 179, no. 2, pp. 79–102, 2001.

[109] M. J. Rosenbluth, W. A. Lam, and D. A. Fletcher, "Force microscopy of nonadherent cells: a comparison of leukemia cell deformability," *Biophysical journal*, vol. 90, no. 8, pp. 2994–3003, 2006.

[110] B. R. Brückner, A. Pietuch, S. Nehls, J. Rother, and A. Janshoff, "Ezrin is a major regulator of membrane tension in epithelial cells," *Scientific reports*, vol. 5, 2015.

[111] D. E. Discher, P. Janmey, and Y.-l. Wang, "Tissue cells feel and respond to the stiffness of their substrate," *Science*, vol. 310, no. 5751, pp. 1139–1143, 2005.

[112] J. M. Vasiliev, "Spreading of non-transformed and transformed cells," *Biochimica et Biophysica Acta (BBA)-Reviews on Cancer*, vol. 780, no. 1, pp. 21–65, 1984.

[113] C. O'Neill, P. Jordan, and G. Ireland, "Evidence for two distinct mechanisms of anchorage stimulation in freshly explanted and 3t3 swiss mouse fibroblasts," *Cell*, vol. 44, no. 3, pp. 489–496, 1986.

[114] A. D. Lieber, Y. Schweitzer, M. M. Kozlov, and K. Keren, "Front-to-rear membrane tension gradient in rapidly moving cells," *Biophysical journal*, vol. 108, no. 7, pp. 1599–1603, 2015.

[115] N. C. Gauthier, T. A. Masters, and M. P. Sheetz, "Mechanical feedback between membrane tension and dynamics," *Trends in cell biology*, vol. 22, no. 10, pp. 527–535, 2012.

[116] A. X. Cartagena-Rivera, C. M. Van Itallie, J. M. Anderson, and R. S. Chadwick, "Apical surface supracellular mechanical properties in polarized epithelium using noninvasive acoustic force spectroscopy.," *Nature communications*, vol. 8, no. 1, p. 1030, 2017.

[117] M. Czajkowski, D. Bi, M. L. Manning, and M. C. Marchetti, "Hydrodynamics of shape-driven rigidity transitions in motile tissues," *arXiv preprint arXiv:1710.09405*, 2017.

[118] T. B. Saw, A. Doostmohammadi, V. Nier, L. Kocgozlu, S. Thampi, Y. Toyama, P. Marcq, C. T. Lim, J. M. Yeomans, and B. Ladoux, "Topological defects in epithelia govern cell death and extrusion," *Nature*, vol. 544, no. 7649, pp. 212–216, 2017.

[119] R. Farhadifar, J.-C. Röper, B. Aigouy, S. Eaton, and F. Jülicher, "The influence of cell mechanics, cell-cell interactions, and proliferation on epithelial packing," *Current Biology*, vol. 17, no. 24, pp. 2095–2104, 2007.

[120] D. Axelrod, D. Koppel, J. Schlessinger, E. Elson, and W. W. Webb, "Mobility measurement by analysis of fluorescence photobleaching recovery kinetics," *Biophysical journal*, vol. 16, no. 9, pp. 1055–1069, 1976.

[121] J. Schindelin, I. Arganda-Carreras, E. Frise, V. Kaynig, M. Longair, T. Pietzsch, S. Preibisch, C. Rueden, S. Saalfeld, B. Schmid, *et al.*, "Fiji: an open-source platform for biological-image analysis," *Nature methods*, vol. 9, no. 7, pp. 676–682, 2012.

[122] H.-J. Butt and M. Jaschke, "Calculation of thermal noise in atomic force microscopy," *Nanotechnology*, vol. 6, pp. 1–7, 1995.

[123] P. Novak, C. Li, A. I. Shevchuk, R. Stepanyan, M. Caldwell, S. Hughes, T. G. Smart, J. Gorelik, V. P. Ostanin, M. J. Lab, *et al.*, "Nanoscale live-cell imaging using hopping probe ion conductance microscopy," *Nature Methods*, vol. 6, no. 4, pp. 279–281, 2009.

[124] Y. Korchev, M. Milovanovic, C. Bashford, D. Bennett, E. Sviderskaya, I. Vodyanoy, and M. Lab, "Specialized scanning ion-conductance microscope for imaging of living cells," *Journal of microscopy*, vol. 188, no. 1, pp. 17–23, 1997.

[125] K. Grebenkämper and H.-J. Galla, "Translational diffusion measurements of a fluorescent phospholipid between mdck-i cells support the lipid model of the tight junctions," *Chemistry and physics of lipids*, vol. 71, no. 2, pp. 133–143, 1994.

[126] I. Mey, M. Stephan, E. K. Schmitt, M. M. Müller, M. Ben Amar, C. Steinem, and A. Janshoff, "Local membrane mechanics of pore-spanning bilayers," *Journal of the American Chemical Society*, vol. 131, no. 20, pp. 7031–7039, 2009.

[127] J. W. Kuhlmann, I. P. Mey, and C. Steinem, "Modulating the lateral tension of solvent-free pore-spanning membranes," *Langmuir*, vol. 30, no. 27, pp. 8186–8192, 2014.

[128] M. M. Müller, *Theoretical studies of fluid membrane mechanics*. PhD thesis, Johannes Gutenberg-Universität Mainz, 2007.

[129] B. R. Brückner, A. Pietuch, S. Nehls, J. Rother, and A. Janshoff, "Ezrin is a major regulator of membrane tension in epithelial cells," *Sci. Rep.*, vol. 5, p. 14700, 2015.

[130] M. C. Gibson, A. B. Patel, R. Nagpal, and N. Perrimon, "The emergence of geometric order in proliferating metazoan epithelia," *Nature*, vol. 442, no. 7106, pp. 1038–1041, 2006.

[131] A. R. Harris and G. Charras, "Experimental validation of atomic force microscopy-based cell elasticity measurements," *Nanotechnology*, vol. 22, no. 34, p. 345102, 2011.

[132] M. R. Dusseiller, D. Schlaepfer, M. Koch, R. Kroschewski, and M. Textor, "An inverted microcontact printing method on topographically structured polystyrene chips for arrayed micro-3-d culturing of single cells," *Biomaterials*, vol. 26, no. 29, pp. 5917–5925, 2005.

[133] D. Brunette, "Spreading and orientation of epithelial cells on grooved substrata," *Experimental cell research*, vol. 167, no. 1, pp. 203–217, 1986.

[134] K. Schafer, "The cell cycle: a review," *Veterinary pathology*, vol. 35, no. 6, pp. 461–478, 1998.

[135] S. J. Elledge, "Cell cycle checkpoints: preventing an identity crisis," *Science*, vol. 274, no. 5293, p. 1664, 1996.

[136] Z. Darzynkiewicz, M. Roederer, and H. J. Tanke, *Cytometry: new developments*. Academic Press, 2004.

[137] E. Trotta and M. Paci, "Solution structure of dapi selectively bound in the minor groove of a dna t· t mismatch-containing site: Nmr and molecular dynamics studies," *Nucleic acids research*, vol. 26, no. 20, pp. 4706–4713, 1998.

[138] P. Pozarowski and Z. Darzynkiewicz, "Analysis of cell cycle by flow cytometry," *Checkpoint Controls and Cancer: Volume 2: Activation and Regulation Protocols*, pp. 301–311, 2004.

[139] M. Rieseberg, C. Kasper, K. F. Reardon, and T. Scheper, "Flow cytometry in biotechnology," *Applied microbiology and biotechnology*, vol. 56, no. 3, pp. 350–360, 2001.

[140] Z. Darzynkiewicz, G. Juan, and E. Bedner, "Determining cell cycle stages by flow cytometry," *Current protocols in cell biology*, pp. 8–4, 2001.

[141] V. Roukos, G. Pegoraro, T. C. Voss, and T. Misteli, "Cell cycle staging of individual cells by fluorescence microscopy," *Nature protocols*, vol. 10, no. 2, pp. 334–348, 2015.

[142] G. Coceano, M. Yousafzai, W. Ma, F. Ndoye, L. Venturelli, I. Hussain, S. Bonin, J. Niemela, G. Scoles, D. Cojoc, *et al.*, "Investigation into local cell mechanics by atomic force microscopy mapping and optical tweezer vertical indentation," *Nanotechnology*, vol. 27, no. 6, p. 065102, 2015.

[143] S.-Y. Tee, J. Fu, C. S. Chen, and P. A. Janmey, "Cell shape and substrate rigidity both regulate cell stiffness," *Biophysical journal*, vol. 100, no. 5, pp. L25–L27, 2011.

[144] X. Wang, X. Hu, N. Kawazoe, Y. Yang, and G. Chen, "Manipulating cell nanomechanics using micropatterns," *Advanced Functional Materials*, vol. 26, no. 42, pp. 7634–7643, 2016.

[145] N. Borghi, M. Sorokina, O. G. Shcherbakova, W. I. Weis, B. L. Pruitt, W. J. Nelson, and A. R. Dunn, "E-cadherin is under constitutive actomyosin-generated tension that is increased at cell–cell contacts upon externally applied stretch," *Proceedings of the National Academy of Sciences*, vol. 109, no. 31, pp. 12568–12573, 2012.

[146] E. W. Gomez, Q. K. Chen, N. Gjorevski, and C. M. Nelson, "Tissue geometry patterns epithelial–mesenchymal transition via intercellular mechanotransduction," *Journal of cellular biochemistry*, vol. 110, no. 1, pp. 44–51, 2010.

[147] D. Leckband and J. de Rooij, "Cadherin adhesion and mechanotransduction," *Annual review of cell and developmental biology*, vol. 30, pp. 291–315, 2014.

[148] D. E. Jaalouk and J. Lammerding, "Mechanotransduction gone awry," *Nature reviews Molecular cell biology*, vol. 10, no. 1, pp. 63–73, 2009.

[149] C. Guilluy and K. Burridge, "Nuclear mechanotransduction: forcing the nucleus to respond," *Nucleus*, vol. 6, no. 1, pp. 19–22, 2015.

List of Figures

List of Abbreviations

Adenosine Triphosphate (ATP)

Atomic Force Microscopy (AFM)

Bovine Serum Albumin (BSA)

Deoxyribonucleic Acid (DNA)

Force Distance Curve (FDC)

Glutardialdehyde (GDA)

Madin-Darby Canine Kidney Cell Line (MDCK II)

Polydimethylsiloxane (PDMS)

Poly-D-Lysine (PDL)

Phosphatidylinositol 4,5-bisphosphate (PIP_2)

Phosphatidylinositol (3,4,5)-trisphosphate (PIP_3)

Polyethylene Glycol (PEG)

Traction Force Microscopy (TFM)

Transepithelial Resistance (TER)

Curriculum Vitae

Education

2014 - present	PhD Position (Georg-August University, Göttingen)
2011 - 2013	Study of Chemistry (Georg-August University, Göttingen, M.Sc. 1.3) Thesis titled "Selektive Störung der Spannungshomöostase adhärenter Säugetierzellen", Supervisor: Prof. A. Janshoff
2008 - 2011	Study of Chemistry (Georg-August University, Göttingen, B.Sc. 1.7) Thesis titled "*Chiralitätserkennung am Beispiel des Limonens: Einfache Modelle für den Geruchssinn*", Supervisor: Prof. M. Suhm
2007 - 2008	Military Service
2000 - 2007	High school (Max-Planck Gymnasium, Göttingen, Abitur 1.7)

Conferences

2015	10th European Biophysics Congress (Dresden, Germany)
2014	Annual Meeting of the German Biophysical Society (Lübeck, Germany)
	Cell's Retreat 2014 (Goslar, Germany)

Publications

Nehls, S.; Janshoff, A.; *Elastic Properties of Pore-Spanning Apical Cell Membranes Derived from MDCK II Cells*, **2017** (113:8), Biophys. J., 1822 - 1830.

Brückner, B. R.; Pietuch, A.; Nehls, S.; Rother, J.; Janshoff, A.; *Ezrin is a Major*

Regulator of Membrane Tension in Epithelial Cells, Sci. Rep., **2015**, 5:14700.

Braunger, J. A.; Brückner, B. R.; Nehls, S.; Pietuch, A.; Gerke, V.; Mey, I.; Janshoff, A.; Steinem, C.; *Phosphatidylinositol 4,5-Bisphosphate alters the number of attachment sites between ezrin and actin filaments*, JBC, **2014** (289:14), 9833 – 9843.

Matlab Scripts

Young Moduli of Confluent Cell Depending on the Size

PlotCellData.m

```
%%% Used to import JPK ForceMap Data to MatLab
%%% NumberOfCurves is total number of FDCs;
    % set by hand depending on forcemap to deal with
    % incomplete datasets

NumberOfCurves=1296

%%% Reference matrix with correct locations
Tether=(0:NumberOfCurves-1);
dim=sqrt(NumberOfCurves);
matrix=[];
matrix=zeros(dim,dim);
for i=0:1:length(Tether)-1
row=dim-floor((i)/dim);
colum=((i)-floor((i)/dim)*dim)+1;
matrix(row,colum)=Tether(i+1);
end;
if round(dim/2)*2==dim
for i=0:dim/2-1
matrix(i*2+1,:)=fliplr(matrix(i*2+1,:)); % Invert rows for
% even maps
end;
else
    for i=1:dim/2
matrix(i*2,:)=fliplr(matrix(i*2,:)); % Invert rows for uneven
%maps
end;
```

```
end


%% Get List of files in data folder
list = dir('**.txt');
FDCcell=[];
clear data;
for i=1:length(list)
    %Namenliste for indices
    FDCcell0=list(i, 1).name ;
    FDCcell=[FDCcell;FDCcell0];
    %Get Force-Disp-Daten
    filename=list(i, 1).name;
    datatemp=importdata(filename,' ',91);
    data(i).X=datatemp.data(:,1);
    data(i).Y=datatemp.data(:,2);
    i/length(list)
end

%% Extract FDC index from name
FDCcell2=[];
koord=[];
for i=1:length(FDCcell)
    if NumberOfCurves>1000
koord=str2num(FDCcell(i,34:37));%% > 1000 Kurven
    end
    if NumberOfCurves<1000
koord=str2num(FDCcell(i,34:36));%% < 1000 Kurven
    end
FDCcell2=[FDCcell2;koord];
end

%% Sorting data into correct matrix
CellData=zeros(dim,dim);
CellDataSlopes=zeros(dim,dim);
CellDataXY=cell(dim,dim);
for k=1:length(FDCcell2)
for i=1:dim
    for j=1:dim
        if matrix(i,j)==FDCcell2(k)
            CellData(i,j)=min(data(k).X);
            %Force Threshold
%             Slopes=polyfit(data(k).X(data(k).Y>20*10^...
%             (-11)),data(k).Y(data(k).Y>20*10^(-11)),1);
            %TSS Threshold
            Threshold=find(data(k).X<data(k).X(end)+1*10^(-8));
            Slopes=polyfit(data(k).X(Threshold),data(k).Y...
                (Threshold),1);
            CellDataSlopes(i,j)=Slopes(1);
            CellDataXY{i,j}=data(k);
        end
```

```
    end
end
end
%% Break here
    % manually choose contact points for all entries in the
    % data matrix, use FDC_loader to create pws files

%% loading of the loader-changed .mat files
list = dir('**.mat');
CPs=[];
%data=[];
clear pwss;
for i=1:length(list)
    i
    %List of names for indices
    CP0=list(i, 1).name ;
    CPs=[CPs;CP0];
    %Loading PWS file
    filename=CPs(i,:);
    load(filename);
    pwss{i,1}=pws;
end
%%% Extract FDC index (again)
CPsNo=[];
for i=1:length(CPs)
    if NumberOfCurves>1000
koord=str2num(CPs(i,43:46));%% > 1000 curves
    end
    if NumberOfCurves<1000
koord=str2num(CPs(i,43:45));%% < 1000 FDCs
    end
CPsNo=[CPsNo;koord];
end
%%% CellData2 = HeightMap of Contact Points
%%% CellData3 = Relative indentation Depth
CellData2=NaN(dim,dim);
CellData3=NaN(dim,dim);
clear CellDataPWS
CellDataPWS=cell(dim,dim);
for k=1:length(CPsNo)
for i=1:dim
    for j=1:dim
        if matrix(i,j)==CPsNo(k)
            CellData2(i,j)=CellData(i,j)-min(pwss{k, 1}.X);
            CellData3(i,j)=min(pwss{k, 1}.X)/CellData2(i,j);
            CellDataPWS{i,j}=pwss{k, 1};
        end
    end
end
end
```

ForcemapCellSegmentation.m

```
%% calculating the integrals
int=[]
for i=1:length(data)
    clear x
    clear y
    x=data(i).X;
    y=data(i).Y;
    y=y(2:end);
    x=x(1:end-1)-x(2:end);
    int(i)=sum(x.*y);
end

%% plotting integrals in map
CellDataInt=NaN(dim,dim);
for k=0:length(int-1)
for i=1:dim
    for j=1:dim
        if matrix(i,j)==k
            CellDataInt(i,j)=int(k+1);
        end
    end
end
end
imagesc(CellDataInt)

%% Determine the (average) slope image just as an indication of
% cell borders
x=[];
y=[];
x2=[];
y2=[];
slopes1=[];
CellDataSlope=[];
for i=1:length(data)
    x=data(i).X;
    y=data(i).Y;
    x2=x(y>10^(-10)); %only use values >100pN
    y2=y(y>10^(-10));
    if isempty(x2)==1
        slopes(i)=NaN;
    else
        slopes(i)=(y2(1)-y2(end))/(x2(1)-x2(end));
    end
end
for k=0:length(slopes-1)
for i=1:dim
    for j=1:dim
        if matrix(i,j)==k
            CellDataSlope(i,j)=slopes(k+1);
```

```
        end
    end
end
end
imagesc(CellDataSlope)

%% draw lines in plot Itest3
stop=0
x=[2 2]
y=[2 2]
for k=1:150 %max 150 entries should be fine
if (x(1)==1) && (y(1)==1)
else
koords=ginput(2);
x=[koords(1,1) koords(2,1)];
x=round(x);
y=[koords(1,2) koords(2,2)];
y=round(y);
if (x(1)==1) && (y(1)==1)
else
xresol=(min(x):0.001:max(x));
if x(1)-x(2)==0
    line=[];
    line(1:max(y)-min(y)+1,2)=(min(y):1:max(y));
    line(:,1)=x(1);
else
yfit=interp1(x,y,xresol);
yfit=round(yfit);
line=[];
line(:,1)=round(xresol(:));
line(:,2)=yfit(:);
line=unique(line,'rows');
end
% Itest3=Itest;
for i=1:size(line,1)
    Itest3(line(i,2),line(i,1))=0;
end
end
imagesc(Itest3)
end
end


%% delete outer cells

Itest4=[];
Itest4(2:length(Itest3)+1,2:length(Itest3)+1)=Itest3;
Itest4(end+1,end+1)=0;
Itest4(find(Itest4>0))=1;
Itest4(find(Itest4<0))=1; %binarization finished,
%1=value exists, 0=border, also frame of zeros around the matrix
```

```
for i=2:length(Itest4)-1
   if Itest4(i,2)==1;
       Itest4(i,2)=2;
   end
    if Itest4(i,end-1)==1
       Itest4(i,end-1)=2;
   end
end
for i=2:length(Itest4)-1
   if Itest4(2,i)==1;
       Itest4(2,i)=2;
   end
    if Itest4(end-1,i)==1
       Itest4(end-1,i)=2;
   end
end %%every border cell has outer values of 2
for v=1:40
for i=size(Itest4,2)-1:2
    for j=size(Itest4,1)-1:2
        if (max(max(Itest4(i-1:i+1,j-1:j+1)))==2)...
                 && (Itest4(i,j)==1)
            Itest4(i,j)=2;
        end
    end
end
for i=2:size(Itest4,2)-1
    for j=2:size(Itest4,1)-1
        if (max(max(Itest4(i-1:i+1,j-1:j+1)))==2)...
                 && (Itest4(i,j)==1)
            Itest4(i,j)=2;
        end
    end
end
end %Fill border cells
imagesc(Itest4)

%% count and define cell areas
 Itest4(find(Itest4==2))=0; % Replace outer cells (value 2)
 % with zeros
for No=2:20;
var=1;
for k=1:20 %repeat to fill completely
for i=2:size(Itest4,2)-1
    for j=2:size(Itest4,1)-1
        if Itest4(i,j)==var
            Itest4(i,j)=No;
            var=30;
        elseif (max(max(Itest4(i-1:i+1,j-1:j+1)))==No)...
                 && (Itest4(i,j)==1)
            Itest4(i,j)=No;
        end
```

```
    end
end
for i=size(Itest4,2)-1:2
    for j=size(Itest4,1)-1:2
        if Itest4(i,j)==var
            Itest4(i,j)=No;
            var=30;
        elseif (max(max(Itest4(i-1:i+1,j-1:j+1)))==No)...
                && (Itest4(i,j)==1)
            Itest4(i,j)=No;
        end
    end
end
end
end
imagesc(Itest4)

%% reducing the radius of the inner cells
Itest5=Itest4;
reduc=0; %amount of pixels to remove from cell edge
for i=1+reduc:size(Itest4,2)-reduc
    for j=1+reduc:size(Itest4,1)-reduc
        if (min(min(Itest4(i-reduc:i+reduc,j-reduc:j+reduc)))...
                ==0)
            Itest5(i,j)=0;
        end
    end
end
imagesc(Itest5)
%% recruting the numbers
Mechanics1=[];
Mechanics2=[];
Mechanics=[];
Mechanics(:,1)=(2:20);
for No=2:20;
    Mechanics1=[];
    Mechanics2=[];
for i=2:size(Itest4,2)-1
    for j=2:size(Itest4,1)-1
        if Itest5(i,j)==No
           Mechanics1=[Mechanics1;CellDataInt(i,j)];
        end
        if Itest4(i,j)==No
           Mechanics2=[Mechanics2;CellDataInt(i,j)];
        end
    end
end
Mechanics1(find(isnan(Mechanics1)==1))=[];
Mechanics(No-1,2)=sum(Mechanics1)/length(Mechanics1);
Mechanics(No-1,3)=length(Mechanics2);
end
```

```
plot(Mechanics(:,3),Mechanics(:,2),'x')

%% plotting map with median values colorcoded
Itest6=Itest4;
for No=2:20;
for i=2:size(Itest4,2)-1
    for j=2:size(Itest4,1)-1
        if Itest4(i,j)==No
           Itest6(i,j)=Mechanics(No-1,2);
        end
    end
end
end
imagesc(Itest6)
```

Shape Determination

Channel Combination

```
dir=getDirectory("Choose a Directory");
print(dir);
splitDir=dir + "\Split\\";
print(splitDir);
File.makeDirectory(splitDir);
list = getFileList(dir);

for (i=0; i<list.length; i++) {
     if (endsWith(list[i], ".tif")){
               print(i + ": " + dir+list[i]);
            open(dir+list[i]);
            imgName=getTitle();
         baseNameEnd=indexOf(imgName, ".tif");
         baseName=substring(imgName, 0, baseNameEnd);

         run("Split Channels");
         selectWindow("C1-" + imgName);
         rename("C1-" + baseName + ".tiff");
         saveAs("Tiff", splitDir + "C1-" + baseName + ".tif");
         close();
         selectWindow("C2-" + imgName);
         rename("C2-" + baseName + ".tiff");
         saveAs("Tiff", splitDir + "C2-" + baseName + ".tif");

         run("Close All");
     }
} run("Close");
run("Close");
run("Record...");
```

Initiation.m

```
test=C10x2Dfusedoverlay0x2DS4Z5Mask; %image to load
ImageWindow=170;
AreaThreshold=400;

testbw=im2bw(test,0.5);
testbw=imcomplement(testbw); %invertieren
testbw=bwmorph(testbw,'diag'); %fill diagonal pixels
testbw=testbw+1;
testbig=zeros(size(test,1)+4+2*ImageWindow,size(test,2)+4+...
    2*ImageWindow);
testbig(3+ImageWindow:end-2-ImageWindow,3+ImageWindow:end-2-...
    ImageWindow)=testbw;

DeleteBorderObjects
NumerizationOfObjects
DilationAndErosion
ImagesSingleCells
NextNeighboorsRecognition
%% Recognition of Small Cells
SmallCells=find(SingledCellsArea<100);
NextBiggest(isnan(NextBiggest)==1)=0;
for i=1:length(SmallCells)
    [x,y]=find(testbig==SmallCells(i));
    for j=1:length(x)
        testbig(x(j),y(j))=NextBiggest(SmallCells(i));
    end
end
DilationAndErosion %close contacts to the next bigger cells
testbig(testbig>0)=1; %going back to binary image, count again
    %to get correct numbers here
NumerizationOfObjects
ImagesSingleCells
NextNeighboorsRecognition
```

DeleteBorderObjects.m

```
%% Set border-touching cells to zero
testbigold=testbig;

for k=1:1000
[x,y]=find(testbig==0);
k
for i=1:length(x)
if (x(i)>1.5) && (y(i)>1.6) && x(i)<size(testbig,1) &&...
        y(i)<size(testbig,2)
    temp=testbig(x(i)-1:x(i)+1,y(i)-1:y(i)+1);
[x2,y2]=find(temp==1);
```

```
for j=1:length(x2)
    temp(x2(j),y2(j))=0;
end
testbig(x(i)-1:x(i)+1,y(i)-1:y(i)+1)=temp;
if isempty(x2)==1 && isempty(y2)==1
    %temporarily exclude finished pixels
    testbig(x(i),y(i))=-1;
end
end
end
if testbig==testbigold
    break
else
    testbigold=testbig;
end
end
testbig(testbig==-1)=0;
testbig(testbig==2)=0;
```

NumerizationOfObjects.m

```
%% Identify single cells; attribute indeces
for h=2:10000
    h
    [x,y]=find(testbig==1);
    if isempty(x)==1
        break
    end
    x=x(1);
y=y(1);
testbig(x,y)=h;
for k=1:1000
%     k
    testbigold=testbig;
    [x3,y3]=find(testbig==h);
    for l=1:size(x3)
       x=x3(l);
y=y3(l);
temp=testbig(x-1:x+1,y-1:y+1);
[x2,y2]=find(temp==1);

for i=1:size(x2)
    for j=1:size(y2)
        temp(x2,y2)=h;
    end
end
testbig(x-1:x+1,y-1:y+1)=temp;
    end
if testbigold==testbig
```

```
    break
end
end
end
NumberOfObjects=h-1;
```

DilationAndErosion.m

```
%% dilate and erosion to remove false borders
% if artifacts in image binarization/skeletonization
for h=2:NumberOfObjects
    h
    [x,y]=find(testbig==h);
    temp=[];
    temp(1:3,1:3)=h;
    for i=1:length(x) %dilate 1px
    testbig(x(i)-1:x(i)+1,y(i)-1:y(i)+1)=temp;
    end
    [x,y]=find(testbig==h);
    for i=1:length(x) %erode 1px
    temp(:,:,i)=testbig(x(i)-1:x(i)+1,y(i)-1:y(i)+1);
    end
    for i=1:length(x)
    [x2,y2]=find(temp(:,:,i)==h);
    if length(x2)<9
        testbig(x(i),y(i))=0;
    end

    end
end
```

ImagesSingleCells.m

```
%% Get Images of singled Objects
SingledCells=zeros(ImageWindow,ImageWindow,NumberOfObjects);
for h=2:NumberOfObjects
    h
    [x,y]=find(testbig==h);
    if isempty(x)==0
    CEMx=round(sum(x)/length(x));
    CEMy=round(sum(y)/length(y));
    SingledCells(:,:,h)=testbig(CEMx-round(ImageWindow/2):...
        CEMx+round(ImageWindow/2)-1,CEMy-...
        round(ImageWindow/2):CEMy+round(ImageWindow/2)-1);
    for i=1:ImageWindow
        for j=1:ImageWindow
            if SingledCells(i,j,h)==h
```

```
                SingledCells(i,j,h)=1;
            else
                SingledCells(i,j,h)=0;
            end
        end
    end
    end
end
SingledCellsAvg=sum(SingledCells,3);
SingledCellsArea=squeeze(sum(sum(SingledCells,1),2));
```

NextNeighboorsRecognition.m

```
%% Creation of Outlines, Determination of Next Neighboors
SingledCellsNeighboors=zeros(ImageWindow,ImageWindow,...
    NumberOfObjects);
if exist('SingledCellsFirstNeighboors')==1
    clear SingledCellsFirstNeighboors
end
SingledCellsFirstNeighboors={};
for h=2:NumberOfObjects
    h
    [x,y]=find(testbig==h);
    CEMx=round(sum(x)/length(x));
    CEMy=round(sum(y)/length(y));
    SingledCellsNeighboors(:,:,h)=testbig(CEMx-round(...
        ImageWindow/2):CEMx+round(ImageWindow/2)-1,CEMy...
        -round(ImageWindow/2):CEMy+round(ImageWindow/2)-1);
    temp00=[];
    temp0=[];
    temp1=[];
    for i=3:ImageWindow-3
        for j=3:ImageWindow-3
            if SingledCellsNeighboors(i,j,h)==h
                SingledCellsNeighboors(i,j,h)=1; %index of
                %current cell equals 1, ignore all others
                temp=SingledCellsNeighboors(i-2:i+2,j-2:j+2,h);
                temp0=temp(:);
                temp1=[temp(1:5,1);temp(1,2:4)';temp(5,2:4)';...
                    temp(1:5,5)];
                temp0(temp0==-1)=[];
                temp0(temp0==1)=[];
                temp0(temp0==h)=[];
                if isempty(temp0)==0 %&& isempty(find([...
                    %temp(1:5,1);temp(1,2:4)';temp(5,2:4)';...
                    %temp(1:5,5)]==0))==1
                    temp0(temp0==0)=[];
                    temp00=[temp00;temp0];
                end
```

```
            end
        end
    end
    temp00=unique(temp00);
    SingledCellsFirstNeighboors{h,1}=temp00;
end
SingledCellsFirstNeighboorsNbrs=zeros(length(...
    SingledCellsFirstNeighboors),1);
for i=1:length(SingledCellsFirstNeighboorsNbrs)
SingledCellsFirstNeighboorsNbrs(i)=length(...
    SingledCellsFirstNeighboors{i});
end
%% Create Outlines
SingledCellsOutlines=SingledCellsNeighboors;
NextBiggest=[];
for h=2:NumberOfObjects
    h
    [x,y]=find(SingledCells(:,:,h)==1);
    temp=[];
    temp0=[];
    temp00=[];
for i=1:length(x)
            temp=SingledCells(x(i)-1:x(i)+1,y(i)-1:y(i)+1,h);
            if length(find(temp==1))==9
                SingledCellsOutlines(x(i),y(i),h)=0;
            else
               temp=SingledCellsNeighboors(x(i)-2:x(i)+2,...
                   y(i)-2:y(i)+2,h);
               temp0=temp(:);
               temp0(temp0==1)=[];
               temp0(temp0==0)=[];
               temp00=[temp00;temp0];
            end
end
        NextBiggest(h)=mode(temp00);
end
    %% 2D plot of the Cells with number of Neighbours colorcoded
SingledCellsFirstNeighboorsNbrsMap=zeros(size(testbig,1),...
    size(testbig,2));
for h=1:NumberOfObjects
    h
[x,y]=find(testbig(:,:)==h);
for i=1:length(x)
    SingledCellsFirstNeighboorsNbrsMap(x(i),y(i))=...
        SingledCellsFirstNeighboorsNbrs(h);
end
end
%%
for h=1:NumberOfObjects
    l=imagesc(SingledCells(:,:,h))
    axis square
```

```
    print(num2str(h),'-dtiff')
end
```

Danksagung

Zuerst möchte ich Andreas Janshoff danken, für die Übernahme der Betreuung der Arbeit. Dabei hat er selbstständiges Arbeiten stets unterstützt, stand aber bei Fragen jederzeit zur Verfügung. Auch danke ich Michael Meinecke als meinem Zweitbetreuer und, zusammen mit Stefan Jakobs, für die Betreuung als Thesis Committee und während der TCMs.
Auch Sarah Köster, Silvio Rizzoli und Florian Rehfeldt seid gedankt als zusätzliche Teilnehmer im Prüfungskomitee.
Ebenso danke ich Max Albert und Joachim Rädler für die Unterstützung bei der Erstellung der ersten Si-Wafer.
Angela G. und Lennart für ihre gute Arbeit in den jeweiligen Bachelorarbeiten und Praktika, die angenehm zu betreuen waren.
Angela R und Anja für die vielen Zellen, die sie kultiviert und mir für Experimente bereitgestellt haben. Ebenso Petra für die Unterstützung in bürokratischen Angelegenheiten.
Ich danke auch dem gesamten Arbeitskreis, der stets tolerant war und jeden nett aufgenommen hat. Euch hab ich es zu verdanken, dass ich vier Jahre lang (meist) gern in die Uni gegangen bin. Das ist nicht selbstverständlich, und freut mich besonders. Speziell möchte mich bedanken bei Susi, für die Unterstützung bei der Entwicklung der micropatterning Technik, und Andrea, mit der man in mancher Mittagspause der *cuisine* der Nordmensa entkommen konnte.
Dabei seien auch besonders die erwähnt, mit denen ich die meiste Zeit das Büro teilen durfte, nämlich Toto, Moe, Hannes, Filip und Ilyas. Toto, für manch interessantes Gespräch, Moe, für man angeheizte Diskussion, Filip, für die Raucherpausen, und Hannes, mit dem man über jedes experimentelle oder auswertungstechnische Problem diskutieren konnte. Das organisierte Chaos in unserem Büro hätte vermutlich sonst nicht geklappt. Besonderer Dank gilt hier Hannes und Filip für das korrigieren dieser Arbeit.
Ich danke auch meinen WG-Mitgliedern, besonders Markus für fast 20 Jahre Freundschaft, Lissi, für viele nette Gespräche und eine gute Zeit, und Brandon, der zuletzt kam und meine dauerhafte Abwesenheit während der Schreibphase gut akzeptiert

hat. Auch die Mitbewohner ehrenhalber, Jacqueline und Tobi, seien erwähnt und für viele Spieleabende bedankt.
Ich danke auch allen Freunden, viele noch aus dem Studium, für die guten Zeiten und hoffe, den Kontakt auch in Zukunft nicht zu verlieren.
Schließlich danke ich besonders meiner Familie, die mich immer unterstützt hat in Belangen jedweder Art. Auch Emma danke ich, für einfach alles was sie in der Zeit getan hat.